ADDITIVE MANUFACTURING AND ELECTROLESS METALLIZATION OF A 4X4 V-BAND CONTORTED WAVEGUIDE BUTLER MATRIX

A Dissertation

by

AMRITA BAL

Submitted to the Office of Graduate and Professional Studies of
Texas A&M University
in partial fulfillment of the requirements for the degree of

DOCTOR OF PHILOSOPHY

Chair of Committee,	Gregory H. Huff
Co-Chair of Committee,	Robert D. Nevels
Committee Members,	Jean-Francois Chamberland
	Darren J. Hartl
	H. Rusty Harris
Head of Department,	Miroslav M. Begovic

August 2021

Major Subject: Electrical Engineering

ABSTRACT

This research presents an investigation of high-performance antennas and beamforming networks with complex geometric features that are uniquely enabled by distinct design spaces created from the intersection of microfluidics, applied electromagnetics, and additive manufacturing. Each design space is explored by a demonstration vehicle that can be used to test key concepts relevant to the types of structures and challenges to current fabrication techniques they are targeted to address. The first demonstration vehicle involves the development of structurally embedded vascular antennas to provide reconfigurable electromagnetic antenna properties in multilayer and complex curved surfaces. The second investigates the development of compact multi-port contorted waveguide networks that provide signal routing and a discrete Fourier transform of the signal for beam switching applications. Each vehicle provides a distinct pathway that leverage design for additive manufacturing whose goal is to develop new high frequency components and devices.

Structurally embedded vascular antennas are functionalized by embedding sacrificial materials into the layup of a structural composite and formed using a mandrel to set the desired geometric structure. After the composite has been cured microvascular structures with desired geometric patterns are embedded between composite lay-ups. Controlled transport of liquid metal through these embedded capillaries enables functionalization of the additively manufactured structure into an antenna or antenna array reconfigurable over

a wide range. Two distinct structures have been pursued as a demonstration vehicle to leverage these concepts. These are, a multilayer structure with distinct geometrical patterns positioned in separate layers and a complexly curved composite shaped to resemble the leading edge of an Unmanned Aerial Vehicle.

The “contorted waveguide” topologies are electromagnetically functionalized through a pressure-driven electroless metallization process that deploys fluid-flow through the structure as a means of chemically depositing the conductive layer required to support low-loss wave propagation and guidance. The resulting workflow developed for these components provide a novel low-cost and low-waste-generating process for realizing millimeter-wave volumetric structures that would be challenging if not impossible to fabricate through conventional techniques. The design, fabrication, and experiment of a four-input and four-output beamforming network referred to as a butler matrix is used as a demonstration vehicle to showcase the capabilities and study the limitations of contorted waveguide structures.

ACKNOWLEDGEMENTS

I would like to thank my committee chair, Dr. Huff, for offering me an opportunity to pursue research on this interdisciplinary topic which has helped me develop deep insights into complex problems and grow as a researcher. I would also thank my committee members, Dr. Nevels, Dr. Hartl, Dr. Chamberland, and Dr. Harris, for their guidance and support throughout this research.

Thanks also go to my colleagues Deanna Sessions, Inderdeep Singh, Joshua Ruff, Bailey Campbell, Sumana Pallampati, Anoop Tiwari, and the department faculty and staff for making my time at Texas A&M University a great experience. I would also like to thank my graduate teaching advisor Mr. Pat Wallace from the Electronic Systems Engineering Technology department for his continued trust, confidence, and patience in me by offering me the opportunity to conduct classes as a teaching assistant. He has been a constant source of encouragement and family away from home.

Thanks to my friends Dileep, Jyothsna, Deepika, Deepak, Archana, and Vinaya for cheering me up during stressful days and being family away from my home.

Finally, thanks to my mother Late Pramila Bal, and father Amalendu Bal for their continuous emotional and financial support. This journey would not have been possible without their trust, love, and sacrifices. I would also thank my parents-in-law Padmaja

Malladi and Prakash Amalladinne for believing in me and encouraging me to pursue higher studies. Thanks to my sister-in-law Aparna Amalladinne and her husband Rohan Swayambhatla for being a strong pillar of strength throughout the journey. Lastly, I would like to thank my loving husband Vamsi Amalladinne for being present right beside me through the thick and thin of this journey. This journey would have been impossible without his continuous encouragement and love.

CONTRIBUTORS AND FUNDING SOURCES

Contributors

This work was supervised by a dissertation committee consisting of Professor G. H. Huff of the Department of Electrical and Computer Engineering, Professor Darren J. Hartl of the Department of Aerospace and Department of Material Science Engineering, Professor Robert Nevels, Professor Jean -F. Chamberland and Professor H. Rusty Harris of the Department of Electrical and Computer Engineering.

The fabrication of multilayer and complex-curved composite performed in Chapter II was carried out in U.S. Air Force Research Laboratory and University of Dayton Research Institute. Discussion on fabrication and material aspect of these structures were carried out with Professor Darren J. Hartl of the Department of Aerospace and Department of Material Science Engineering. This work is published in 2021.

All other work conducted for the dissertation was completed by the student independently.

Funding Sources

Graduate study was supported by a Teaching Assistantship from Department of Electronic Systems Engineering Technology (2017-2021) and Department of Electrical and Computer Engineering (2016-2017) of Texas A&M University

This work was also made possible in part by U.S. Air Force Research Laboratory (AFRL). Any opinions, findings, and conclusion or recommendations expressed in the material indicated in chapter II are those of the authors and do not necessarily reflect the view of the AFRL or the US government. Approved for public release (88ABW-2017-5151).

NOMENCLATURE

EM	Electromagnetics
SEVA	Structurally Embedded Vascular Antenna
ML-SEVA	Multilayer SEVA
SEVA-CLA	Multielement SEVA Conformal Linear Array
SEVA-RLα2	SEVA Relaxed Logarithmic with α=2
SEVA-RLα30	SEVA Relaxed Logarithmic with α=30
VHF	Very High Frequency
ISM	Industrial, Scientific, and Medical
BM	Butler Matrix
UAV	Unmanned Aerial Vehicle
5G	Fifth Generation
AM	Additive Manufacturing
RF	Radio Frequency
3D	Three-dimensional
EGaIn	Eutectic Gallium Indium
cPLA	Catalyzed Polylactic Acid
SLA	Stereolithography
CWG	Circular Waveguide
R2C-WG	Rectangular-to-circular Waveguide
mm-wave	Millimeter Wave

TRL	Thru, Reflect and Line
SOLT	Short, Open, Load and Thru
.SLA	Stereolithography file format
FC-70	Fluroinert Electronic Liquid
IoT	Internet of Things

TABLE OF CONTENTS

Page

LIST OF FIGURES

Page

CHAPTER I

INTRODUCTION

Technological advances in the fields of sensing, communication, robotics, autonomous vehicles, wearable electronics etc. necessitates the development of advanced and high-performance Radiofrequency (RF) and Electromagnetic (EM) devices. The advent of fifth generation (5G) of wireless communication is constantly pushing for increase in the transmission rates, coverage, and number of connections. The concept of Internet of things (IoT) will lead to an exponential increase in the number of devices and sensing systems, connecting everyone and everything. These have increased challenges for RF engineers to develop high performance EM and RF components without compromising on users' comfort or aesthetics of the device. Conventional fabrication techniques pose serious constraints on developing structures with complex geometry which could possibly restrict the growing demands of devices suitable for the expanding market. Researchers are always on the lookout for alternative fabrication technologies which could offer similar performance as conventional technologies at lesser cost and in short time. Among the different fabrication techniques Additive Manufacturing (AM) or 3D printing technology has advanced significantly in the last decade and this technology enables easy and fast prototyping of geometrically-complex structures at low-cost and in considerably less time, offering the desired performance metric as conventional fabrication techniques. Combination of additive manufacturing with fluidics or microfluidics enables creation of geometrically complex and contorted RF and EM devices like antennas, hybrids, filters

etc. which can lower barrier for some of the challenges seen with conventional fabrication techniques today.

Additive manufacturing is the process of developing lighter, stronger systems or parts by depositing layer upon layer of substrates. AM techniques have been in practice for multiple decades now along with other popular techniques like subtractive manufacturing. But, circa 2012 exponential increase in patents in the field of AM has been observed, which bought in new advances in the field and expanded the field of application for additive techniques. There has been constant effort from the research community to develop efficient AM techniques reducing defects introduced in the process of fabrication and making the process of manufacturing streamlined, in lesser time and cost-effective way. Applications of AM is seen across various industries and sectors like space, aerospace, construction, manufacturing etc.. AM is emerging as a popular choice across different sectors as a tool to design structures with complex geometry in less time and lesser cost, otherwise challenging not to mention impossible with conventional fabrication techniques. Impact and evolution of AM in aerospace industry is enumerated in [1]–[3]. These articles explore the new opportunities and avenues that could potentially be generated using AM. AM cuts down time to market and fabrication cost of complex components required in aerospace. Other industries where application of AM is widespread are in space, construction and manufacturing [4]–[7]. AM is also increasingly being used in the design of EM devices, antennas and RF components to print complex geometry in less time and cost. Application of AM to print complex antennas like fractals,

horns, lens and various others are explored in [8]–[14]. Apart from antennas complex EM devices like couplers, filters, power combiners are also fabricated using additive techniques [15]–[18]. These EM devices offer similar performance at lower cost and has much higher ease of fabrication.

Fluidics or microfluidics is broadly defined as the study of liquid in motion and this property of fluid could be exploited to obtain mechanical or electronic functions. Selective flow of fluid in closed space obtained by application of pressure could offer interesting solutions to problems across various disciplines like biology, chemistry, electronics etc.. Bones of cuttlefish are an example of a natural biological system containing multiple parallel microscopic chambers which are reinforced by winding wall like structures. Fluid moves through cuttlebones at different pressure and flow rates. Application of microfluidics in the areas of biology, chemistry and medicine has been here for decades [19]–[21]. Application of fluidics or microfluidics span beyond its traditional filed and it is being widely used in developing electronics. Microfluidic devices are soft and extensive research is being carried out to integrate these soft components into electronics, in place of traditional insulators, conductors or semiconductors. Microfluidic electronics is an emerging field of study whose applications range across different sectors like bio-inspired devices, body-worn healthcare and medical sensing systems [22]–[24]. Interesting application of microfluidics has been shown in the implementation of antennas, engineered EM materials and EM devices as switches, in place of conductors, beam scanning applications etc. [22]–[28]. These microfluidic EM structures offer similar

performance as conventional metallic antennas with ease of shape reconfiguration and invisibility to radar signals upon retraction of liquid metal from the capillaries.

This dissertation explores the design, analysis, fabrication and measurement of geometrically complex and contorted electromagnetic structures and antennas additively printed and functionalized using fluidic or microfluidic concepts. Broadly two distinct electromagnetic structures are studied in this dissertation. The first structure is an antenna which is additively embedded as microvascular cavity inside an epoxy composite and functionalized to operate as an antenna by controlled transport of liquid metal through those embedded capillaries. The second structure, a contorted waveguide Butler matrix has been additively printed and metallized by selective flow of metal bath solution to operate as a beam forming network. The scope and limitations of these structures are established through investigation of measured and simulated results. The dissertation is divided into three chapters summarizing the background, accomplishments and results. The key aspects covered in each chapter are enumerated in the next section.

Summary and Key Contributions

- Chapter II: Multilayer and Conformally Integrated Structurally Embedded Vascular Antenna Arrays
  - Demonstrated the ability to engineer multi-layer and conformally curved reconfigurable antennas enabled by the transport of liquid metal in structurally embedded vascular networks.

    - Demonstrated that vascular networks can be fabricated on two consecutive (closely spaced) layers of fabric in the composite layup.
    - Demonstrated that vascular networks can be embedded with distinct pattern in a complexly curved composite mimicking the shape of a UAV wing.
  - Developed expertise in the design, fabrication, and electromagnetic functionalization of these structures that leads to a better understanding of the challenges they present and the opportunities they provide.
    - Successfully utilized the technique to create a multi-layer SEVA in which two co-located reconfigurable antennas can be utilized synergistically for radiation and impedance tuning.
    - Successfully utilized the technique to demonstrate beam scanning of a three-element array on a complex curved composite and reconfigurable over a decade of frequency range.
    - Identified the prerequisites, limitations and challenges of fluid (liquid metal) flow in similarly embedded complex geometry EM devices and antennas.
- Chapter III: Electroless Metallization of Additively Manufactured Structure
  - Demonstrated the assembly and operation of a low-cost, selective and low-waste generating metallization technique for electroless deposition of V-band additively manufactured EM devices.
    - Demonstrated the assembly and operation of a closed loop system with peristaltic pump at the heart to selectively metalize EM structures using electroless deposition techniques.

        - Brought to light the deposition of precipitates during the metallization process and introduced filter in the path of electroless solution to improve overall performance of metal plated EM devices.
    - Developed proficiency to understand fluid flow inside closed contoured complex geometries and expand the current metallization technique to understand the scope and challenges in metal plating multiport complex EM structures.
        - Developed appropriate connectors and techniques for smooth flow of electroless metal bath inside 2-port and multiport waveguides, hybrids, antennas etc.
        - Developed understanding of fluid flow inside complex geometry to successfully metallize complex EM structures with curves and bends as well as intricate patterns.
- Chapter IV: Three-dimensional Design, Analysis and fabrication of Beam forming networks
    - Demonstrated the ability to analyze, design, and fabricate non-planar three-dimensional beamforming network printed using additive manufacturing techniques
        - Demonstrated that complex waveguide curves and bends can be designed to maintain rotational symmetry and preserve the polarization of the structure.
        - Demonstrated that non-planar fully three-dimensional Butler matrix can be designed to operate successfully over the frequency range of 57-64 GHz.

- Developed expertise in analyzing limitations of current additive techniques in design of EM devices and find possible solutions to alleviate these challenges.
    - Identified the source of anomalous reflections observed in measurements (not simulations) by analyzing mode converters and other locations susceptible to the impact of fabrication workflow.
    - Successfully established the relationship between fabrication limitations on performance of complex waveguide structures with multiple twists and bends.

Publications

JOURNALS

- Amrita Bal, Jeffery W Baur, Darren J Hartl, Geoffrey J Frank, Thao Gibson, Hong Pan and Gregory H Huff, "Multi-Layer and Conformally Integrated Structurally Embedded Vascular Antenna (SEVA) Arrays", Sensors (2021)
- A. Bal, D. Carey, F. Espinal and G. H. Huff, "Electroless Silver Plating of 3D Printed Waveguide Components by Peristaltic Pump Driven System", Electronics Letters (2019)

CONFERENCES

- Amrita Bal and Gregory H. Huff, "Modelling and Impact of 3D Print Inaccuracies on the performance of Circular waveguide Hybris Coupler", International Applied Computational Electromagnetics Society Symposium (2020)

- Amrita Bal, Anoop Tiwari and Gregory H Huff, “Electroless Silver Plating of Additive Manufactured Trough Waveguide Mode Transducer and Antenna Structure”, IEEE International Symposium on Antennas and Propagation and USNC-URSI Radio Science Meeting (2019)
- Amrita Bal, Anoop Tiwari, Wenbo Liu and Gregory H Huff, “Pressure-driven Selective Electroless Metallization of Additive Manufactured Multi-port V-band Waveguide Antennas and Beamformers”, Antenna Applications Symposium (2019)
- Amrita Bal, Jeffery W Baur, Darren J Hartl, Geoffrey J Frank, Thao Gibson, Hong Pan and Gregory H Huff, “Beamforming and Reconfiguration of a Structurally Embedded Vascular Antenna Array (SEVA^2) in both Multilayer and Complex-curved Composites (2017)

CHAPTER II

MULTI-LAYER AND CONFORMALLY INTEGRATED STRUCTURALLY EMBEDDED VASCULAR ANTENNA (SEVA) ARRAYS

This chapter presents the design and fabrication of two multi-element Structurally Embedded Vascular Antennas (SEVAs). These are achieved through advances in additively manufactured sacrificial materials and demonstrate the ability to embed vascular microchannels in both planar and complex-curved epoxy-filled quartz fiber structural composite panels. Frequency-reconfigurable antennas are formed by these structures through the pressure-driven transport of liquid metal through the embedded microchannels. The planar multi-layer topology examines the ability to fabricate two co-located radiating structures separated by a single ply of quartz fabric within the composite layup. The multi-element linear array topology composed of microchannels embedded on to a single-layer are used to demonstrate the ability to conformally-integrate these channels into a complex curved surface that mimics an array of antennas on the leading edge of an Unmanned Aerial Vehicle (UAV). A parallel-strip antipodal dipole feed structure provides excitation and serves as the interface for fluid displacement within the microchannels to facilitate reconfiguration. The nominal design of the SEVAs achieve over a decade of frequency reconfiguration with respect to the fundamental dipole mode of the antenna. Experimental and predicted results demonstrate the operation for canonical states of the antennas. Additional results for the array topology demonstrate beam steering and contiguous operation of interconnected elements in the multi-element structure.

Background

Unmanned Aerial Vehicles (UAV) are deployed to serve a wide variety of commercial, municipal, and defense applications including health care, public safety, mobile network coverage diagnostics, etc. [29]–[31]. The growing utilization of UAV-based application spaces and the growing complexity of their missions have increased the need for more robust communication and sensing systems that support these wireless links. This has facilitated a need for robust, shape-conformal and frequency reconfigurable antennas and phased arrays that can adapt to dynamic operational scenarios; these vehicles (controlled remotely or autonomously) are also required in many scenarios to maintain reliable and long-range communication with a ground station. Reconfigurable, multi-band, and/or broadband omnidirectional antennas used in UAV applications have been proposed in response to this (e.g., [32]–[37]). Antenna arrays have also been used in-place of single antennas in these applications to provide enhanced gain and scanning capabilities (e.g., [38]–[40]).

Antennas considered for use in UAVs are often derived from canonical planar topologies. The integration of these antennas on/in to the UAV presented challenges and numerous efforts have been carried out to embed these antennas into load bearing structures (even conformal to their surfaces). These efforts mainly focused on improving structural efficiency and antenna performance. Various efforts in this direction resulted in development of vertically grown carbon nanotubes and carbon composite fibers used for fabrication of load bearing antennas having desirable RF and mechanical performance

[41], [42]. Similar load bearing antennas, like Conformal Load bearing Antenna Structures (CLAS) and Composite Smart Structures (CSS), have been proposed to overcome geometrical limitations and eases integration with a non-planar surface [43]–[46]. Examples of CLAS include MEMS reconfigurable pixelated patch antennas and bi-layer log periodic antenna arrays [47], [48]. Antennas and antenna arrays designed using high strength metal coated fibers suited for stress, weight and shape critical applications provide synergistic advance [49]–[51].

The development of load bearing antenna technologies has been critical in the deployment of radiating systems that can withstand the extreme environments and physical conditions encountered by both traditional aircraft and UAVs [52]–[55]. Advances in additive manufacturing using liquid metal as a reconfiguration mechanism [56], [57] have been demonstrated recently to impart a greater degree of electromagnetic agility into the design space of conformal load bearing antenna systems. Previous work on the load bearing, structurally embedded vascular antenna (SEVA) [57] demonstrated the frequency reconfigurability of a dipole antenna meandered in exponentially increasing sinusoidal pattern. The effective (resonant) length of the embedded dipole was varied using pressure driven transport of liquid metal (eGaIn) [58] to operate the antenna over a wide frequency range. The prior work [59]–[62] on embedded structures emphasize on the mechanics, materials and fundamental concepts used to emphasize the functionalization of antennas in structurally embedded environments. The repeatability and stability of antenna characteristics make this structure an extensible demonstration vehicle to use in future and

ongoing efforts. In this work the design is used to demonstrate the ability to engineer multi-layer and conformally curved reconfigurable antennas enabled by transport of liquid metal through the embedded microvascular channels. This is illustrated through two unique designs- First it is used to demonstrate an antenna with vascular networks fabricated on two closely spaced and consecutive layer of fabric in the composite lay-up. In the second design it is shown that vascular networks with distinct pattern can be fabricated in a complexly curved substrate mimicking the shape of a UAV wing. These structurally embedded vascular antennas operate over a decade of frequency in a single footprint.

To demonstrate the concepts of electromagnetically functionalized antenna controlled by transport of liquid metal straight line dipole as well as modified dipole with exponentially increasing sinusoidal patterns are considered. Dipole is the simplest type of antenna consisting of two identical conductive elements such as metal wires or rods. It produces an omnidirectional radiation pattern supporting a line current that has only one node at each end. A radiating dipole is half wavelength in length measured from end to end consisting of two quarter wavelength sections. The current distribution is of standing wave approximately sinusoidal along the length of dipole with nodes at each end and antinode at the center. Two wire dipole with frequency of resonance at 2.4 GHz with omnidirectional radiation pattern is shown in Figure 1.

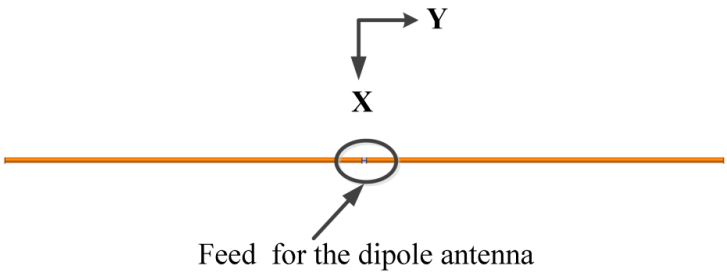

(a)

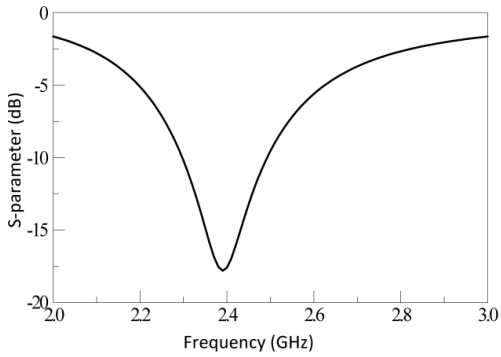

(b)

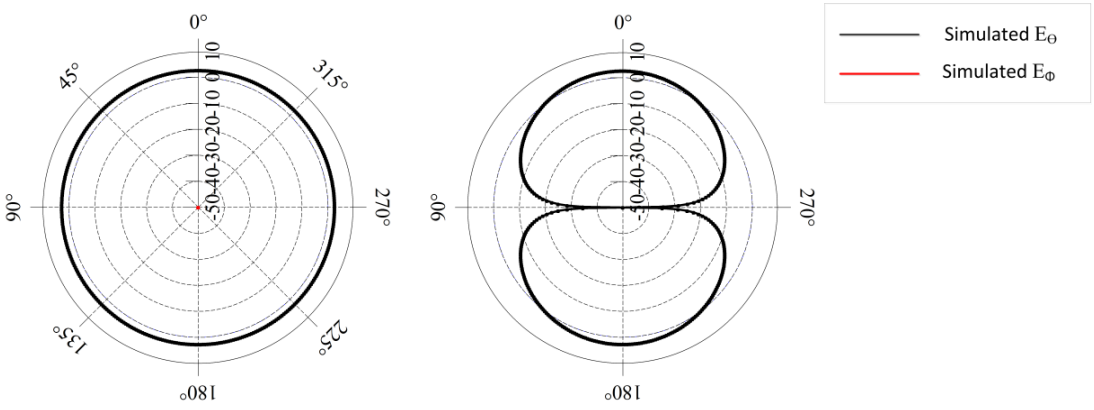

(c)

Figure 1 Characteristics of a two-wire dipole. (a) Two wire dipole excited in the center (b) Frequency response of the dipole (c) Radiation pattern of the dipole in xz- (left) and yz- (right) plane.

The first configuration, Multilayer SEVA (ML-SEVA) explored in this chapter investigates dipoles structurally embedded in epoxy composite. One of the layers has straight dipole while the other layer has exponentially increasing sinusoidal dipole embedded in the composite. The second configuration, SEVA conformal linear array (SEVA-CLA) consists of three exponentially increasing sinusoidal dipoles embedded in the epoxy composite, which work together as an antenna array. Antenna arrays typically consists of multiple antenna elements arranged in linear, planar or volumetric fashion, where phase and magnitude of each element is varied to obtain beam scanning in space. Figure 2 show the beam scanning along 360 degrees in space using three-element isotropic elements.

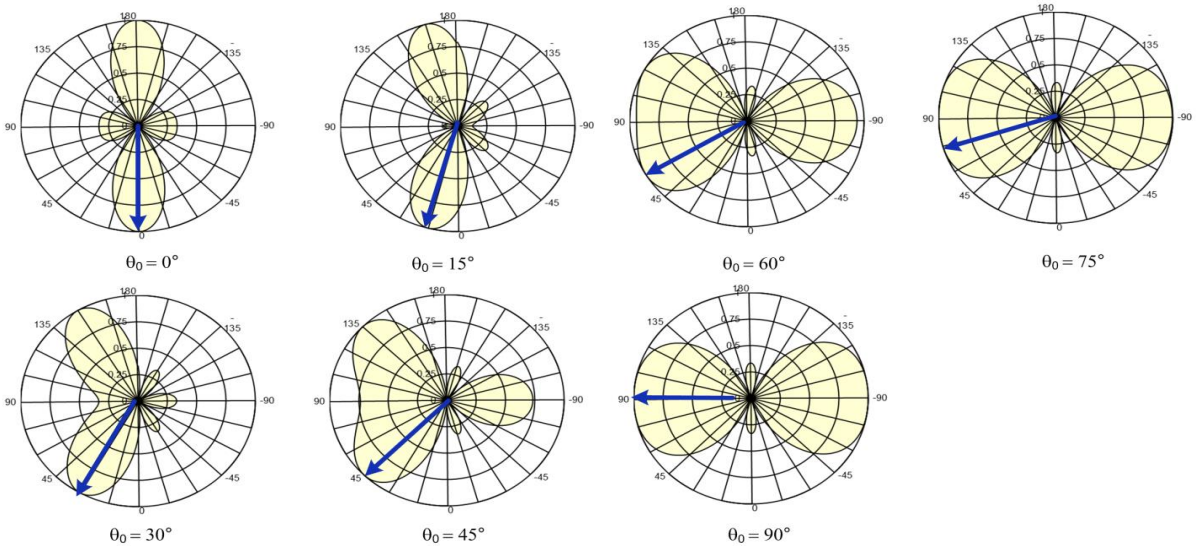

Figure 2 Beam scanning using three isotropic antenna elements.

The organization of this work on multi-element frequency reconfigurable SEVAs follows. First the design and fabrication of a multi-layer SEVA (ML-SEVA) is presented. The multi-element SEVA conformal linear array (SEVA-CLA) integrated onto a complex-

curved surface is discussed next. The last section includes measured and simulated results from these structures. A brief discussion concludes the chapter. Full-wave electromagnetic solver [63] is used for simulation of these structures.

Design and Fabrication

Multi-layer SEVA (ML-SEVA)

Figure 3 shows the CAD model and notional composite lay-up of the multi-layer SEVA (ML-SEVA) presented in this work. The design and operation of this two-layer ML-SEVA leverages advances in additive manufacturing techniques to synthesize complex co-located vascular networks that provide additional operational degrees of freedom with respect to the antenna performance metrics demonstrated by the original SEVA in [57]. The fabric lay-up for the ML-SEVA in this work features two unique vascular networks separated by a single ply low-dielectric epoxy/quartz prepreg fabric RM-2014/4581 Astroquartz® III with a 0.25 mm layer thickness. Each pair of the meandered lines that form the microchannels through which liquid metal is flowed are first extrusion-printed using the sacrificial PLA formulation in a single layer thickness of 0.6 mm onto Polyimide sheets. These two pairs of meandered lines create two distinct dipole-like configurations that are then thermally transferred to a fabric layer below the previous one and arranged according to the lay-up shown in Figure 3.

$$x(t) = \frac{t^{\alpha}}{d_0^{\alpha-1}} \sin(\pi p_0 t) \quad \text{---------(1)}$$

$$y(t) = t + s_0 \quad \text{---------(2)}$$

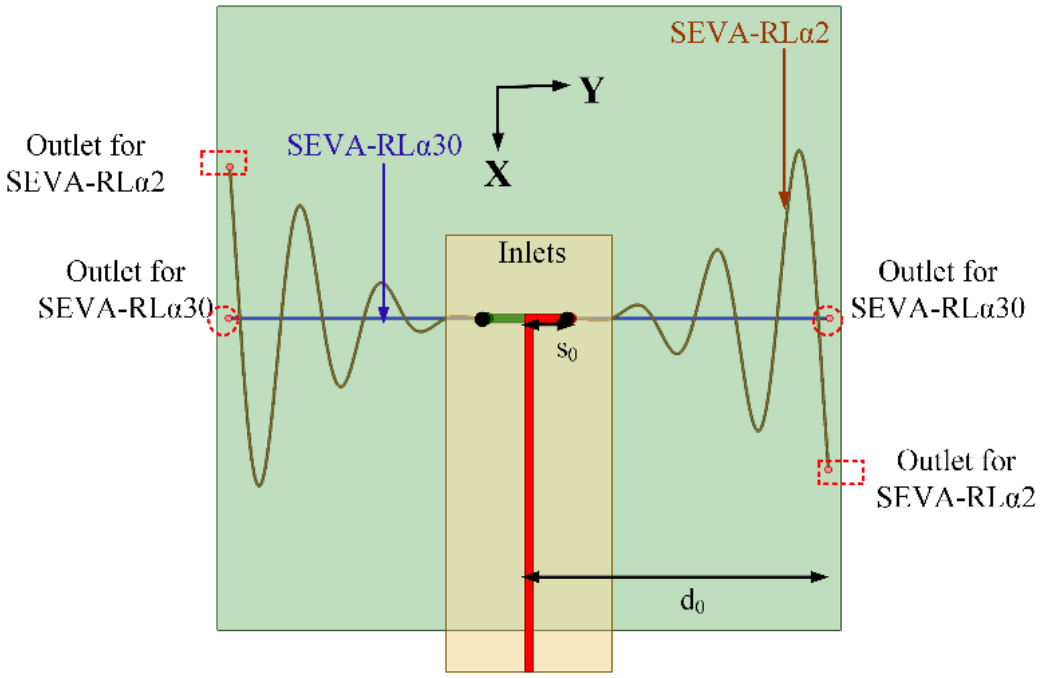

(a)

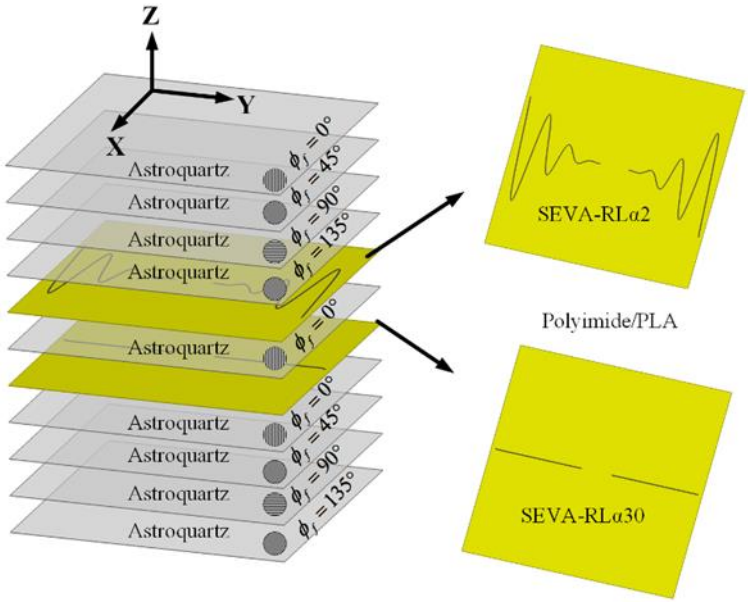

(b)

Figure 3 Detailed representation of Multi-layer SEVA (ML-SEVA) (a) CAD model used for simulating the structure (b) Fabrication lay-up.

The processing steps for this structure follow [57] by first curing the composite with embedded microchannels in an autoclave. Vertical cylindrical channels are then machined down from the top of the composite to the lowest of the two sacrificial layers (SEVA-RLα30) to provide release holes for the ablation of sacrificial materials. This is followed by a post-cure in a vacuum oven to vaporize the sacrificial material and create microvascular voids in the composite. These are inspected visually and then tested with compressed air to ensure all channels are cleared of any blockage. After this the vertical channel at each feed location $(x, y) = (0, \pm s_0)$, with s_0 = 3.94 in. (10 mm), connects the two arms of the SEVA-RLα2 and SEVA-RLα30; the remaining four only contact a single arm where they intersect $y = \pm d_0 = 2.6$ *in*.

The resulting composite with embedded microvasculature is electromagnetically functionalized by first adhering hollow copper cylindrical vias 2mm in diameter at the two feed locations. These are extended just below the surface for mechanical stability and provide access for the pressure-driven displacement of fluids into each of the four channels. These metallic vias extend upwards through drilled holes in a 31 mil (0.7874 mm) FR4 substrate (ε_r = 4.4 and $tan\ \delta$ = 0.02) where they are electrically connected (soldered) to the arms of an antipodal dipole having a length $l = 2y_0$. This antipodal dipole is fed by a parallel strip feed line with a 50 Ω characteristic impedance that is terminated in a Sub-Miniature Version A (SMA) connector for measurements. In this configuration, the transition from parallel strip line to antipodal dipole operates as a Dyson-style balun for the SEVA over the frequency ranges considered in this work. The ML-SEVA operates

as a combination of two thin wire dipoles growing outward from the antipodal dipole; the selective filling of channels is achieved by leaving the vertical channel at its opposing end unobstructed or sealing the individual vertical channels with a thermal adhesive where it intersects $y = \pm d_0$.

Multi-element SEVA Conformal Linear Array (SEVA-CLA)

Figure 4 shows the notional composite lay-up and CAD model of the mandrel used to form the composite into a complex-curved surface for the SEVA conformal linear array (SEVA-CLA). The complex-curved shape of the mandrel is not necessarily representative of a leading-edge design for a specific UAV and/or other aircraft, but it demonstrates the extensibility of the SEVA processing steps. This advancement in the additive manufacturing is leveraged in this work to fabricate a large contiguous channel embedded within a complex-curved composite with multiple access points. The structurally embedded microvascular structure can operate in a number of different radiating manifold configurations; the focus here is on its operation as a three-element linear array as well as a single contiguous antenna that extends the bandwidth of the manifold. The SEVA-CLA generally follows the processing steps for the original SEVA [57] but expands on them in terms of the dimension and geometry of the complexity of the vascular network. As with other SEVA designs, debulking of the prepreg to remove volatiles from the resin and avoid the formation of porosity is an important step before curing in an autoclave. Once cured and released from the mandrel it is drilled at the prescribed locations (at the ends of the curvilinear channels) to access the sacrificial layer. The structure is then placed in a

vacuum oven to post-cure and vaporize the sacrificial material and create the embedded microvascular network. The meandering vasculature of the three-element SEVA-CLA uses the parameterization of the SEVA-RLα2 for each of the three driven antenna elements. The curvature of the mandrel used to shape the composite is approximated for the high frequency modeling of antennas by sweeping the polynomial approximations of the "leading edge" curvature $f_z(x) \simeq 12.0\times10^{-3}x^2$ in the xz-plane along the contour "saddle path" $f_z(y) \approx 275.5\times10^{-6}y^2$ in the yz-plane. Three of the feed structures are first positioned then the array elements are first mapped conformally onto the complex-curved surface of the mandrel using; The central element has symmetric arm lengths $d_0 = d_2$ = 3.59 in. (91.44 mm) while the arm lengths for the edge elements are asymmetric with the length of one arm fixed to $d_0 = d_1$ = 2.92 in. (74.12 mm) and the other one fixed to $d_0 = d_2$ = 3.59 in. (91.44 mm). The zero crossing points (denoted by variable *t*) on y-axis extend from 0 to 2.4 in. for sinusoidal exponentially increasing dipole [64].

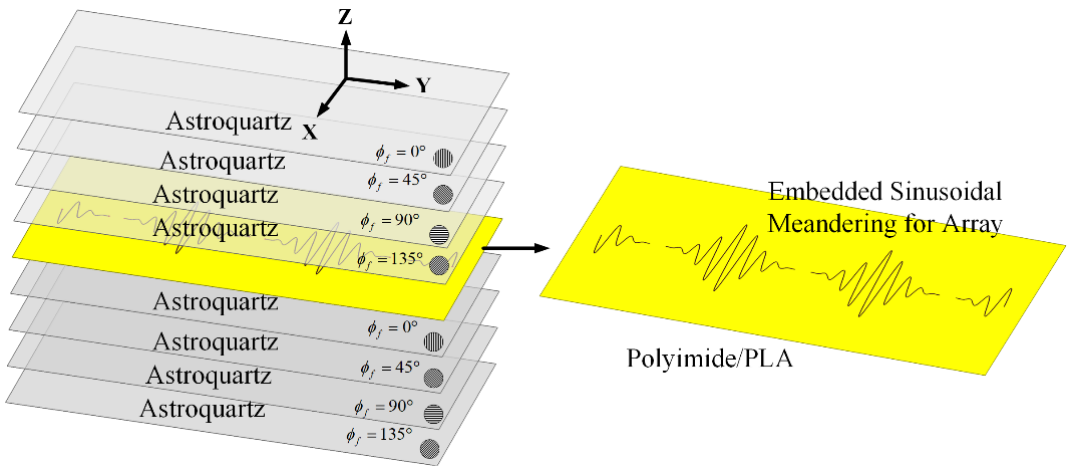

(a)

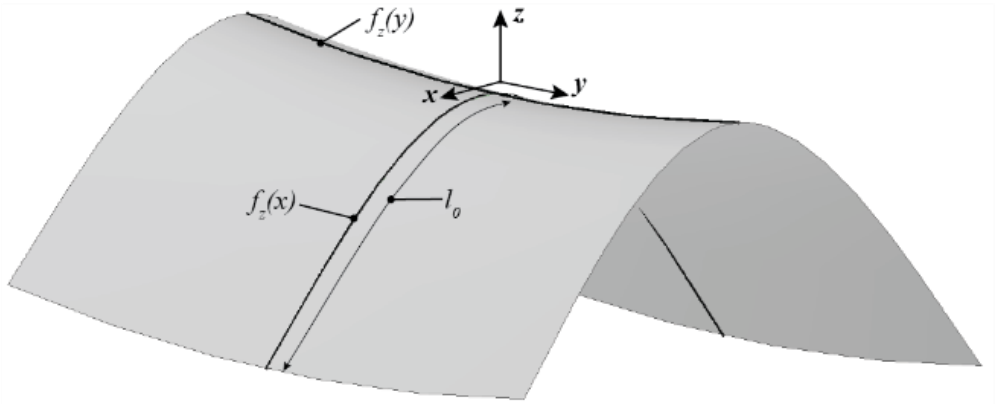

(b)

Figure 4 Detailed representation of Multi-element SEVA conformal linear array (SEVA-CLA) (a) Fabrication lay-up (b) CAD model of complex curved mandrel used for shaping the composite.

The topology and operation/role of the feed network for this structure is similar to the structure presented in Figure 3. It's 50 Ω impedance parallel strip feed lines have a length l0 = 5.78 in. (147mm) and is fabricated on 31 mil (0.7874 mm) thick RT/Duroid 5880 (εr = 2.2 and tan δ = 0.0004); this is used in place of the FR4 substrate to provide a feed network that can conform to the curvature of the composite. Figure 5 (top view) shows three feed elements connected to the sinusoidally meandered dipoles. Figure 5 (side view) shows the detailed connection between feed and embedded microvascular channels.

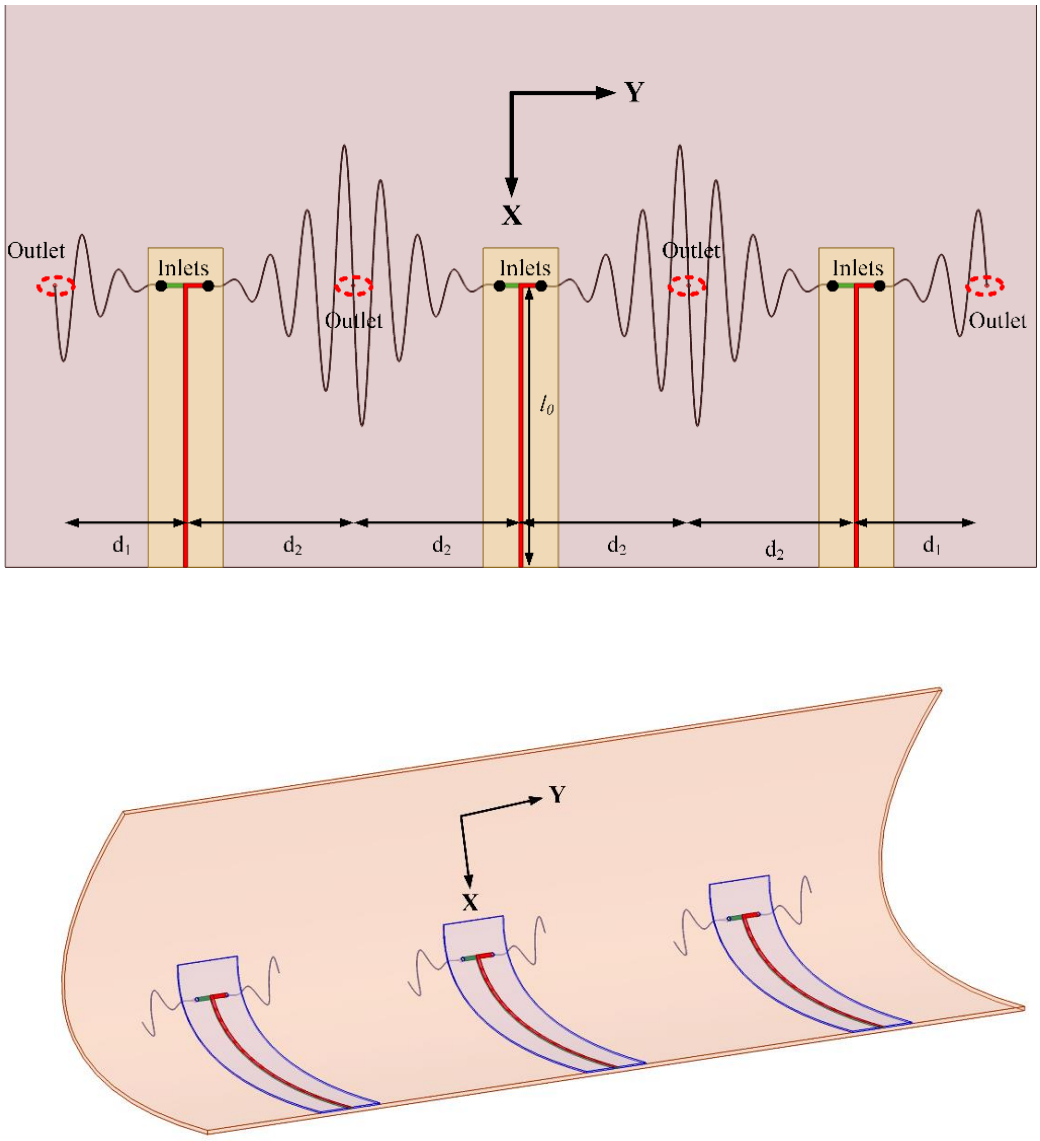

Figure 5 CAD Model of multi-element SEVA-CLA. Top view: Connection of feed elements with sinusoidally meandered dipoles. Side view: Connection of feed elements with sinusoidally meandered dipoles

Measurement and Analysis

Discussion on the transport of liquid metal in the embedded vascular channels of ML-SEVA and SEVA-CLA is presented in this section. Comparison between simulated and

measured results of these structures draw attention to the frequency reconfigurability of ML-SEVA and beam scanning ability of SEVA-CLA. Operation of SEVA-CLA as a contiguous antenna element operating in VHF is also presented in this section. Demonstration of fundamental array principles are presented by studying contour plots of isotropic antenna array and SEVA-CLA.

Multi-Layer SEVA (ML-SEVA)

Figure 6 shows the final fabricated model of ML-SEVA. The embedded microvascular channels are visible in the semi-translucent ML-SEVA. This offers a means to visibility track and measure the position of liquid metal being transported through the microchannels as well as its proximity to the zero-crossing points of the exponentially increasing sinusoidal structure (SEVA-RLα2) at t_1 = 0, 0.4, 0.8, 1.2, 1.6, 2 and 2.4 in. Corresponding values are chosen for *t2* (SEVA-RLα30) in this experiment. Selected combinations of *t1* and *t2* are presented in this article to demonstrate the principle of frequency reconfiguration in ML-SEVA. Radiation patterns observed have remain

consistent with simulation across different configurations and the selected combinations are shown for illustration.

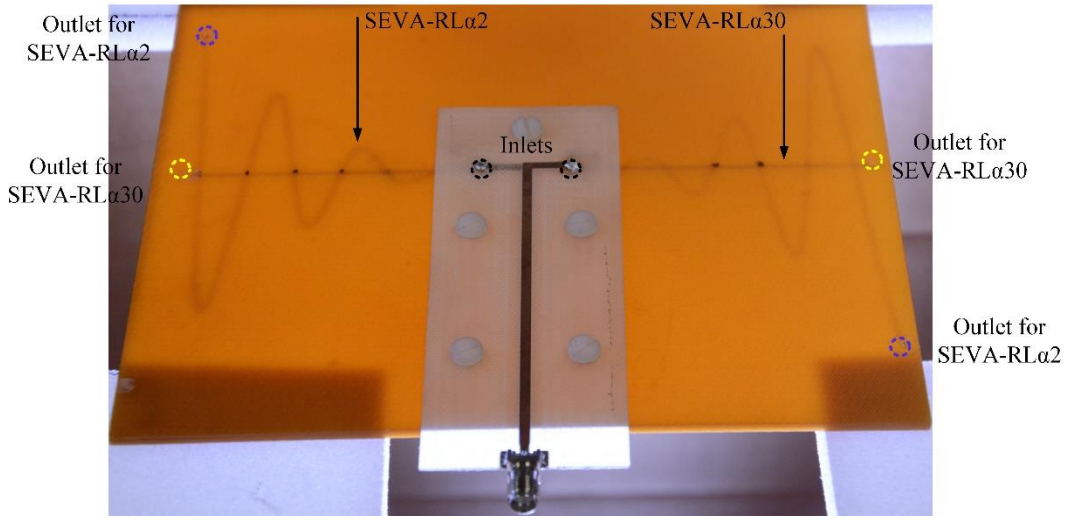

Figure 6 Fabricated ML-SEVA and feed network aligned and attached with nylon threads.

Cylindrical metallic tubes with a diameter of 2 mm are soldered to the feed and visually aligned with the opening on the embedded channels in the substrate to ensure continuous and leakage-proof flow of liquid metal from inlets towards the outlets. This also establishes electrical connection between liquid metal in the embedded channels and the feed. Additionally, for mechanical stability, the feed is affixed to the substrate by nylon screws ensuring a tight fitted connection between the feed and the substrate. Filling the embedded channels with non-conductive, low-loss, low dielectric, and heat transfer fluid Fluorinert FC-70 [65] electronic liquid before flowing liquid metal ensures smooth flow of liquid metal in the channels. When liquid metal is transported from the inlet of SEVA-RLα2 towards its outlet the outlet of SEVA-RLα30 is sealed with hot melt adhesive

(HMA) to avoid leakage of liquid metal into the undesired channel. Similarly, the outlet of SEVA-RLα2 is sealed with HMA when liquid metal is transported through SEVA-RLα30.

Figure 7 shows the measured and simulated input reflection coefficient (in dB) for the chosen combinations of *t1* and *t2*. The plots clearly demonstrate down shift of fundamental mode resonant frequency with increasing liquid metal flow in the embedded channels. These plots illustrate that the radiation pattern of the antenna remains quasi-omnidirectional for the different configurations. The close agreement observed between the measured and simulated results indicates that the operation of frequency reconfigurable ML-SEVA is also stable across the range of frequencies considered in this work. Figure 8 shows the measured and simulated E_θ and E_φ in *xy*- and *xz*- planes at the lowest value of magnitude (in dB) for the fundamental mode. When the antenna resonates at a frequency closer to the antipodal dipole (around 4 GHz) used to feed the microvascular component the antenna, the radiated pattern deviates from expectations due to increase interactions with the parallel strip feed network and other artifacts of experimental set-up. Thus, higher volume of metal in the embedded channels offers stable radiation pattern compared to lower metal volumes in the channels as with higher metal volumes in channel the antenna resonates at frequencies much lower than 4 GHz. Simulated maximum gains for configurations in figure 6 a, b, c, d is 2.3, -0.01, -3, 1.7 and -5 dBi respectively.

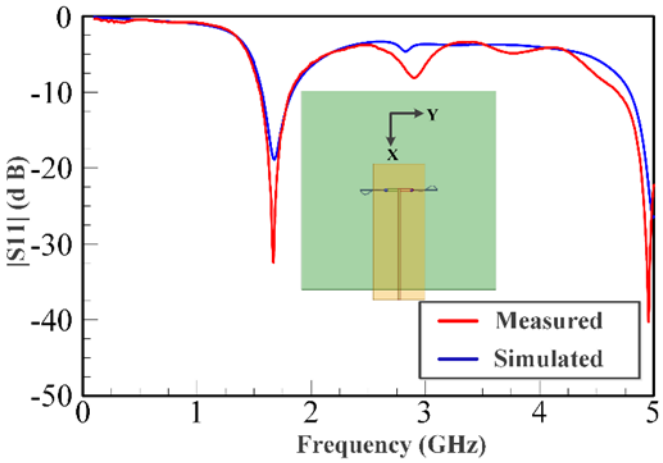
0
-10
-20
-30
-40
-50
|S11| (d B)
0
1
2
3
4
5
Frequency (GHz)
Y
X
Measured
Simulated

(a)

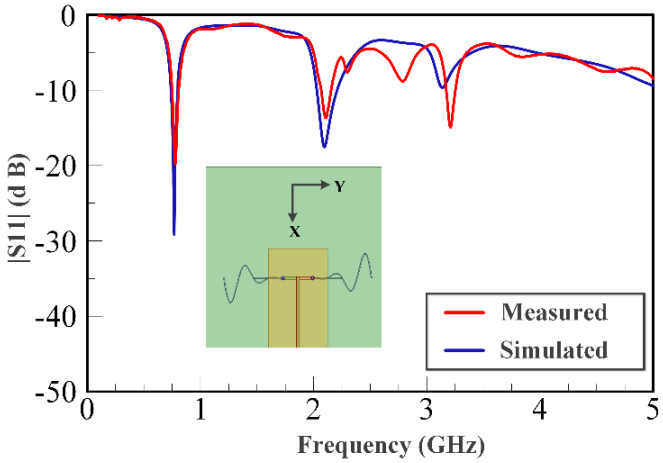
0
-10
-20
-30
-40
-50
|S11| (d B)
0
1
2
3
4
5
Frequency (GHz)
Y
X
Measured
Simulated

(b)

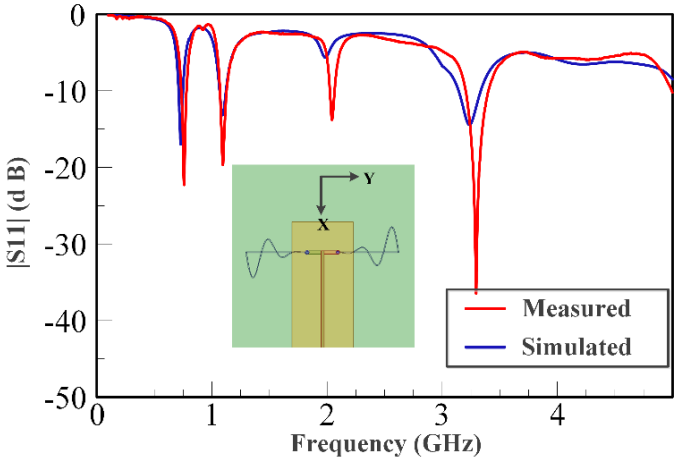
0
-10
-20
-30
-40
-50
|S11| (d B)
0
1
2
3
4
Frequency (GHz)
Y
X
Measured
Simulated

(c)

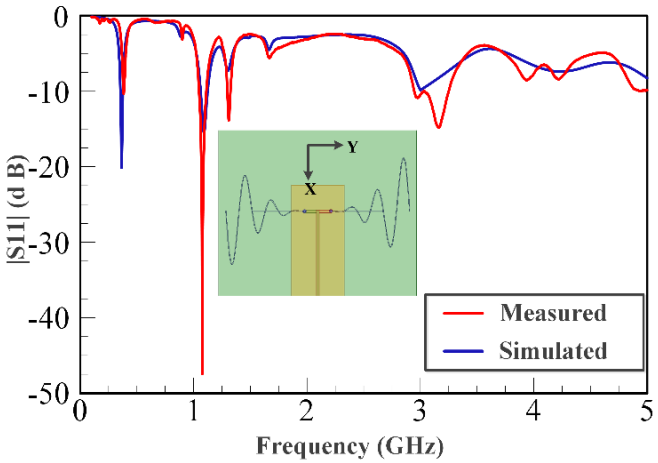
0
-10
-20
-30
-40
-50
|S11| (d B)
0
1
2
3
4
5
Frequency (GHz)
Y
X
Measured
Simulated

(d)

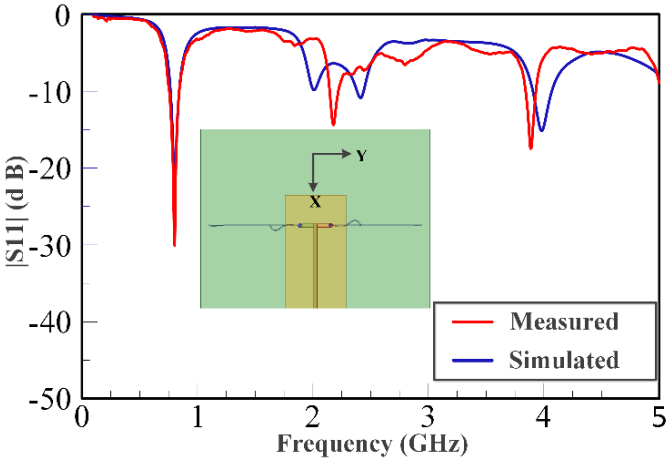
0
-10
-20
-30
-40
-50
|S11| (d B)
0
1
2
3
4
5
Frequency (GHz)
Y
X
Measured
Simulated

(e)

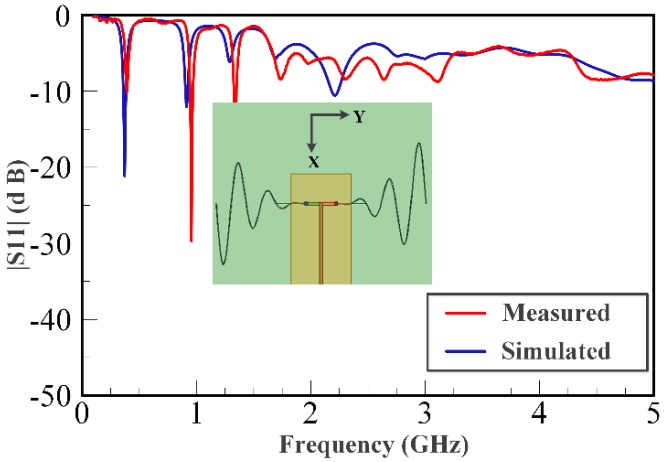
0
-10
-20
-30
-40
-50
|S11| (d B)
0
1
2
3
4
5
Frequency (GHz)
Y
X
Measured
Simulated

(f)

Figure 7 Measured and simulated S-parameter values (|S11| [dB]) for different scenarios. (a) t1 = 0.8 in. and t2 = 0.8 in. (b) t1 = 1.6 in. and t2 = 0.8 in. (c) t1 = 1.6 in. and t2 = 1.6 in. (d) t1 = 2.4 in. and t2 = 1.6 in. (e) t1 = 1.6 in. and t2 = 2.4 in. (e) t1 = 2.4 in. and t2 = 0.8 in.

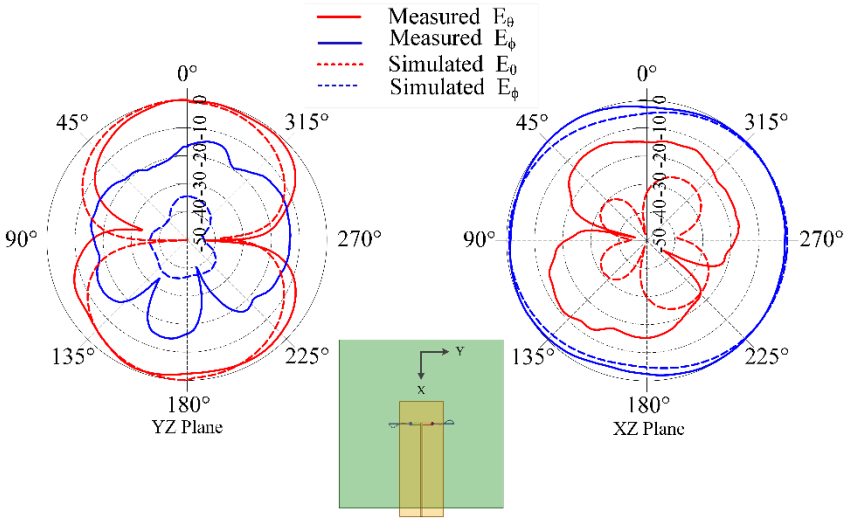

(a)

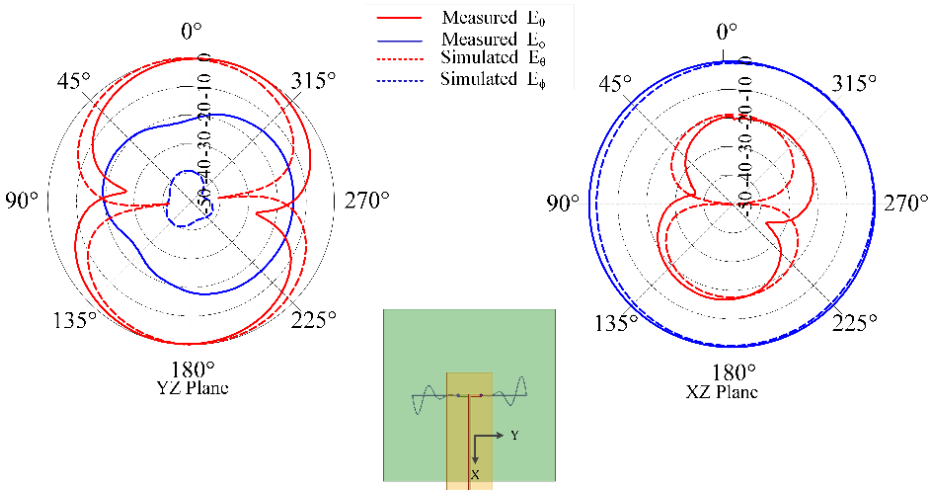

(b)

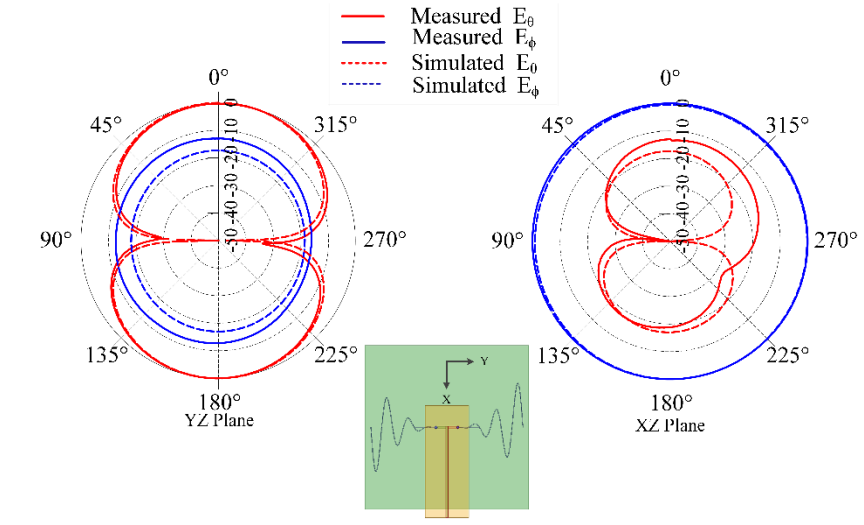

(c)

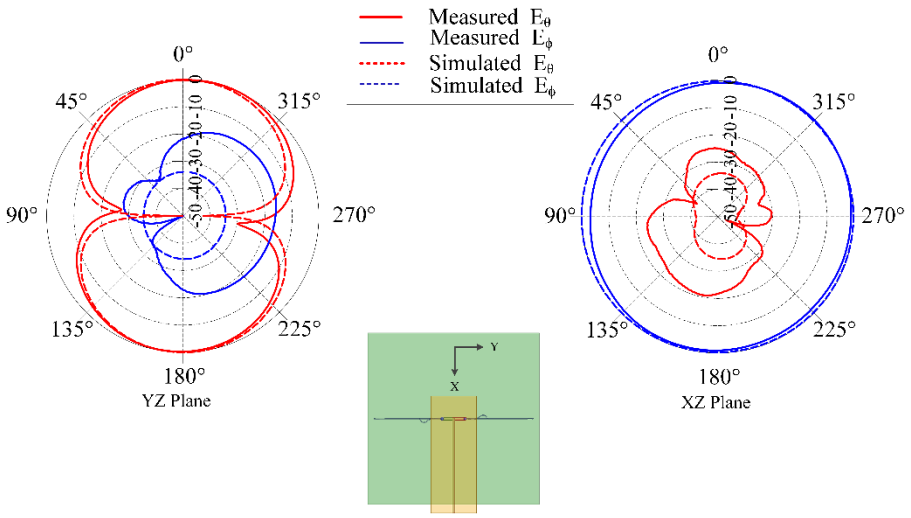

(d)

Figure 8 Measured and Simulated radiation pattern in yz- (left) and xz- planes (right) for different scenarios (a) t1 = 0.8 in. and t2 = 0.8 in. at f =1.681 GHz (b) t1 = 1.6 in. and t2 = 1.6 in. at f = 0.74 GHz (c) t1 = 2.4 in. and t2 = 0.8 in. at f = 0.372 GHz.

The effect of frequency shift (miniaturization) of the first mode at the lowest value of S11 obtained across three different configurations (SEVA-RL$_{\alpha 30}$, SEVA-RL$_{\alpha 2}$ and multilayer) are plotted in Figure 9. The multilayer structure achieves frequency downshift of 30-105

MHz compared to SEVA-RL$_{\alpha 2}$ and 120-480 MHz compared to SEVA-RL$_{\alpha 30}$ for variation of t over a range of 0 to 2.4 in.

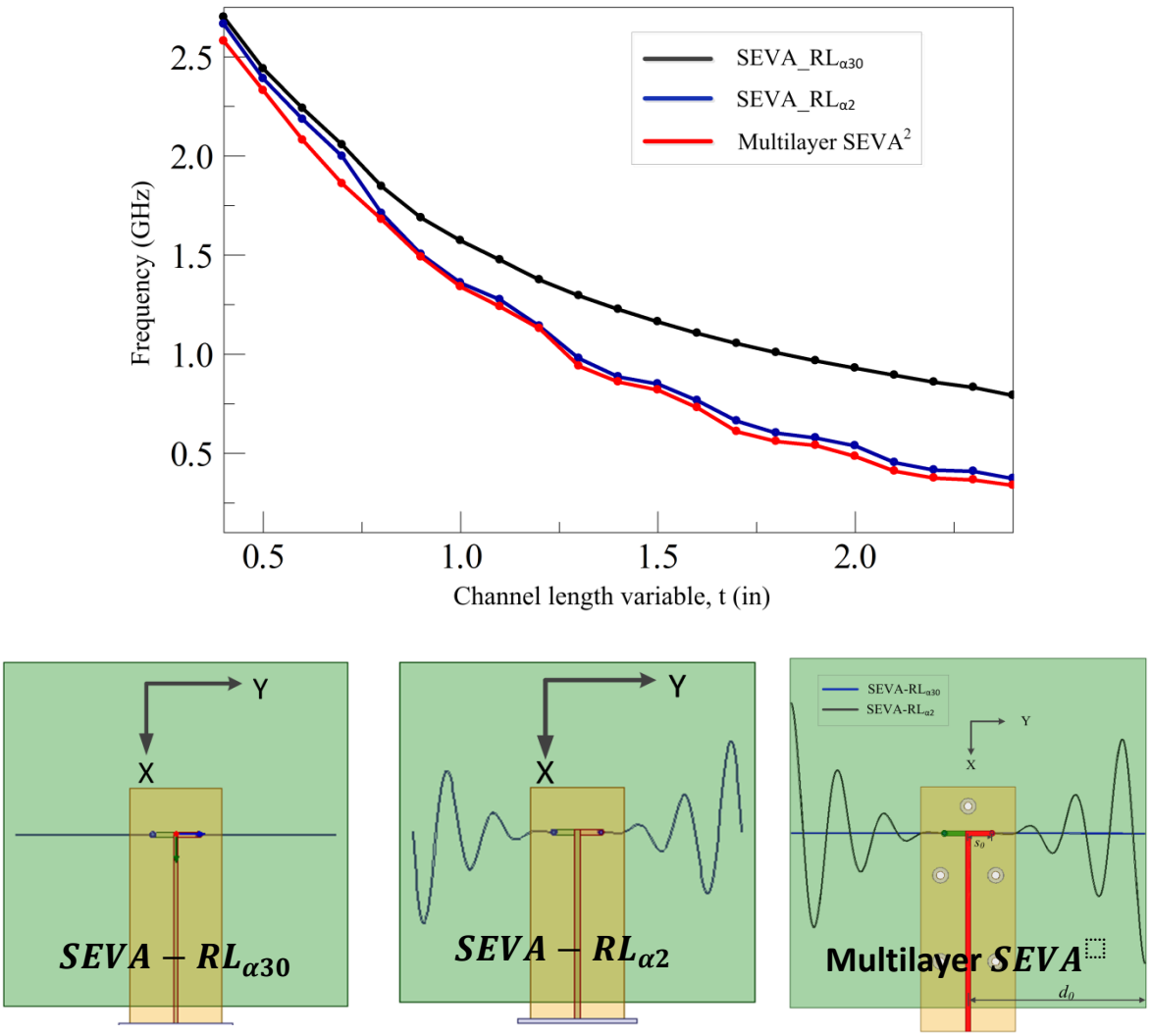

Figure 9 Frequency down-shift across three configurations

Multi-element SEVA Conformal Linear Array (SEVA-CLA)

Figure 10 shows the fabricated model of multi-element Conformal Linear Array (SEVA-CLA). Oxidation during the fabrication of the composite resulted in an opaquer panel

compared to the ML-SEVA. This limits the visibility of the embedded channels in the composite thus, the embedded channels of multi-element SEVA-CLA are filled using a different approach than ML-SEVA. Additional modifications included the use of a torus-shaped gasket formed from an HMA that was used to affix the feed structure on the curved composite. This prevents leakage of liquid metal and ensures smooth flow of liquid metal in the embedded channels.

During the measurement campaign for this antenna the embedded microchannels were first filled with FC-70 in preparation for the transport of liquid metal (to regulate back-pressure, etc.). For each of the three antennas, the antipodal dipole feed structure was first measured while the other two feeds are terminated in matched loads. Pre-measured liquid metal was then injected into the channels through the hollow via in the feed section using an appropriately tipped syringe. The amount of FC-70 flowing out from the outlets along with input reflection coefficient reading from the network analyzer was used to provide a rough estimate of the position of liquid metal in the microchannel. This was necessary as the darker color of the panel prevented visual inspection of the exact position of the fluid. This process was repeated for each element, for each of the measured configurations.

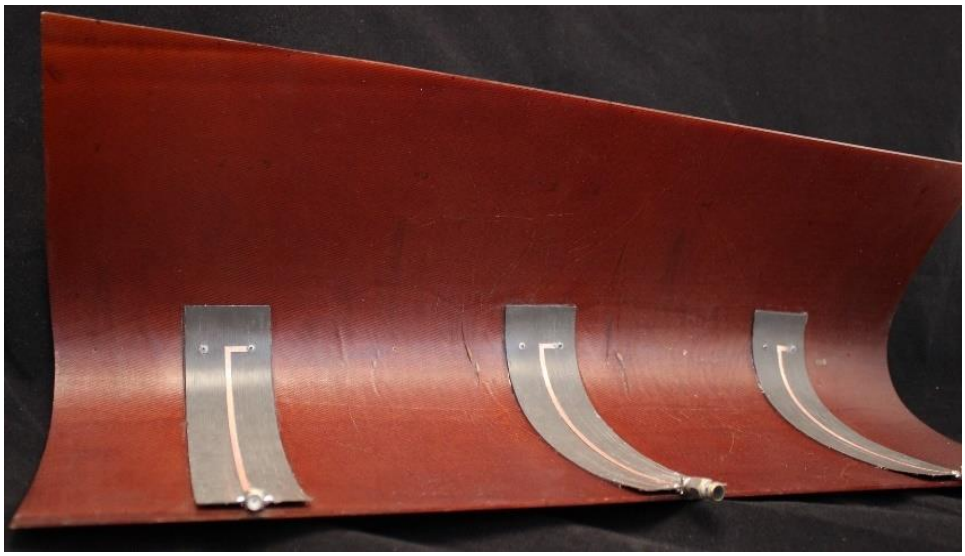

(a)

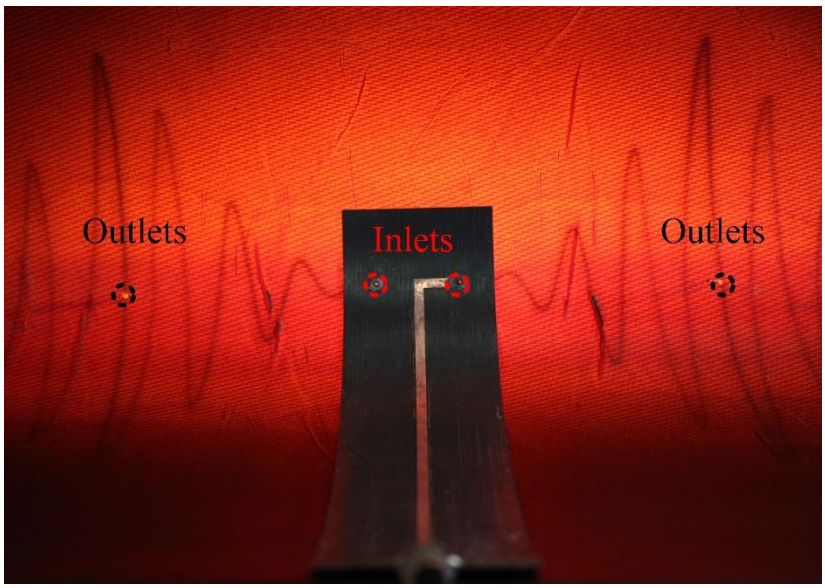

(b)

Figure 10 Fabricated model of SEVA-CLA (a) Top view showing the complete array with the three elements (b) Single element of the array with outlets and inlets indicated

Figure 11 shows the simulated and measured input reflection coefficient of the multi-element SEVA-CLA with a filling of t = 1.55 in. in each arm of sinusoidal meandering, operating at 824 MHz. A subset of the mutual impedance measurements of multi-element SEVA-CLA are compared. This configuration is chosen such that the center of the matched impedance bandwidth of the antennas (when filled with liquid metal) would provide a half-wavelength element spacing in the array. Operationally, at frequencies higher than this (when the dipole arms contain less liquid metal) the spacing become much greater than a half-wavelength and the pattern behaves as expected with the generation of grating lobes and other features. The radiation pattern of SEVA-CLA with 0-degree relative phasing between the elements is shown in Figure 12. Beam scanning by the array in the yz- plane is shown in Figure 13. Maximum beam scanning range of the array is within ±45 degrees. The principal beam of the array can be scanned by varying the progressive phase shift between the elements of the array. The phase difference between the antenna elements is varied by connecting microstrip transmission lines with pre-determined phases at 824 MHz.

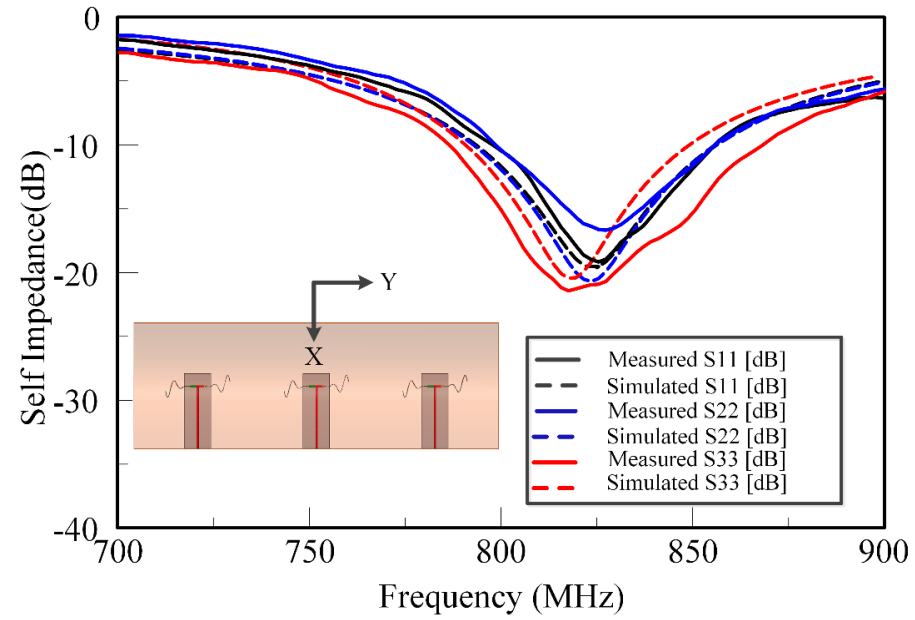

(a)

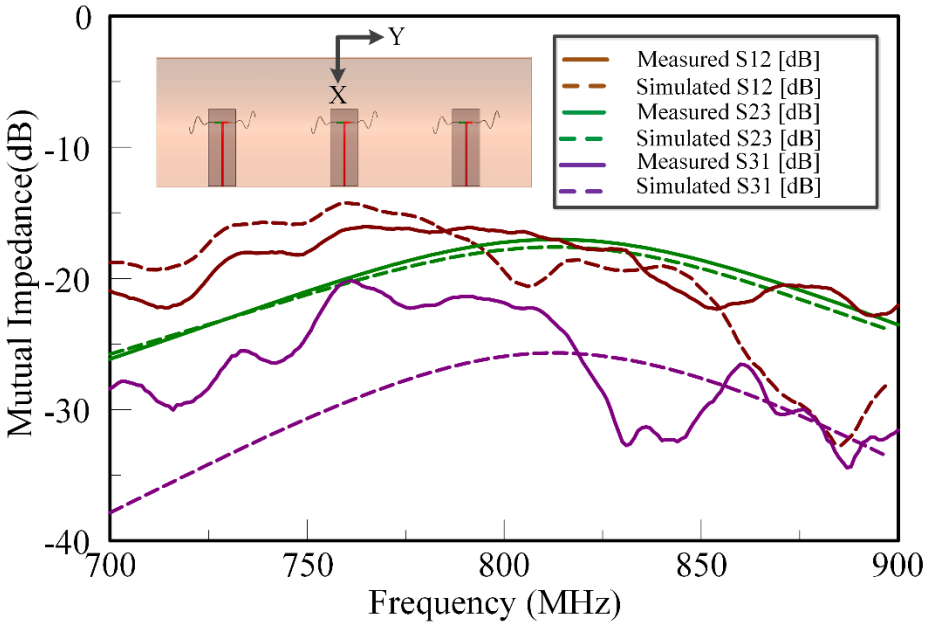

(b)

Figure 11 Measured and simulated impedance results of multi-element SEVA-CLA at 824 MHz for channel filling variable, t = 1.55 in (b) Self-impedance of the array elements (c) Mutual-impedance of array elements

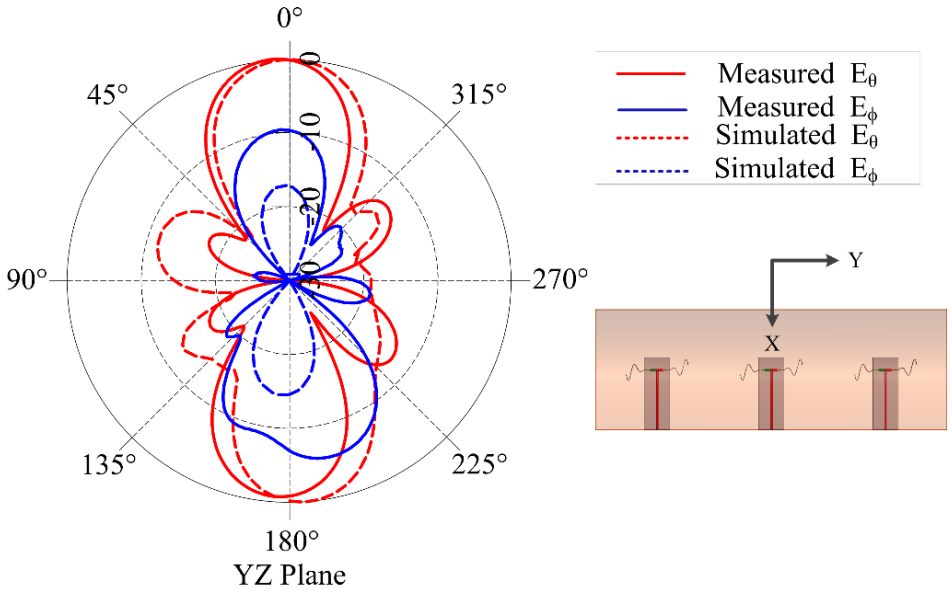

Figure 12 Radiation pattern of multi-element SEVA-CLA for an antenna array with 0-degree relative phasing at 824 MHz

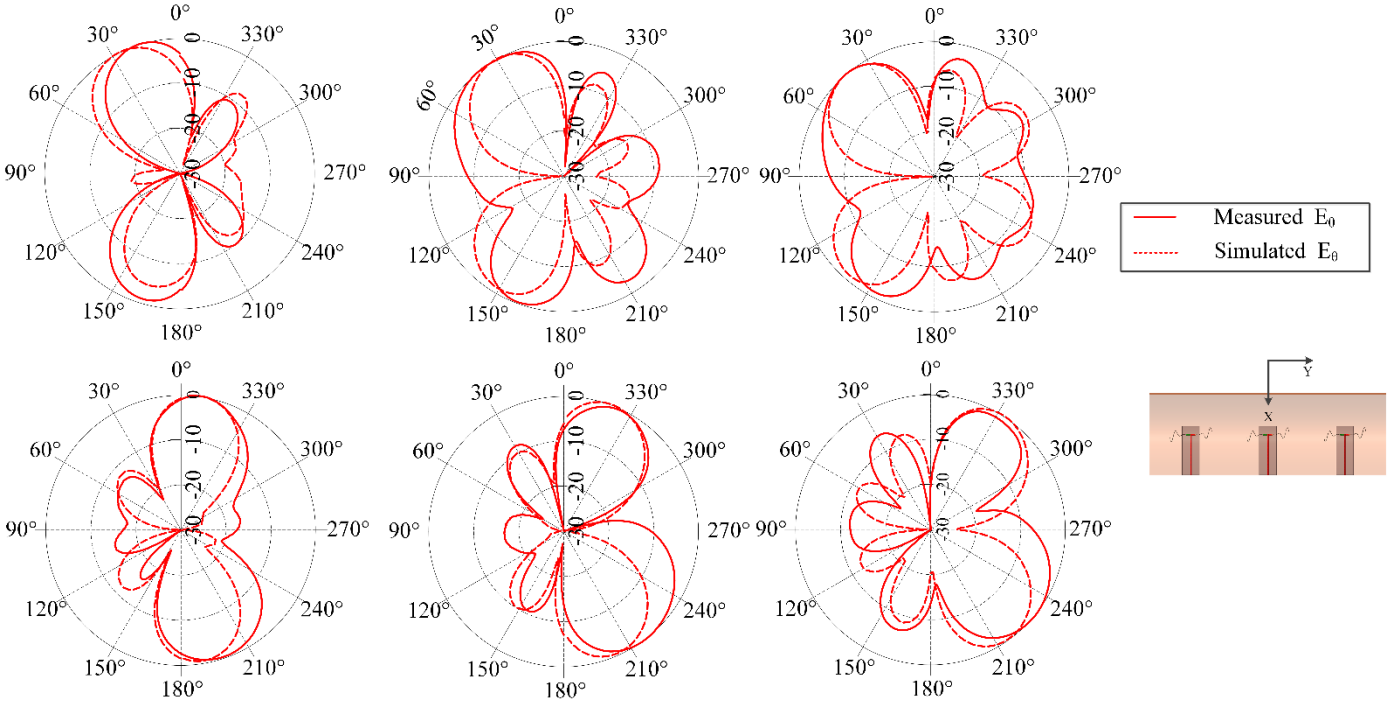

Figure 13 Beam scanning of multi-element SEVA-CLA for different scan angles at with channel filling factor t = 1.55 in. operating at 824 MHz (a) Radiated beam at ± 15^0 (b) Radiated beam at ± 30^0 (c) Radiated beam at ± 45^0

The contour plot in Figure 14 shows the array pattern for three isotropic elements spaced 183 mm apart and the three element SEVA-CLA with uniform excitation over a nominal operational bandwidth from 0.45 GHz to 4.05 GHz. The overall array pattern for multi-element SEVA-CLA is obtained by multiplying the single elemental pattern of multi-element SEVA-CLA with the array pattern of similarly spaced isotropic source. Careful examination of the two normalized gain plots testifies that the gain pattern of SEVA-CLA is obtained by multiplying the gain pattern for three-element isotropic array with the unit element pattern shown in Figure 12. Additional nulls at ±90 degrees in the SEVA-CLA contour plot are introduced by the individual elemental pattern of multi-element SEVA-CLA. The position and distribution of maxima at 0 degrees and grating lobes are similar between the two plots. Increase in the number of grating lobes in the visible region at higher frequencies is due to the widening gap between individual elements in terms of wavelength. Figure 15 shows the gain distribution of SEVA-CLA over similar frequency range (0.45-4.05 GHz). The variation in the gain pattern is attributed to the coupling between the elements with different filling factor, *t* over the frequency range. The gain of SEVA-CLA observes a dip around 2 GHz as the grating lobes start to emerge in the visible range. The efficiency of the SEVA-CLA could not be measured experimentally in the facility due to lack of available tools or in simulation but a decrease in efficiency is expected to be seen with increasing grating lobes [66].

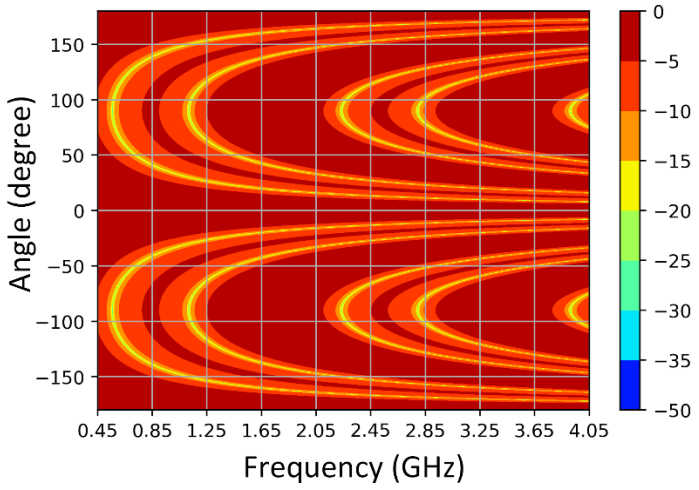

(a)

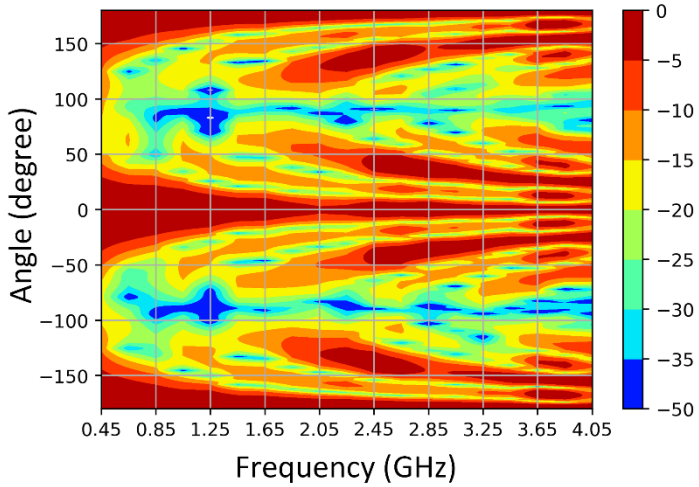

(b)

Figure 14 Simulated variation of radiation pattern with frequency (a) 3-element isotropic elements spaced 183 mm apart and (b) multi-element SEVA-CLA spaced 183 mm apart

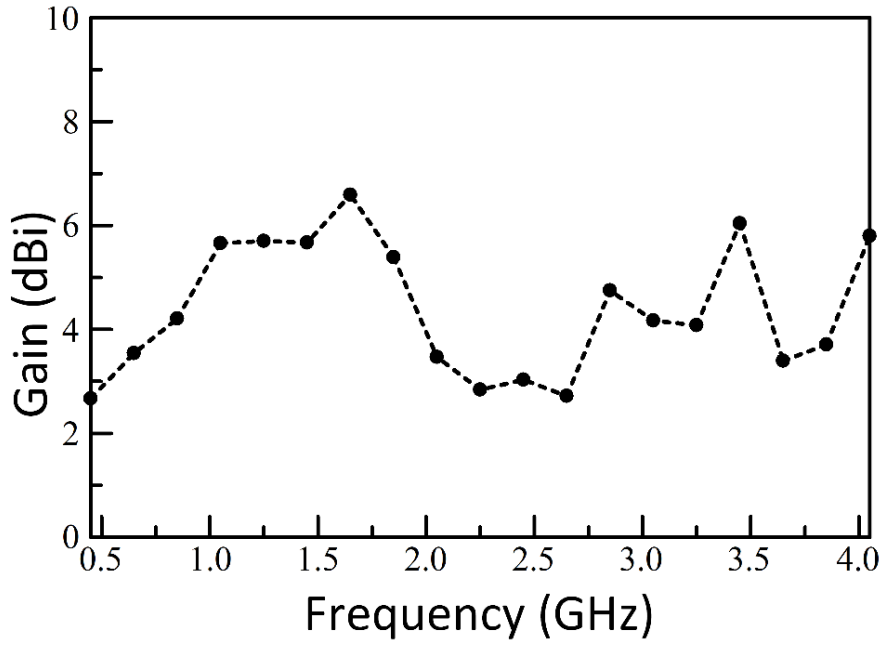

Figure 15 Simulated variation of gain with frequency multi-element SEVA-CLA

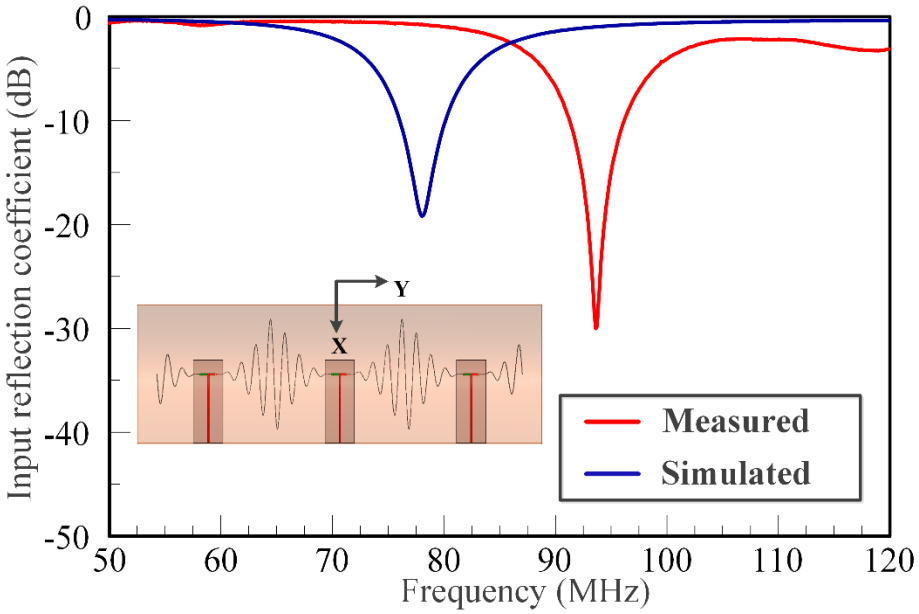

Figure 16 Measured and simulated results of multi-element SEVA-CLA operated as a single antenna element.

Figure 16 shows the measured input reflection coefficient for another unique configuration of the SEVA-CLA. This corresponds to the complete filling of embedded microchannels with liquid metal. The central element is driven in the configuration shown with the other two ports terminated in open circuits – this is one of many unique configurations that can potentially be achieved using different reactive loads and feed locations. In the form shown, the contiguous antenna structure operates as single antenna element with a matched impedance bandwidth centered at 95 MHz. The shift between measured and simulated input reflection coefficient is attributed to differences arising from fabrication and processing as well as other variations between modeled and fabricated designs.

Discussion

Current advances in the design and implementation of antennas engineered to reconfigure using the controlled transport of liquid metal through microchannel has been used to enable frequency reconfiguration, polarization reconfiguration and beam-steering [67]–[69]. These designs show the wide range of applications of antenna sensors using transport of liquid metal through microchannels suitable for varied applications over wide frequency range. These and other structures are typically single-layer design with microfluidic channels traversing a planar geometry. They open questions on the integration of these techniques for most complex host. This study demonstrates the ability to engineer multilayer and conformally curved reconfigurable antennas enabled by the transport of liquid metal in structurally embedded vascular networks. This study provides insights into the fabrication of vascular networks in two consecutive layers of fabric in the

composite lay-up. It also demonstrates the ability to embed distinct patterns in a complexly curved composite. The design, fabrication and electromagnetic functionalization of these structures leads to better understanding of the scope they provide and challenges they present. These fabrication techniques have been leveraged to create multilayer SEVA in which two co-located reconfigurable antennas have been utilized synergistically for impedance and radiation tuning. In SEVA-CLA this technique has been utilized to demonstrate beam scanning of three element array on a complex curved composite which can be reconfigured for a decade of frequency. The agreement between measured and simulated data testifies the concept and ideas presented in this paper. These design techniques can be successfully utilized in designing and fabricating embedded antennas to operate as sensors in UAVs or airplanes. This research also opens avenues in designing shape-conformal electromagnetic sensors using the concepts of microfluidics and structurally embedded vascular electromagnetic devices.

Key Contributions

- Demonstrated the ability to fabricate structurally embedded vascular antenna with two different meanderings on separate layers which are operated as a frequency reconfigurable antenna by controlled transport of liquid metal through these embedded microvascular channels.
- Utilized the concept of controlled transport of liquid metal through embedded microchannels to establish beam scanning in a frequency reconfigurable three-element antenna array fabricated on a curved mandrel.

CHAPTER III

ELECTROLESS METALLIZATION OF ADDIITVELY MANUFACTURED STRUCTURE

Fabrication and electroless metallization of additively manufactured electromagnetic components like waveguide, trough waveguide and hybrid coupler operating in 57-64 GHz, ISM band is presented in this chapter. Consumer-grade stereolithographic 3D printer is used to print these structures using pigmented acrylate-based resin. Electroless deposition of silver on these microwave components is achieved using an in-house system assembled with off the shelf components. This system is driven by a peristaltic pump, circling plating solution between silver bath and waveguide. This chapter is broadly divided into three sections. In the first section electroless metallization of WR-15, 2-inch waveguide and trough waveguide using closed-loop circulatory system driven by peristaltic pump is described. Metal plated WR-15, 2-inch waveguide section offers an average insertion coefficient of -0.35 dB. Similarly, plated trough waveguide section connected to rectangular waveguide through rectangular to trough waveguide transition shows average insertion coefficient of -1 dB. This metallization technique offers comparable results as other techniques in literature at much lesser cost and generates lower waste. In the second section, additive manufacturing and metallization of multi-port short slot rectangular waveguide hybrid couplers operating over the 57-64 GHz ISM band are presented in this chapter. The electroless deposition technique implemented for metallization of 2-port waveguides are extended for metallization of these multiport

structures. In the third section, Circular waveguide hybrid coupler operating over a frequency range of ISM band 57-64 GHz, additively printed and metal plated using the electroless technique introduced in section 2 is investigated. Effects of orientation of print and thickness of intricate structures on the performance of circular waveguide hybrid coupler are presented. Effective ways to reduce the anomalous reflections seen in the measurement results of the structure are also investigated and possible solutions for mitigating them are investigated.

Background

Advances in additive manufacturing (AM) techniques for microwave and millimeter-wave components have enabled fabrication of lower precision structures in lesser time and at lesser cost. Three-dimensional (3D) printing technologies like stereolithography (SLA) and polyjet uses non-metallic polymer resin while, selective laser melting (SLM) uses metallic composites for printing various structures. Microwave components printed using these technologies are discussed in [70]. Waveguide components printed using non-metallic polymer resins require metal deposition for successful operation as electromagnetic structures. Stereolithographic (SLA) three-dimensional (3D) printing techniques are increasingly used in the manufacture of passive microwave components for their high printing resolution and relatively low cost. Acrylate based photosensitive resins are used for printing these components. Major challenge lies in converting non-conductive acrylate-based structures to conductive microwave components. Different metal plating techniques for achieving suitable skin depth at target frequency are discussed and explored

in literature. Electroless deposition of copper or nickel followed by electro-deposition is popularly used for metal plating waveguides and antenna structures [70]–[72]. Split block techniques are incorporated for successfully electroplating waveguides and antennas. These structures have slightly degraded transmission performance compared to structures without cracks. Electroless deposition of copper on plastic is discussed in [73], [74]. The main copper deposition step is preceded by various other important steps like etching, activation, acceleration etc... Simple one step process of depositing silver in electroless manner is presented in [75]. The acrylate-based waveguides are dipped in silver bath for successful silver deposition. In this chapter electroless metallization of 2-port and multi-port electromagnetic structures operating over a frequency range of 57-64 GHz is investigated. Rectangular and circular waveguide hybrid coupler structures are designed, fabricated, metallized, measured and analyzed.

In the first section of this chapter, design, printing and metallization of V-band waveguide and trough waveguide operating in 57-64 GHz industrial, scientific and medical (ISM) radio band are presented. Silver plating bath is circulated inside the waveguides to obtain uniform plating on the edges and flat faces. A system composed of 12 V, 5000 RPM peristaltic pump, syringe and waveguide connected through silicone-based tubing is designed. Calculated ratios of Tollens reagent to dextrose are mixed in the syringe and the plating solution is circulated through the waveguide, until the solution becomes clear. The pump coating system offers comparable results as dip coating technique investigated in [75], using lesser volume of plating solution. Details of waveguide design, printing and

metallization are discussed in this chapter. Metallization is an important process in the fabrication of electromagnetic components which enables minimization of radiation losses from electromagnetic waves propagating through a metallic guided media. Appropriate thickness of deposited metal is governed by skin depth which is a function of frequency of operation and conductivity of metal, given by equation (3). Skin depth is inversely proportional to the square root of frequency, f, permeability, μ and conductivity, σ. Skin depth is a measure of how far electrical conduction takes place in a metal. At DC frequencies the whole depth of metal is consumed for current conduction but as the frequencies increase the current flows near the surface of metal instead of penetrating deeper.

$$\delta = \frac{1}{\sqrt{\pi f \mu \sigma}} \qquad \text{---------(3)}$$

The WR-15 waveguide is operated with its fundamental mode of propagation, TE10. The current distribution of TE10 rectangular waveguide is shown in Figure 17. Simulation results shows improvement in insertion coefficient of a 2-inch rectangular waveguide section with added metal thickness for fixed surface roughness as shown in Figure 18. Variation of surface roughness in accordance with the reported values in literature [76], [77] indicates minimal change in insertion coefficient.

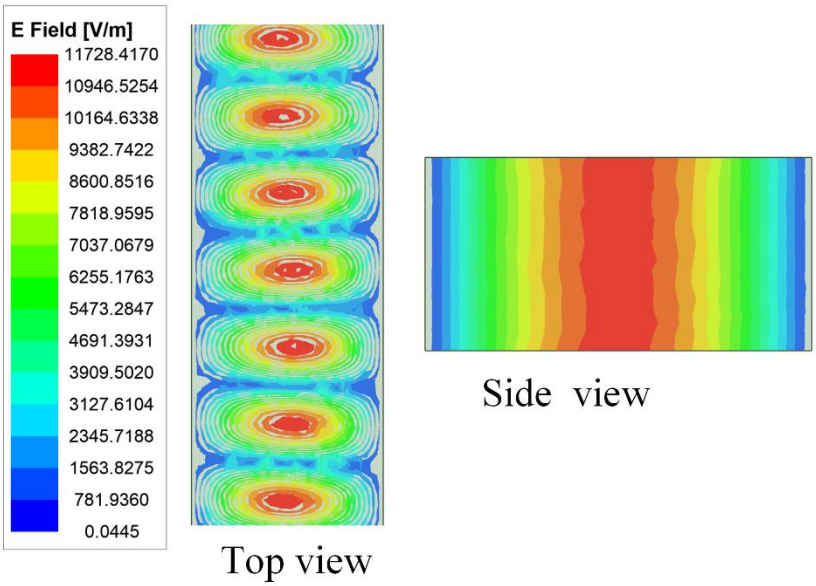

Figure 17 Field distribution in WR-15 waveguide

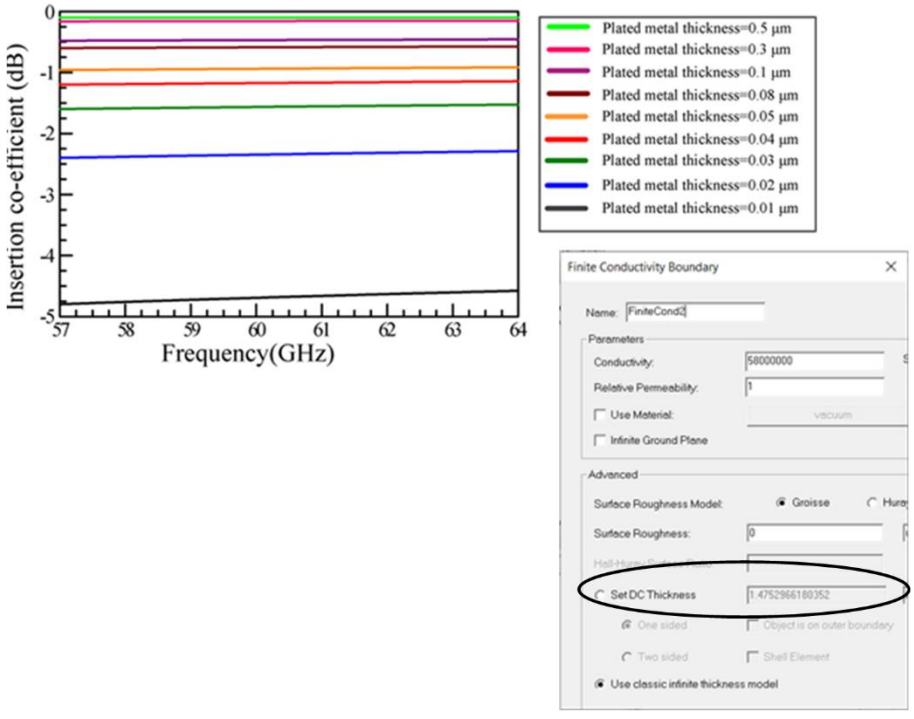

Figure 18 Simulation results indicating the improvement in insertion coefficient with increased deposited metal

In the second section of this chapter 3D printing and electroless silver deposition of WR-15 hybrid coupler operating over 57-64 GHz is investigated. Hybrid couplers are directional couplers which divides input power equally between output ports that is THRU and COUPLED Ports. No power is incident on the ISOLATED port. Additionally, the phase at the output ports THRU and COUPLED are 90 degrees apart from each other.

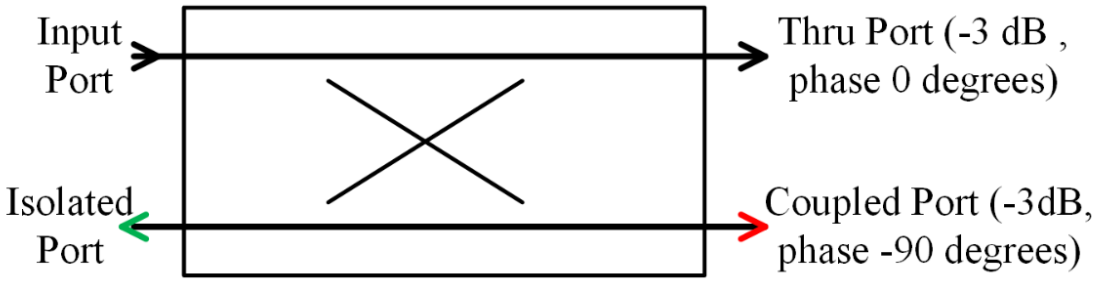

Figure 19 Line diagram of hybrid coupler

The hybrids terminated with E-bend and H-bend are analyzed. Electroless silver plating using pump-driven circulatory technique introduced in the first section is modified for multiport structures. Fluid flow in the multiport structures are investigated for successful metallization of these hybrids which had been leveraged and employed for metallization of other multiport structures.

The third section of this chapter aims to draw attention on the 3D printing inaccuracies and their effects on the performance of the structure. Simulation results of hybrid coupler are compared with measured structure with print inaccuracies. The intricate geometrical features consisting of group of ridges at the center of the structure and the vertical posts

are prone to inaccurate prints. The authors aim to focus on the deviation between measured and simulated results due to print inaccuracies. Adopted techniques to alleviate the issues seen due to fabrication errors are also explored here.

Electroless Metallization of WR-15 Waveguide and Trough Waveguide

CAD model of the 2-inch WR-15 waveguide and trough waveguide is shown in Figure 20 and the metallized waveguide structures are shown in Figure 21. The trough waveguide is connected to the rectangular waveguide through an RWG-TWG transition. Total length of the combined structure is 85 mm. Both waveguides are terminated with UG-385/U flange for electrical connection with commercial connectors.

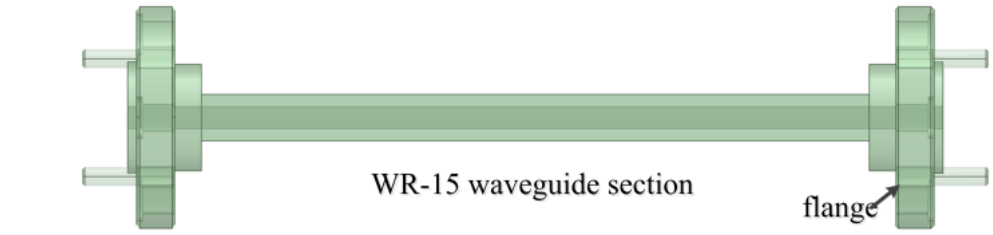

(a)

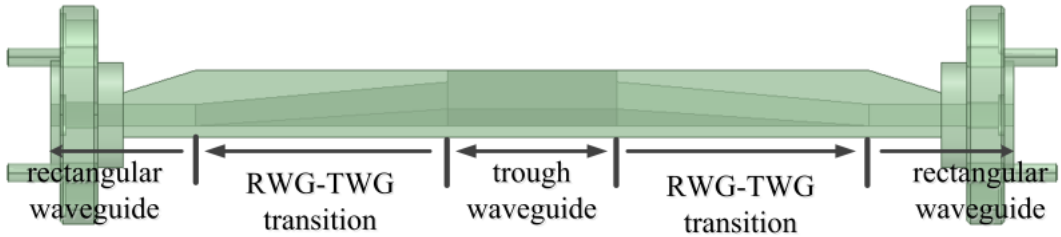

(b)

Figure 20 CAD model of the electroless silver plated waveguides (a) 2-inch WR-15 trough waveguide section. (b) Trough waveguide connected to rectangular waveguide through RWG-TWG transition.

Figure 21 The metal plated 2-inch WR-15 waveguide section and trough waveguide

Fabrication

WR-15 2-inch waveguide section and trough waveguide are 3D printed by SLA based printer with resolution of 25 microns. The waveguides are oriented approximately 45 degrees to the surface of the build plate to ensure accurate print with relatively lesser number of supports. The printed waveguides are washed for 10 minutes in 90 % alcohol bath to remove loosely attached resin. These structures are dried in strong flow of air immediately after the wash. They are cured at 60^{o}C for 60 minutes, after being left to dry further at room temperature for 45 minutes.

Slightly different approaches are taken for silver plating the two structures. Electroless plating of WR-15, 2-inch waveguide section is discussed first. Silver plating solution is prepared following the steps mentioned in [75]. The assembled system and flow diagram of the pump coating system is shown in Figure 22. The flow chart showing the preparation of Tollens reagent is shown in Figure 23. 0.5 grams silver nitrate is mixed with 25 ml of

water to which ammonium hydroxide is added till the color of the solutions turns from brown to clear. 0.35 grams sodium hydroxide dissolved in 25 ml of water is added to the original solution containing silver nitrate, which turns the color of the solution brown. This is followed by adding ammonium hydroxide to the solution which again turns the color of the solution clear. The resultant solution is Tollens reagent. The pump coating system is cleaned with isopropyl alcohol followed by distilled (DI) water. 5 ml of Tollens to 1 ml of dextrose solution are mixed in the syringe. The plating solution obtained on mixing Tollens and dextrose solution is deep brown in color. The plating solution is circulated in both clockwise and anticlockwise directions, with approximately 5 seconds in each direction. The solution starts getting clearer as time passes and silver keeps depositing. It takes approximately 3 minutes for the solution to turn clear from deep brown color. The solution that remains as a by-product of the process is discarded and the pump coating system is thoroughly cleaned with DI water only. The whole process mentioned above is counted as one run. After five such runs the waveguide offered an average insertion coefficient of -0.35 dB and further improvement in insertion coefficient with more runs is not observed. After 2-3 such runs the waveguide is cleaned using a sonic based system to remove any precipitate deposited inside the structure during plating. Removing the precipitates offers better plating and significantly better results. Over-exposure of waveguide in sonic based cleaning system is avoided to prevent removal of plated silver. Removal of plated silver decreases the thickness of coating on the walls and increases surface roughness, thus degrading the performance of waveguide.

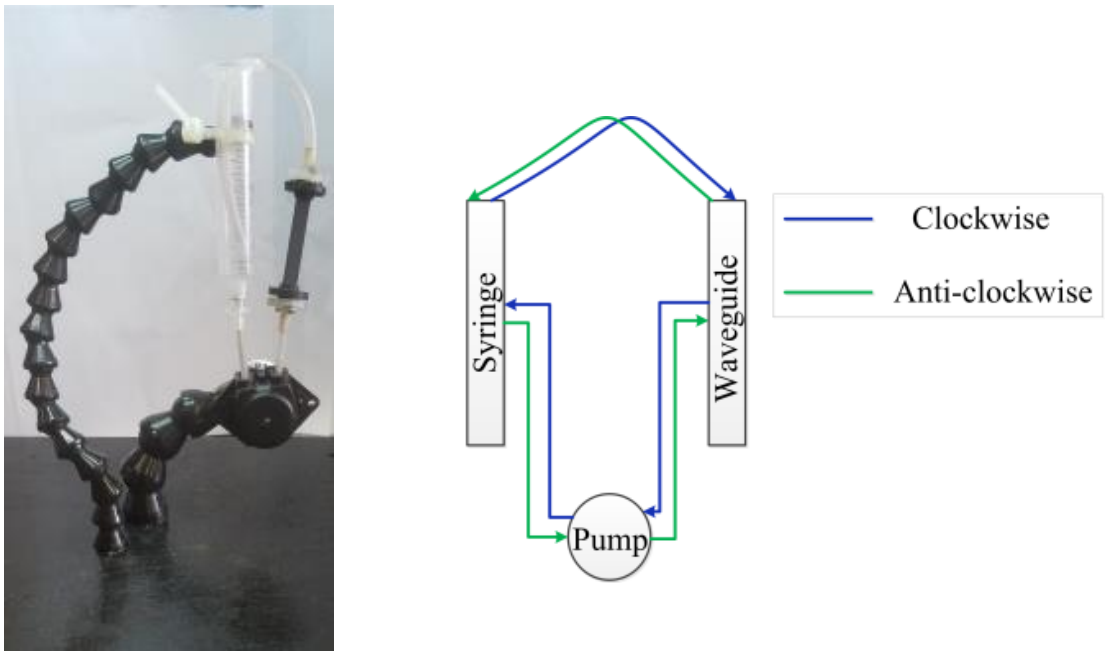

(a) (b)

Figure 22 Pump coating system used for electroless silver plating of waveguides (a) The actual assembled system with pump, syringe and waveguide (b) Flow diagram of pump coating system

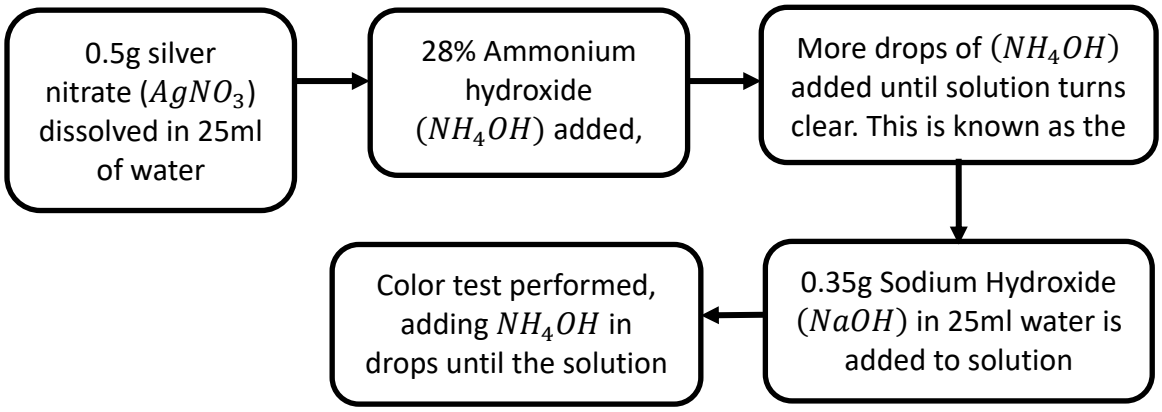

Figure 23 Flow chart showing in preparation of Tollens reagent in laboratory

The exposed trough waveguide section renders it difficult to form a continuous flow system. The trough section is wrapped with plastic paraffin film followed by electric tape, forming a good sealant. The volume of solution is incremented based on available syringe capacity, surface area of target waveguide and visual inspection of plating obtained after first run. 20 ml Tollens to 4 ml dextrose is used for the plating solution. The open trough waveguide section was vulnerable to losing plated metal in sonic cleaning. Thus, the plating solution flowing into the waveguide section attached in filtered. The filter is attached to the syringe and the pump coating system is operated in anticlockwise direction only. This significantly reduced the precipitate deposited inside the whole waveguide section. The plated section is immersed in sonic cleaner for nearly 2-3 seconds with the trough section covered. Total number of runs required for this structure is six. Any run beyond six did not offer better insertion coefficient value. The structure is cleaned after every 2 runs.

Measurements

The insertion coefficient measurements for both structures are obtained after performing response calibration. Set up for response calibration and result of response calibration is shown in Figure 24. Reflection coefficient is measured after full calibration of network analyzer. Without the added filter or ultrasonic cleaning significant change in the insertion coefficient could not be seen as indicated in Figure 25 for 5 and 7 runs. This study concluded the accumulation of precipitate during the metallization process not reported earlier in literature for similar electroless metallization technique. The deposited

precipitates increased the surface roughness value significantly. Measured results are compared with simulated results for WR-15 and trough waveguide in this section.

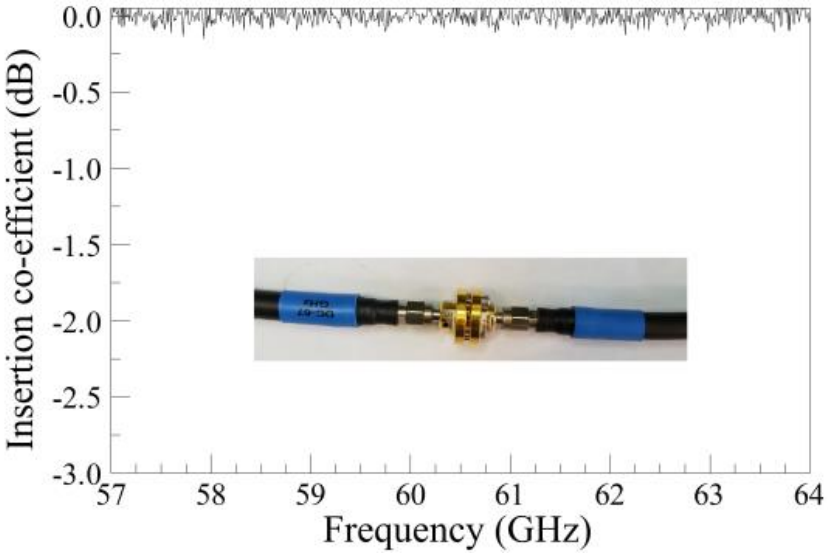

Figure 24 Response calibration set-up and result of response calibration

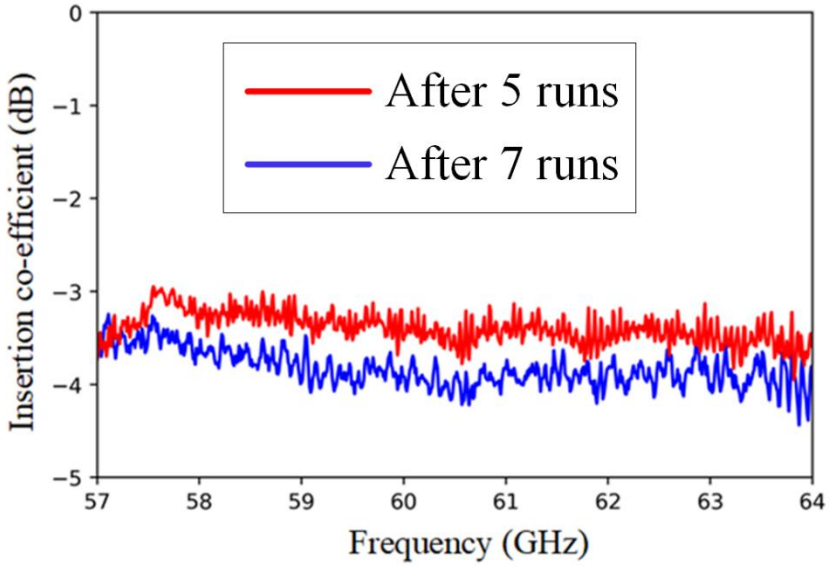

Figure 25 Measured insertion coefficient after 5 and 7 runs.

Insertion coefficients for both structures are presented in Figure 26 and reflection coefficients for both structures are presented in Figure 27. Average insertion coefficient of WR-15 waveguide section is -0.35dB and that of trough waveguide system is -1dB. The reflection coefficient of WR-15 waveguide section and trough waveguide system is below -14dB and -12dB respectively for the whole frequency range.

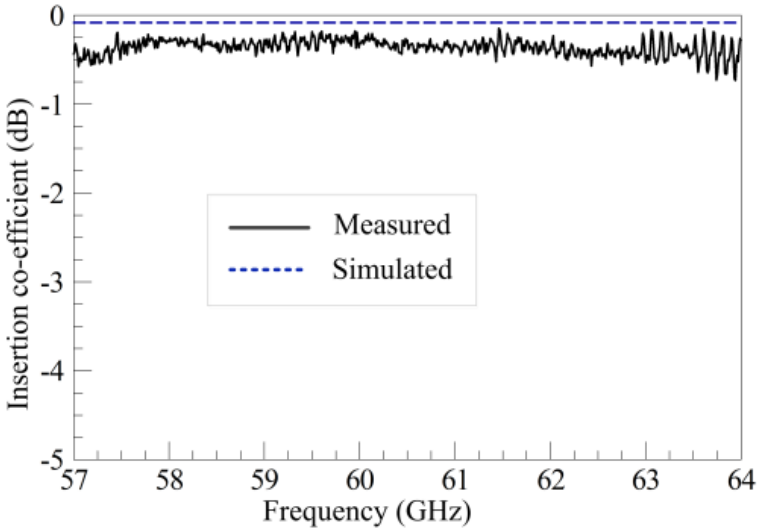

(a)

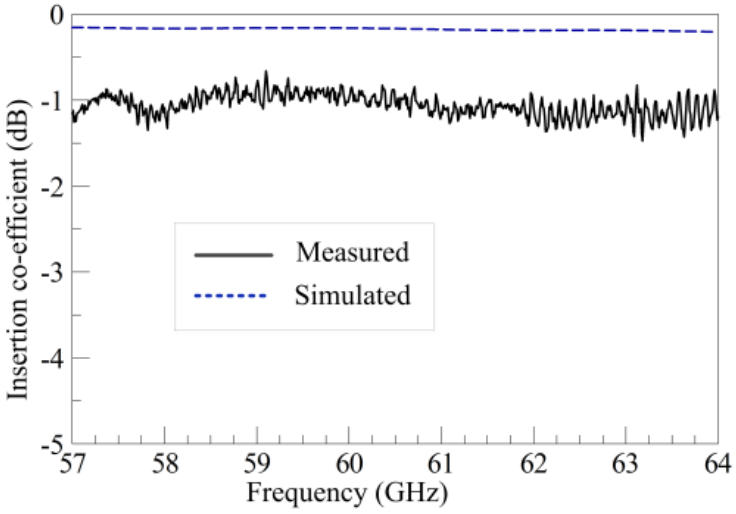

(b)

Figure 26 Measured and simulated results of insertion co-efficient (a) WR-15 2-inch waveguide section (b) Trough waveguide section with transitions

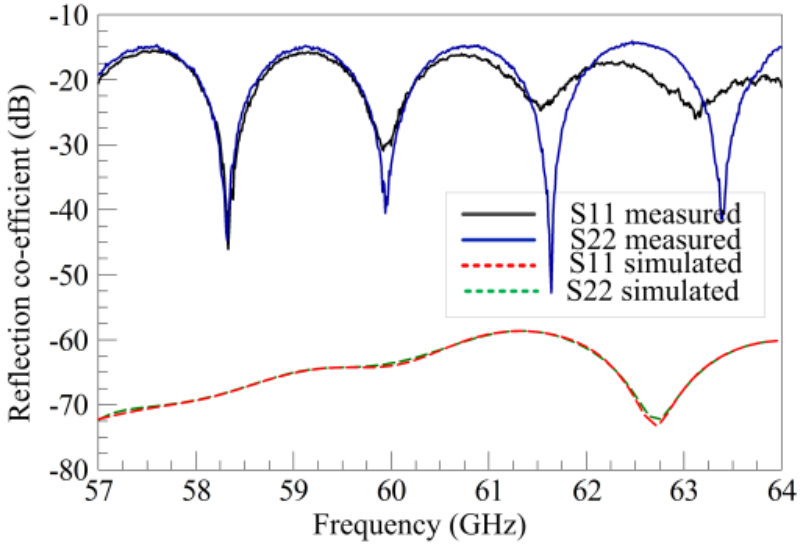

(a)

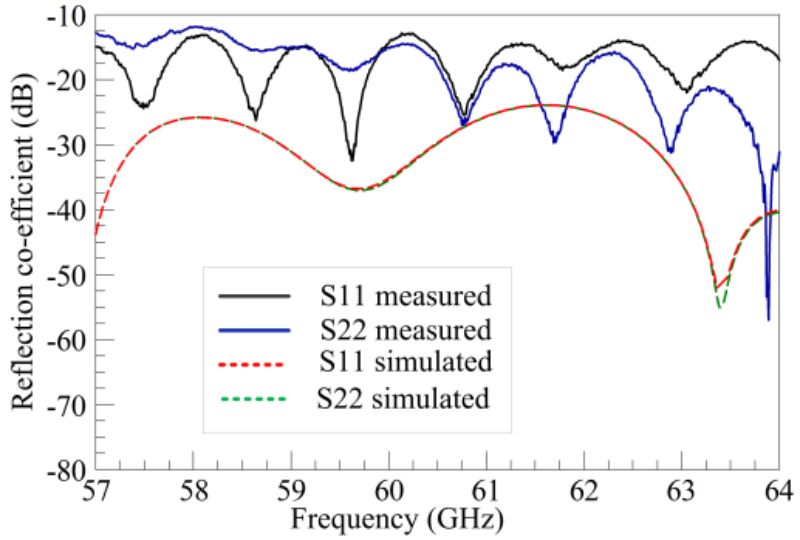

(b)

Figure 27 Measured and simulated results of reflection co-efficient. (a) WR-15 2-inch waveguide section (b) Trough waveguide section with transitions

An improvement in the overall metal deposition process is observed when the pump coat system has a commercial syringe filter attached at the end of the syringe and silver bath is rotated only in anti-clockwise direction. The deposition of silver is near flawless and the step involving sonic bath cleaning is not required. Mixture of 10 ml Tollens to 2 ml dextrose solution is used for each run. Syringe filter is replaced for each new run. The desired result of insertion coefficient is obtained after 5 such runs. The metallization procedure is carried out on a 4 mm section of trough waveguide shown in Figure 28. The final assembled system with syringe inserted in the path of silver bath flow is shown in Figure 29. The measured reflection and insertion coefficient are shown in Figure 30.

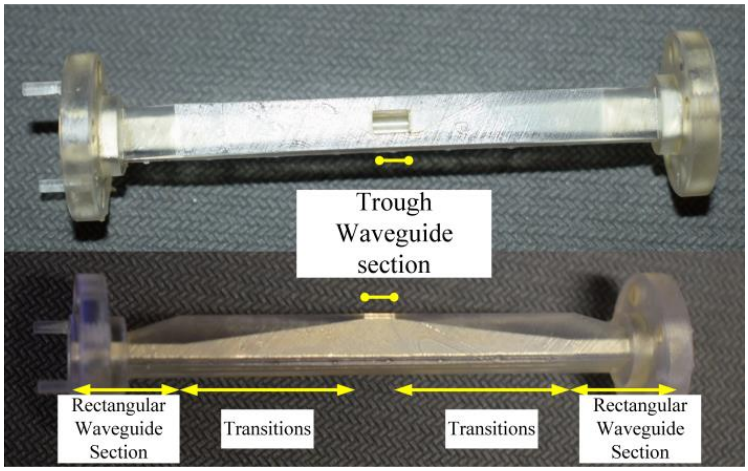

Figure 28 3D printed and electroless silver plated trough waveguide
[1]

[1] Copyright © 2019, IEEE, Reprinted, with permission, from A. Bal, A. Tiwari and G. H. Huff, "Electroless Silver Plating of Additive Manufactured Trough Waveguide Mode Transducer and Antenna Structure" accepted for publication in International Symposium on Antennas and Propagation and USNC-URSI Radio Science Meeting.

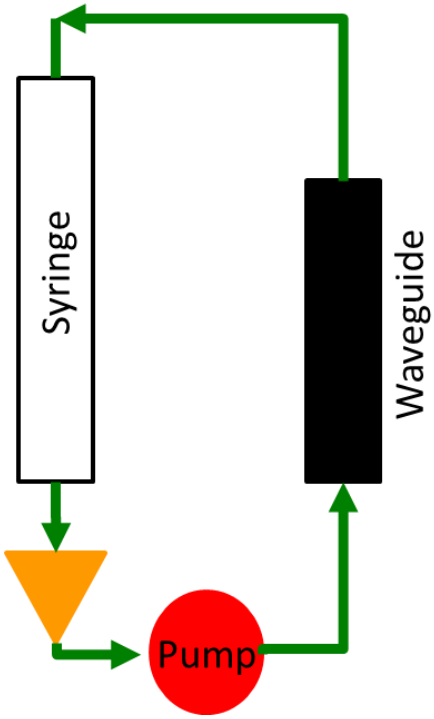

Figure 29 Flow diagram of circulatory system with syringe filter in the path of flow

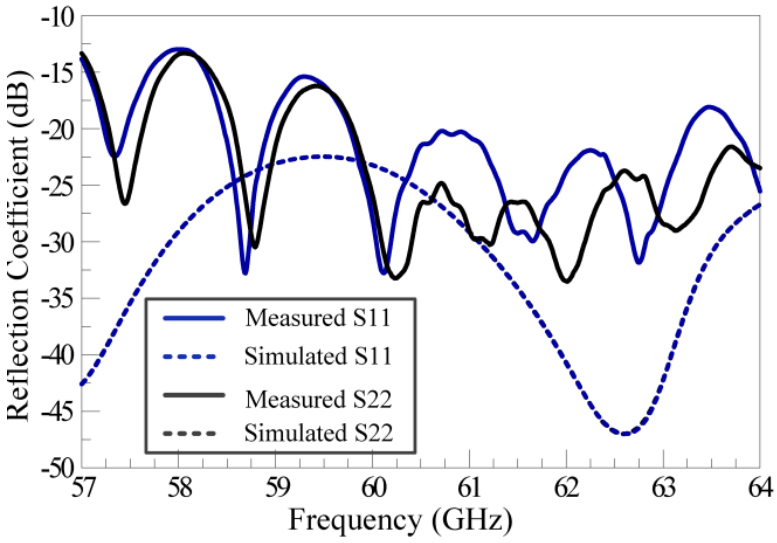

(a)

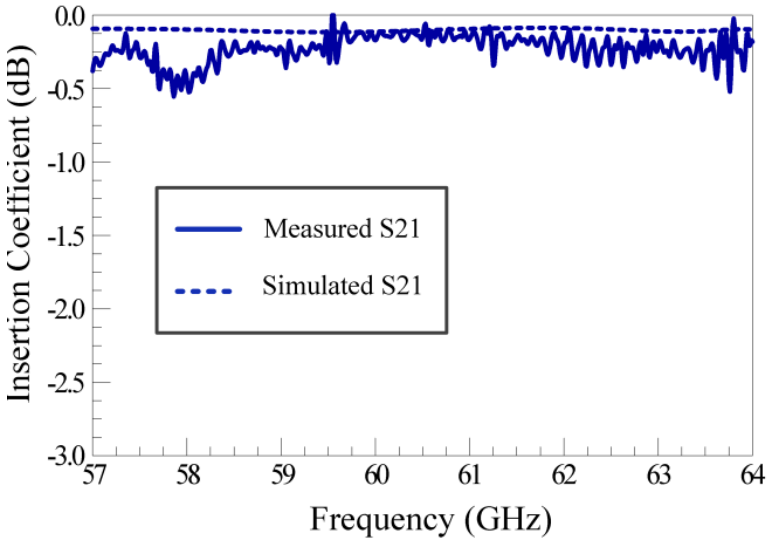

(b)

Figure 30 (a) Reflection coefficient of the printed and silver-plated trough waveguide structure (b) Insertion coefficient of the printed and plated trough waveguide structure

Electroless Metallization of Multiport Short Slot Hybrids

In this section the 3D printing and electroless silver deposition of WR-15 hybrid coupler operating over industrial, scientific and medical (ISM) radio band of 57-64 GHz is investigated. The hybrids terminated with E-bend and H-bend are analyzed. Electroless silver plating using pump-driven circulatory technique introduced in previous section is modified for multiport structures. Fluid flow in the multiport structures is investigated for successful metallization of the hybrids. The hybrid couplers discussed in this section is presented in Figure 31. Figure 32 shows the CAD model of the WR-15 short slot hybrid terminated with an out-of-plane E-bend and an in-plane H-bend. The hybrid section consists of one rectangular waveguide alongside another, and a section removed from their

common wall. This slot couples half of the incident power into each guide with a phase difference of 90° at the output.

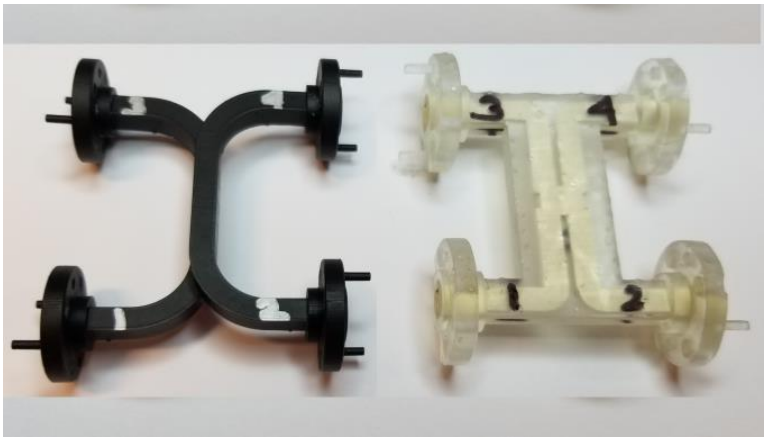

Figure 31 3D printed and metallized short slot hybrid couplers

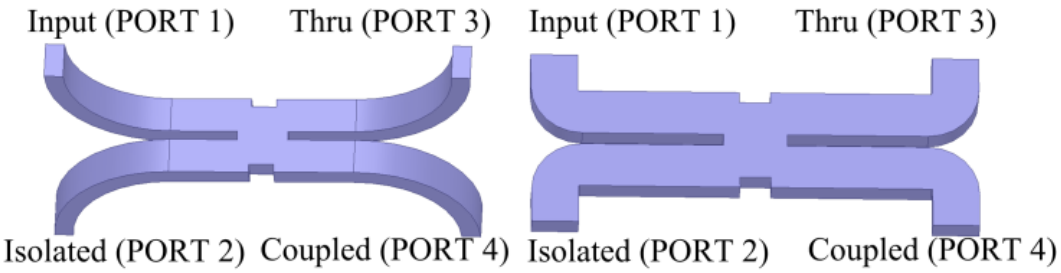

Figure 32 CAD model of short slot hybrid coupler terminated in E-bend waveguide (left) and H-bend (right)

Fabrication

The hybrids are printed using a stereolithographic commercial printer with acrylate-based resin at an angle of 45 degrees to the build plate. The printed structures are washed in 90% isopropyl alcohol for a total of 15 minutes. The wash cycle is subdivided into three stages of five minutes each. In the first and third stage the structure is washed in the isopropyl

alcohol tank provided by the commercial supplier. Though the waves created in the tank successfully washes loosely attached resin on the exposed surface of the structure, it is inefficient in cleaning the interior of the structure which is slightly complicated in design. Thus, in the second step the structure is cleaned using the pump driven circulatory system mentioned in previous section with ethyl alcohol used for metallization.

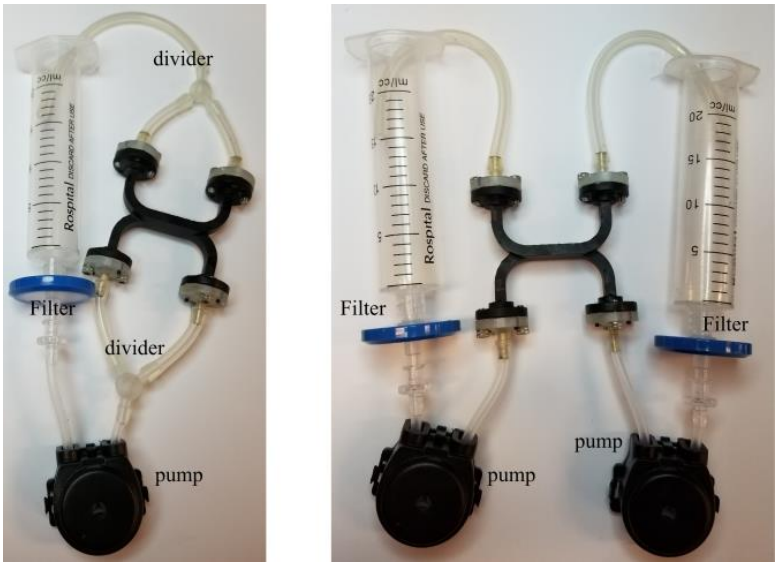

Figure 33 Modified pump-driven circulatory metallization system (a) Single pump and dual divider configuration (b) Dual pump configuration.

Figure 33 shows the two pressure-driven techniques examined for selective electroless metallization of the hybrids. Configuration 1 uses a single pump with two dividers connected at opposite ends of the hybrid. Configuration 2 uses two pumps to flow the plating solution into the hybrid. Each configuration utilizes a custom hose barb-to-waveguide flange connector that was engineered to allow the interconnection of the pressure-driven system with the electromagnetic components. The addition of the 0.22

mm membrane filter enhances quality of deposition by removing particulate and precipitate that does not adhere to the structure. 20 ml Tollens reagent to 4 ml dextrose solution is used in each run to metallize the structure.

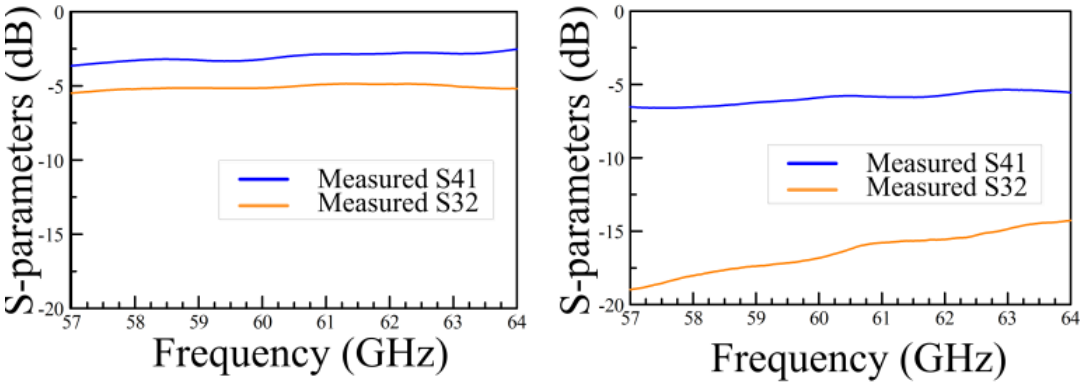

Figure 34 Measured magnitude of coupled PORTS after 4 runs with single pump dual divider (left) and dual pump configuration (right)

Plating solution flows into the structure through PORTS 1 and 3 while exits through PORTS 2 and 4. In every alternate run the inlet and outlet PORTS are swapped to ensure a uniform plating scenario. Hybrids metallized using the two configurations of pump set up are measured after 4 runs. Coupled PORT measurement results are shown in Figure 34. Asymmetric flow rate and inconsistent levelling of hybrid were the primary reasons for significantly different coupled PORT magnitude results with dual pump configuration. These experiments examining the balance in magnitude between coupled (90°) PORTS indicate the use of a single pump and divider system provide more uniform results over the dual pump system. The hybrid couplers terminated with E-bend and planar H-bend require 7 and 5 runs respectively to achieve the desired result of providing a uniform metallization of the structure.

Measurement

The hybrids are measured after TRL calibration of the network analyzer. The TRL calibration consists of commercial short, fabricated THRU and LINE segments. Measured magnitude results for hybrids with E-bend and H-bend launch are shown in fig. 5. Measured phase difference of output ports for the two structures is shown in fig. 6.

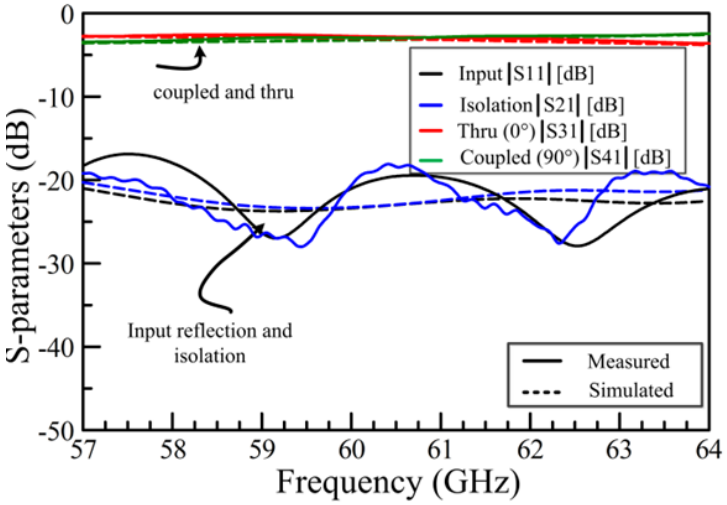

(a)

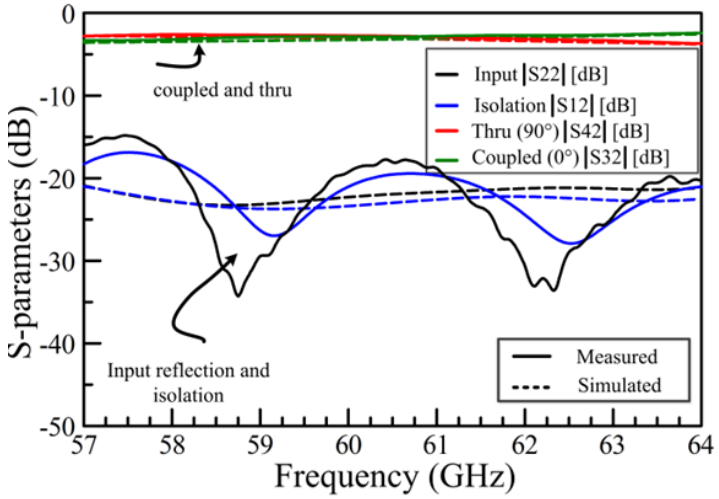

(b)

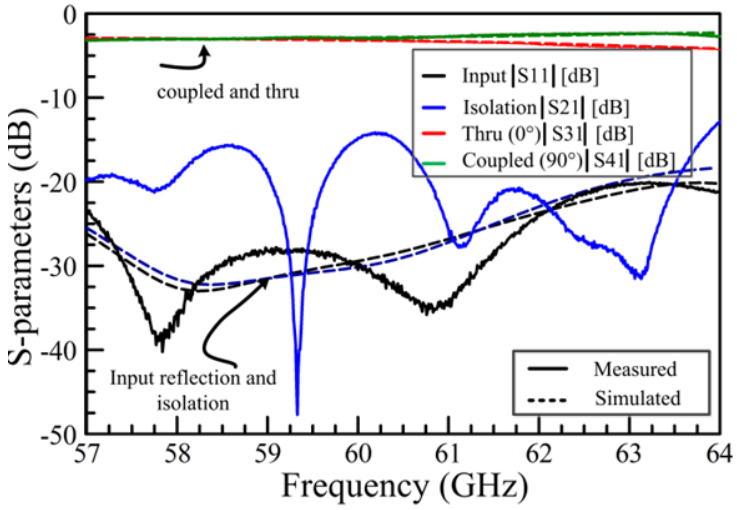

(c)

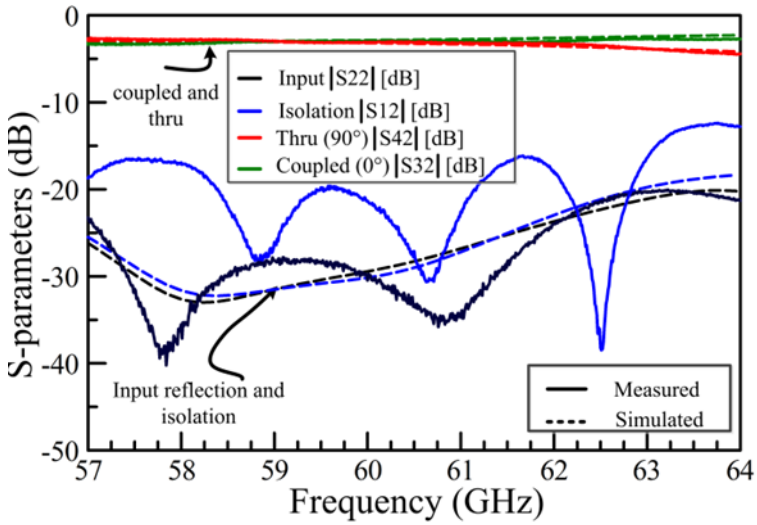

(d)

Figure 35 Measured s-parameters of hybrid coupler (a) Hybrid coupler with E-bend launch and PORT 1 as input (b) Hybrid coupler with E-bend launch and PORT 2 as input (c) Hybrid coupler with H-bend launch and PORT 1 as input (d) Hybrid coupler with H-bend launch and PORT 2 as input.

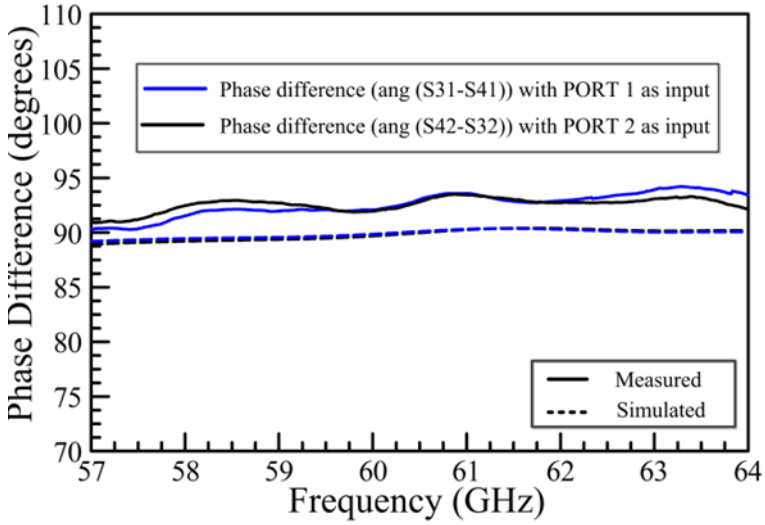

(a)

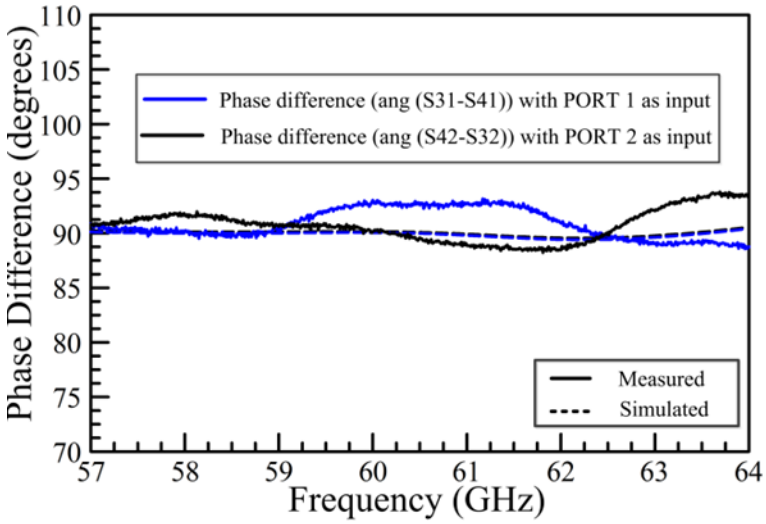

(b)

Figure 36 Measured phase difference at output PORTS. (a) Hybrid coupler with E-bend launch (b) Hybrid coupler with H-bend launch.

Modelling and Impact of 3D Print Inaccuracies on the Performance of Circular Waveguide Hybrid Coupler

This section aims to draw attention on the 3D printing inaccuracies and their effects on the performance of the structure. Figure 37 shows the CAD model and the fabricated model of the circular waveguide hybrid coupler. Figure 38 focusses on the intricate structures of the coupler. The group of ridges at the center of the structure and the vertical posts are prone to inaccurate prints. The aim is to focus on the deviation between measured and simulated results due to print inaccuracies. HFSS is used for carrying out simulations of the hybrid assuming perfectly conducting electric walls.

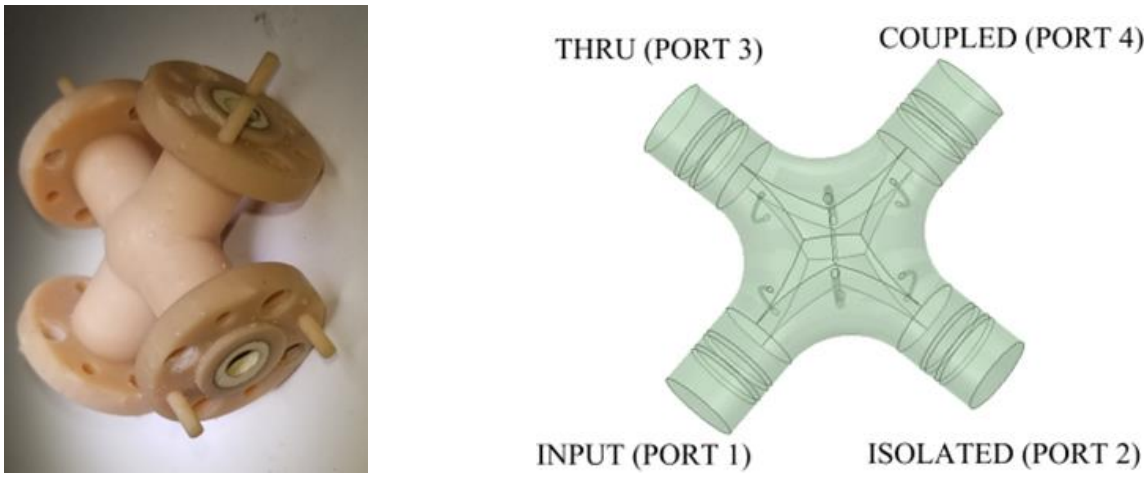

(a) (b)

Figure 37 Fabricated model (top) and CAD model (bottom) of coupler.
[2]

[2] Copyright © 2020, IEEE, Reprinted, with permission, from A. Bal, and G. H. Huff, "Modelling and Impact of 3D print Inaccuracies on performance of Circular Waveguide Hybrid Coupler" accepted for publication in International Applied Computational Electromagnetics Symposium

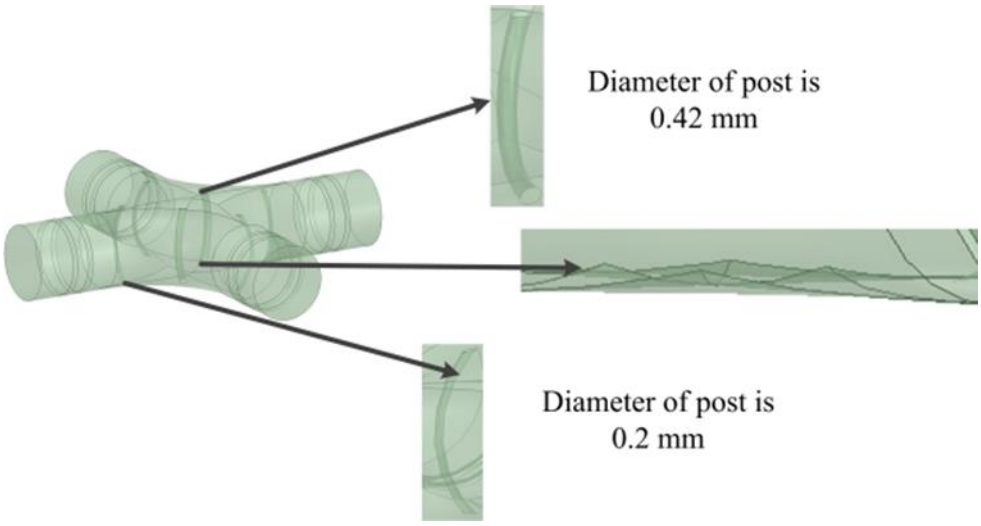

Figure 38 Delicate structures inside the circular waveguide hybrid.

Structural Analysis

The circular waveguide hybrid coupler consists of two different arrangements of inductive curvilinear post indicated as cluster of posts a and posts b. It also has the capacitive torus rings on each of its ports marked as ring c. The posts and rings are indicated in Figure 39. Each of these posts have specific role in the operation of this hybrid. The curvilinear post a alone offers equal division of power with phase difference of 90 degrees at the output ports offering equal power split, similar to the slot section in rectangular short slot hybrid. The equal power split at the output with curvilinear post a alone is shown in Figure 40. The post b and ring c offer matching across wider frequency bandwidth as shown in Figure 41. Increasing the number of rings beyond 2 do not offer improvement in performance.

[3]

[3] Copyright © 2020, IEEE, Reprinted, with permission, from A. Bal, and G. H. Huff, "Modelling and Impact of 3D print Inaccuracies on performance of Circular Waveguide Hybrid Coupler" accepted for publication in International Applied Computational Electromagnetics Symposium

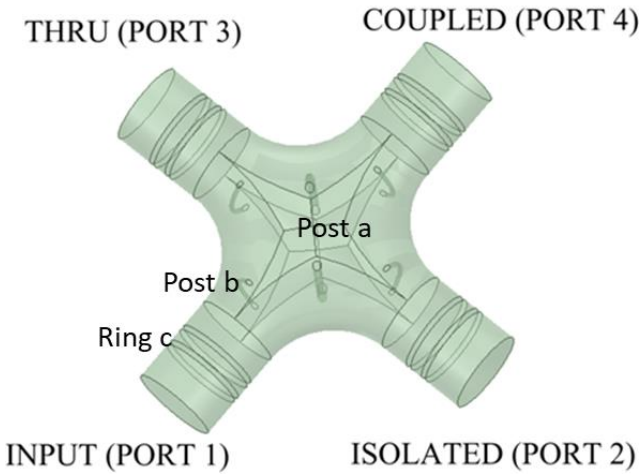

Figure 39 CAD model of circular waveguide hybrid coupler with inductive posts and capacitive ring.

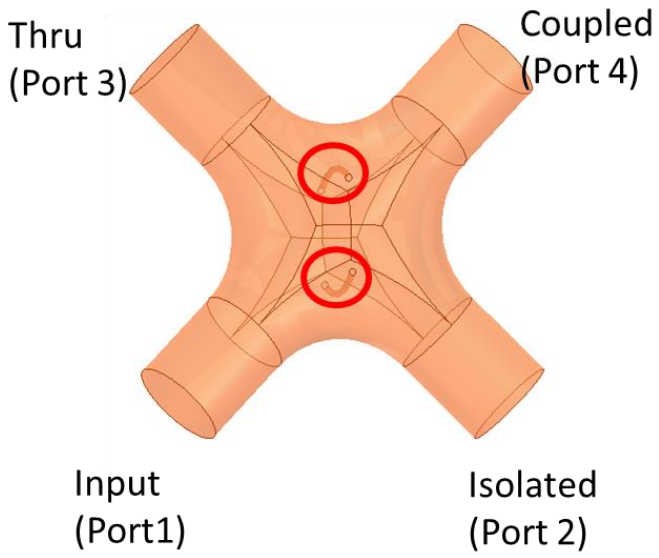

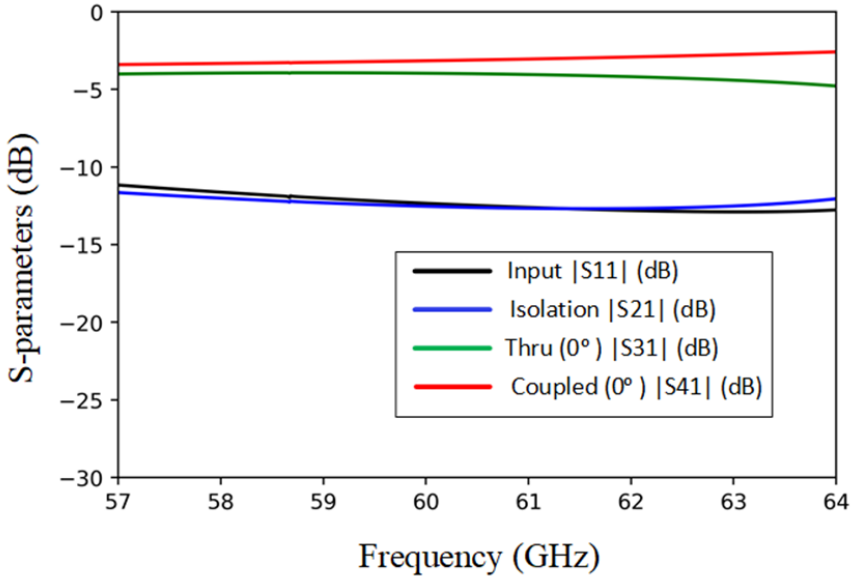

Figure 40 CAD model of circular waveguide hybrid coupler with inductive curvilinear post a only (top). Simulation results of the structure (bottom)

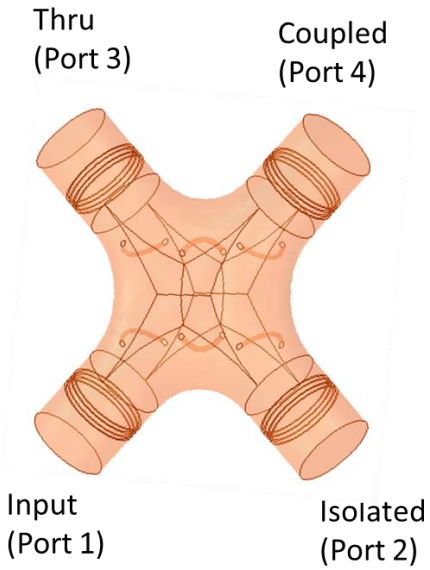

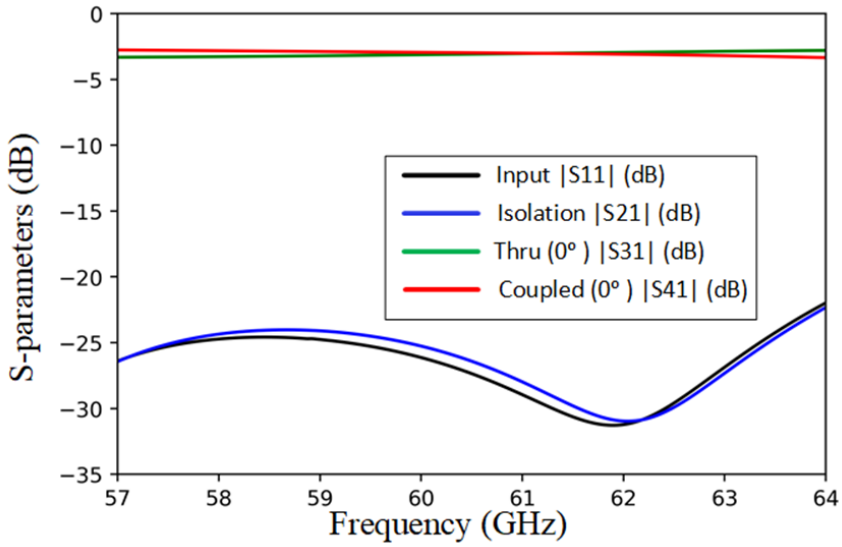

Figure 41 CAD model of circular waveguide hybrid coupler with inductive curvilinear post a, post b and ring c (top) and Simulation results of the structure (bottom).

3D Printing

The hybrid coupler is printed in different orientations along x- and y-axis on the build plate for accurate prints of the group of ridges. On printing the hybrid horizontally on the build plate, two among the four ridges supported by the internal post in the structure are printed accurately while, the other two unsupported ridges get deformed. In the next iteration the structure is printed at incremental angles from 10 to 30 degrees with respect to x- and y-axis. Figure 42 compares the printed ridges at the center of the structure for angle of print 10 and 30 degrees, respectively. Clearly the ridges are printed accurately at higher elevation. A comparison of the printed posts of diameter 0.2 mm and 0.42 mm for similar curvature are shown in Figure 43. Clearly, the 0.42 mm diameter post is printed closely to the designed dimensions than the 0.2 mm diameter post.

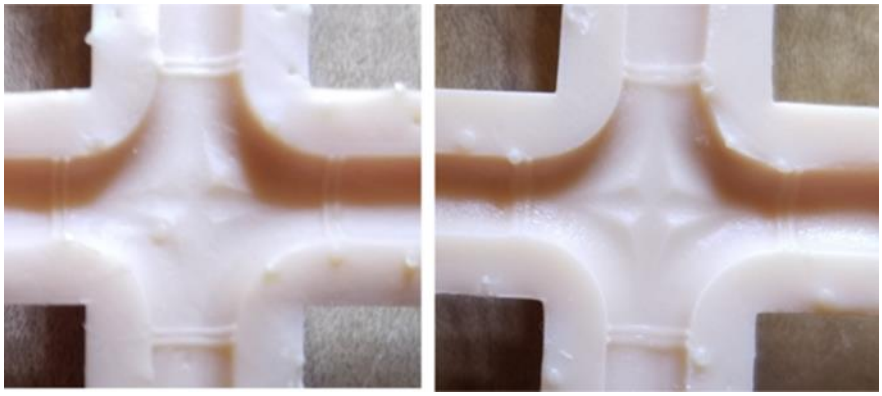

Figure 42 Printed structure at 10-degree (left) and 30-degree (right) elevation along x- and y-axis.

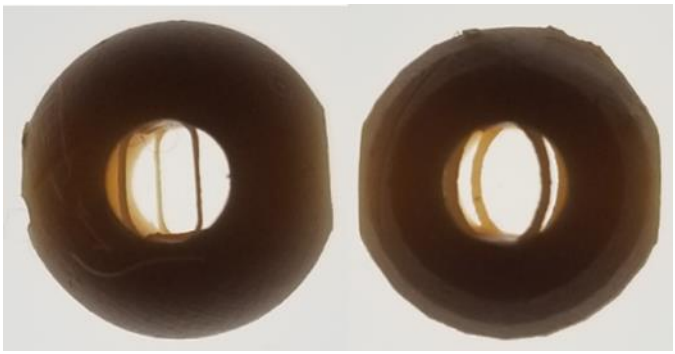

Figure 43 Printed post of diameter 0.2 mm (left) and 0.42 mm (right)

Measured results

This sub-section discusses the effects of printing inaccuracies on the performance of the structure. The measured structure has inductive post of diameter 0.2 mm, printed at an elevation of 10 degrees to x- and y-axis and efforts in mitigating these effects are also highlighted. The TRL calibration kit used for calibrating the network analyzer to shift the plane of reference till the end of the hybrid coupler, neglecting the effects of mode converters are shown in Figure 44. The parts marked as 1 and 2 are the mode converters which are used for THRU calibration. The part marked 4 is SHORT which is used as

REFLECT standard and the parts 1, 2 and 3 together form the LINE standard. The hybrid coupler is metal plated using electroless silver deposition technique discussed in the previous section for multiport structures. Figure 45 and Figure 46 shows the measured and simulated results. Figure 47 shows the error encountered in path length between diagonally opposite input and output due to fabrication inaccuracies. The structure when printed at lower elevation leads to inaccurate modelling of the intricate parts in the hybrid coupler which leads to errors in measurement both magnitude and phase. The source of these reflections seen in the measurement are due to the mode converters connecting the rectangular to circular waveguide which converts TE10 to TE11 mode. The detailed examination of these errors is discussed in the next chapter.

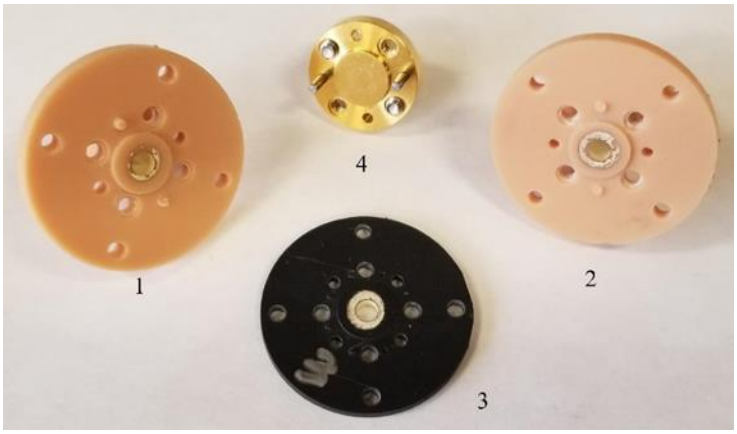

Figure 44 TRL calibration kit used for measuring the hybrid coupler

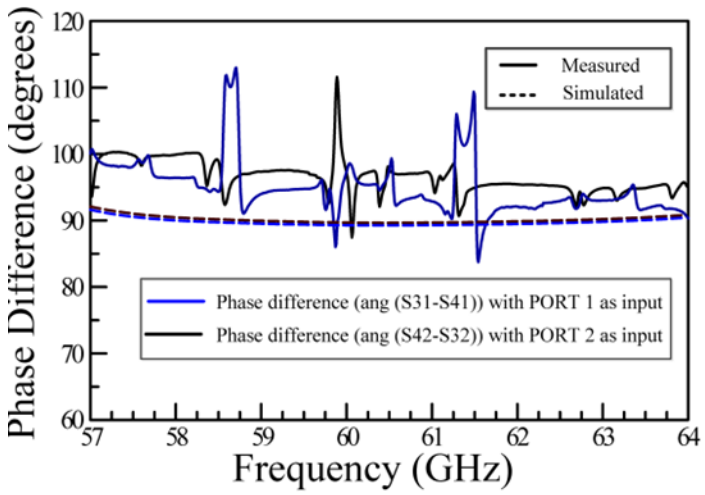

Figure 45 Measured and simulated phase difference between output ports.

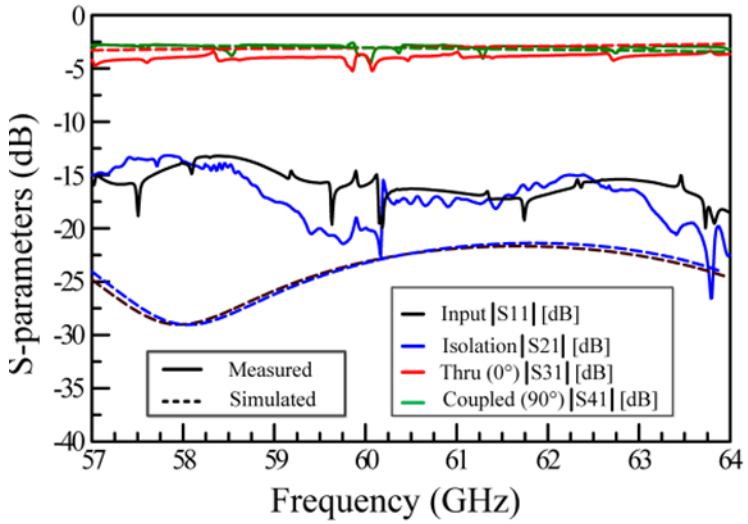

[4]

[4] Copyright © 2020, IEEE, Reprinted, with permission, from A. Bal, and G. H. Huff, "Modelling and Impact of 3D print Inaccuracies on performance of Circular Waveguide Hybrid Coupler" accepted for publication in International Applied Computational Electromagnetics Symposium

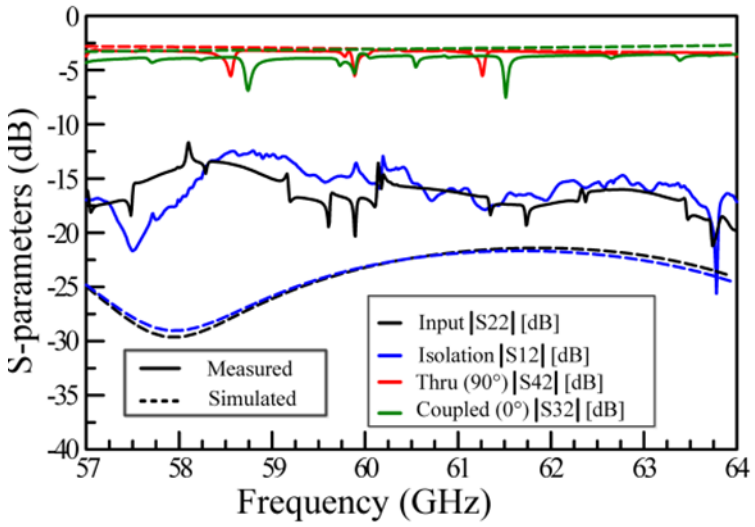

Figure 46 Measured and simulated magnitude distribution at output ports when PORT 1 (top) and PORT 2 (bottom) are excited.

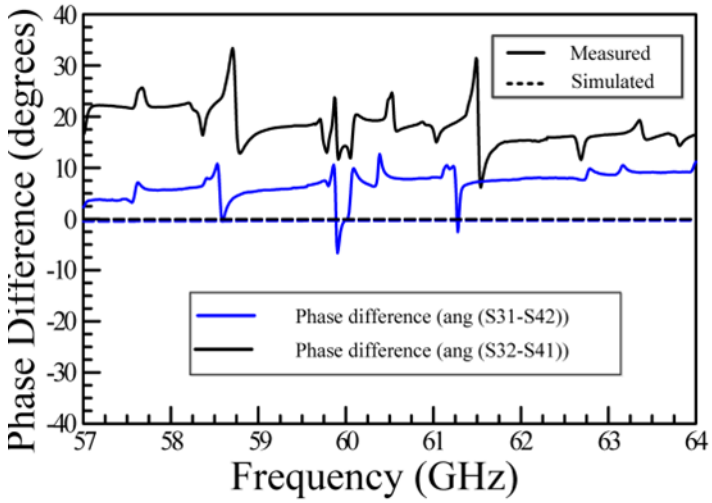

Figure 47 Difference in path length between input and output ports

The reduction in errors could be observed by fabricating the structure at an elevation of more than 30 degrees to both x- and y- axis and by fabricating integrated structure of hybrid coupler and mode converters as shown in Figure 48. The results obtained from the hybrid coupler shown in Figure 48 is shown in Figure 49 and Figure 50.

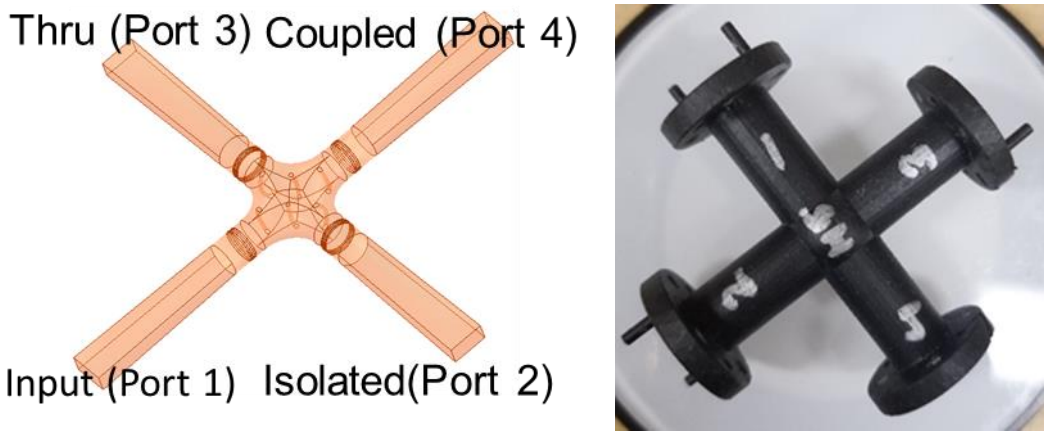

Figure 48 Hybrid coupler integrated with rectangular to circular mode converter

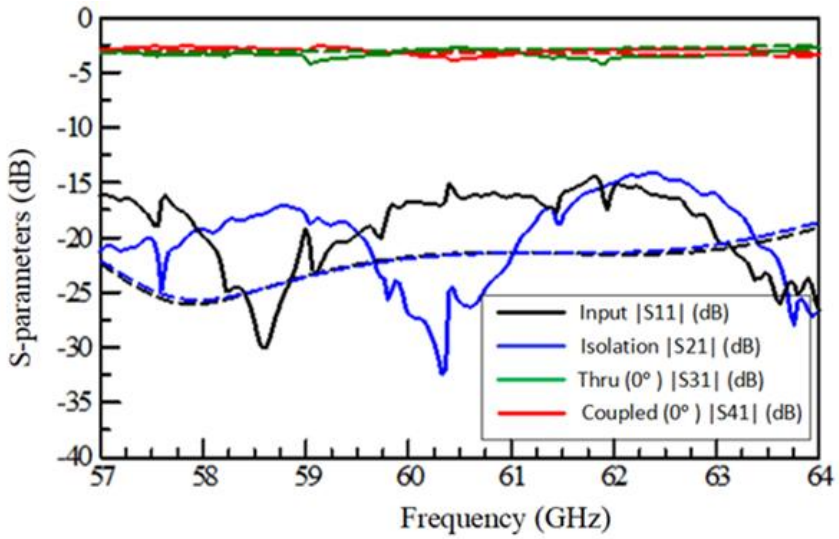

(a)

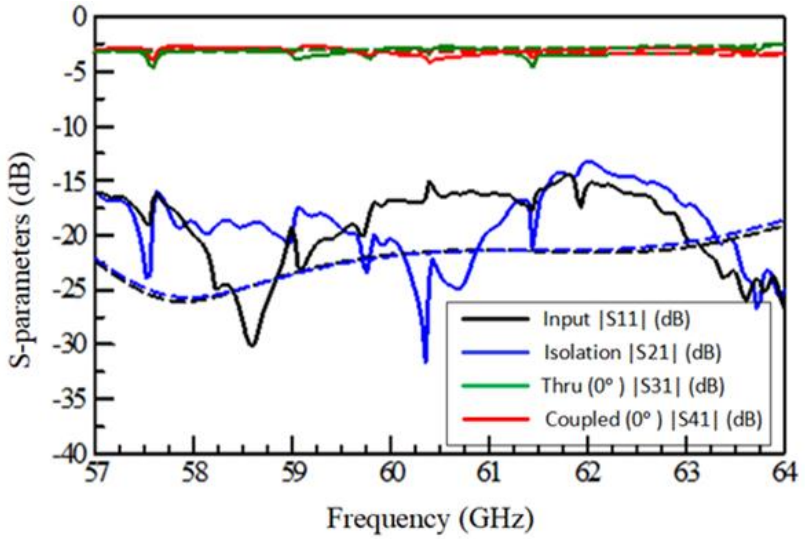

(b)

Figure 49 Measured and simulated magnitude distribution at output ports when PORT 1 (top) and PORT 2 (bottom) are excited for integrated structure of hybrid connected to mode converters.

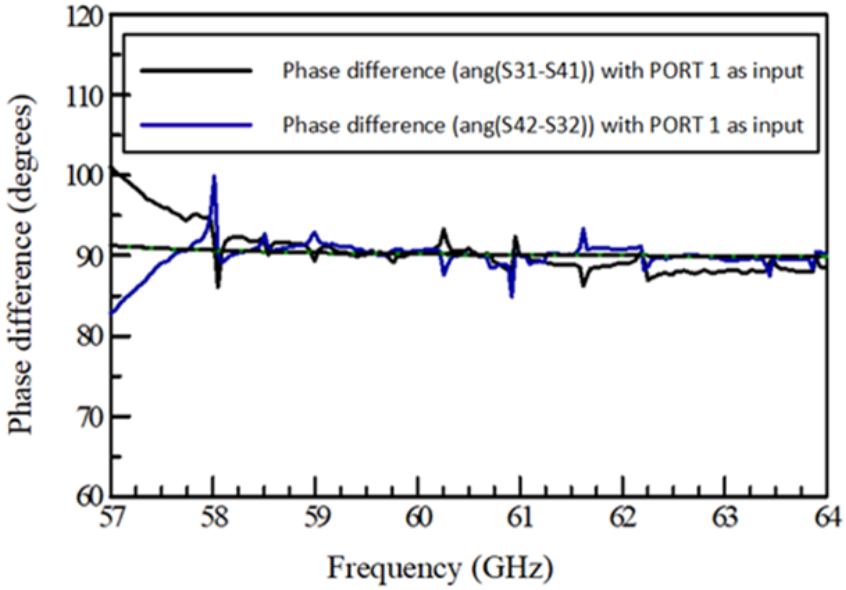

Figure 50 Measured and simulated phase difference between output ports for hybrid coupler connected with rectangular to circular mode converter.

Discussion

The metallization technique discussed in this chapter provides selective, effective, low-cost, low-waste alternative to existing process of metallization in literature like spray painting, electroplating, immersion coating etc. [71], [74]. This closed-loop circulatory metallization process offers efficient metal deposition on the interior surface of the complex electromagnetic device with 2 ports or multiple ports operating over V-band. This process could possibly be extended to metallize much complex structures operating over wide range of frequency bands. This study also demonstrates the design, fabrication and analysis of circular waveguide hybrid coupler, explored for the first time here to the best of the author's knowledge. This study also indicates the presence of precipitates which had not been reported earlier in literature and effective solution to eliminate those deposition by process of filtration to enhance the performance of the devices.

Key Contributions

- Demonstrated the ability to design, fabricate and metallize a complex electromagnetic component using closed-loop, selective circulatory system which is cost effective and generates less waste.
- Developed the proficiency to develop fluid flow through complex electromagnetic structures and establish understanding to metallize these structures.

CHAPTER IV

THREE-DIMENSIONAL DESIGN, ANALYSIS AND FABRICATION OF BEAM FORMING NETWORKS

Additive manufacturing (AM) is widely employed in designing high-frequency complex-geometry three-dimensional electromagnetic structures otherwise impossible to realize using conventional fabrication techniques. These structures pass through different stages like modelling, conversion to printable file followed by additive printing which introduces geometrical anomalies in the final printed model. These aberrations become pronounced in electromagnetic structures with complex geometry operating at higher frequencies as the overall dimension of the devices start scaling down with increasing frequency and starts grazing closer to the tolerance limit of the printer. In this chapter effects of approximations introduced in estimating the geometry of a modelled circular cross-sectional contorted waveguide operating over V-band (57-64 GHz) on the electromagnetic performance of the device is established. This chapter also discusses the design, analysis and fabrication of multi-section contorted beamforming network operating over V-band (57-64 GHz). Mechanical stability of the contorted structures during 3D printing is offered by resting the delicate bends on uniformly distributed cylindrical supports. The selective fluidic flow through the complex structure for obtaining uniform metallization is also discussed. The geometrical defects introduced during fabrication flow of contorted structures and problems encountered in the metallization process are documented in the discussion section along with possible solutions to alleviate these issues.

Background

Application of AM techniques in the design of complex geometry electromagnetic (EM) and radio frequency (RF) devices and components like antennas, waveguides, passive electronics, filters, electromagnetically engineered surfaces etc. are gaining immense popularity over planar structures fabricated using conventional fabrication techniques. 3D printing techniques enable construction of custom geometries by reducing number of processing steps, and resources thus simplifying the whole fabrication process compared to conventional methods [78]. Electromagnetic devices and components developed by printing metallic ink on planar or curved surfaces like shape-conformal antennas printed on volumetric curved surfaces [79], [80], frequency selective surface [81], [82] , passive electronics [83], [84] , RFID sensors [85]–[87] promise efficient fabrication along with desired performance. 3D printing using metallic, non-metallic or a combination of the metallic and non-metallic substrates are highly compelling for fabrication of RF and EM devices and components. The AM techniques employing non-metallic substances like acrylonitrile butadiene styrene (ABS) or other forms of plastic include fused filament fabrication (FFF) used for 3D printing of diplexer, filter, coupler, and reflector antenna [71], [88], [89], fused deposition modelling (FDM) used for printing corrugated horn antenna, RFID antenna [90], [91], and stereolithography for printing antennas and waveguides [92] etc... 3D printing techniques like selective laser melting (SLM) uses metallic powder for printing waveguides [93] while direct digital manufacturing (DDM)

technique employs a combination of metallic and dielectric substrates for construction of multilayer antennas [94] .

The process of 3D printing is composed of multiple steps like CAD modelling of the desired structure, conversion of CAD model to printable stereolithographic (.STL) format, interpretation of printable file by 3D printing software based on printer resolution (in X, Y and Z- direction), orientation of the printable structure etc. and postprocessing which includes one or more of the following steps like careful removal of supports, alcohol wash or curing. The final fabricated model is prone to geometrical errors due to the approximations assumed in each of the above-mentioned steps which in turn affects its overall electromagnetic performance. The deviations in geometrical features between CAD model and 3D printed structures impact electromagnetic performance severely for complex structures and/or devices operated at higher frequencies. Research focused on identifying and mitigating geometrical defects or deviations have primarily concentrated on generic structures. Efforts towards reducing geometrical errors between CAD model are .STL faceted structures are discussed in [95]. Analytical deviation models of regular geometrical shapes derived and calibrated based on measured data are explored in [96]. Compensation for geometrical deviations in polygons and cylindrical 3D models using analytical and statistical tools are explored in [97]–[99]. Similar efforts in handling shape deviation in FDM and employing FEM to model shape shrinkage are enumerated in [100], [101]. Effect of structure orientation on build platform affecting surface quality and part accuracy are discussed in [102], [103].

Air-filled waveguides and antennas operating at higher frequencies are favored for their higher power handling capabilities and lower losses. As the frequency increases the size of the EM devices shrink in size and starts grazing close to the minimum feature or layer resolution supported by 3D printers. Performance of EM devices susceptible to fabrication errors are seen in the measurement results [15] . Some of these geometrical errors introduced during fabrication affect the EM performance of the device significantly especially at higher frequencies. As the cross-section of a waveguide is changed from rectangular to circular the dominant mode of propagation changes from TE10 to TE11 which is also indicative of the change in electric field distribution in the structure. This change in cross-section of the waveguide leads to increased sensitivity of the electric field to geometrical defects. This chapter aims to investigate the electromagnetic characteristics of a contorted circular waveguide (CWG), 3D printed using stereolithographic techniques and metallized with silver using closed-loop circulatory system operating. Focus is drawn towards the anomalies seen in measurement and the optimum orientation for obtaining satisfactory results are also highlighted. The preliminary analysis is established by investigating the measured and simulated results of a single section CWG connected to rectangular-to-circular waveguide (R2C-WG) transition at either ends. The results from the analysis of single section CWG are extended for analysis of electromagnetic characteristics in the contorted CWG. The chapter also investigates the design, analysis, and metallization process of contorted 4X4 Butler matrix developed vertically to represent a compact structure with stacked hybrids connected through appropriately phased waveguide bends. Butler matrix is a class of beam forming network with N inputs and N

outputs thus, a NXN Butler matrix provides discrete Fourier transform of signals which enable beam scanning. Butler matrix is physically realized through a network of hybrids, phase-shifters and crossover networks. The inputs or outputs, hybrid couplers and progressive phase-shifts at the output can be mathematically expressed as given in equations 4-7. The diagrammatic representation of a 4X4 Butler matrix is given in Figure 51. Crossovers are used for swapping signals between diagonal ports without interference and they consume significant area on a printed circuit board. Intelligent structures avoiding crossovers are simple and easy to implement without encountering significant power loss. The vertically stacked completely 3D Butler matrix employed in this chapter leverages the concept of compact beam forming network without requiring a crossover.

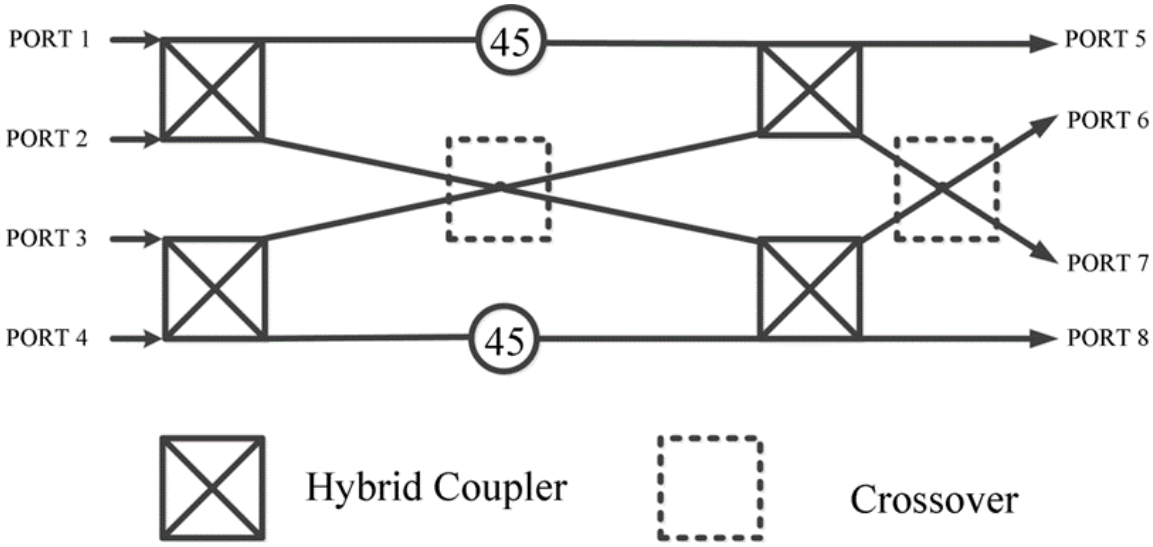

Figure 51 Diagrammatic representation of a 4X4 Butler matrix with hybrids, phase-shifters ad crossovers.

$N = 2^m$, where m is an integer ---------- (4)

Number of hybrids: $\frac{Nlog_2^N}{2}$ ---------- (5)

Number of phase shifters: $\frac{N\,(log_2^N - 1)}{2}$ ----------(6)

Progressive phase-shift between output ports: $\beta = \pm\frac{2p-1}{N}X180\ \ where\ p = 1, 2, \ldots N/2$ ----------(7)

CAD Modelling of Waveguide Structures

This section discusses the CAD modelling of single-section CWG, contorted CWG and 4X4 contorted Butler matrix operating over a frequency of ISM 57-64 GHz. The modelling of the structures from single section circular waveguide to Butler matrix are discussed in detail for establishing understanding between measured and simulated results. The curves and bends in contorted structures are explained in detail and they are intelligently designed to preserve the polarization and rotational symmetry at input and output ports. The architecture of the Butler matrix enables development and analysis of compact beam forming networks beyond 4 inputs and outputs.

Single-section Circular Waveguide

Figure 52 shows the CAD model of a single section CWG with R2C-WG transition connected at either ends of CWG. The transition is used for converting fundamental TE10 mode in rectangular waveguide to the fundamental TE11 mode in CWG. To study the electromagnetic characteristics of a single section CWG contributed by geometrical

inconsistencies, establishing a relation between measured and simulated data is extremely important. The following steps employed in the design of the single section CWG establishes closest approximation between simulated and measured results. Detailed explanation of the steps for modelling the structure in electromagnetic simulator is shown in Figure 53. Step1: circular section in the yz-plane is created with a diameter of 3.581 mm and a rectangular section along yz-plane with a spacing of 17.3 mm away from the circular section along x-axis with a dimension of 3.76 X 1.88 mm is created. These two sections (circular and rectangular) are connected to form the R2C-WG transitions. Step2: The transition section is duplicated 180 degrees around the center along the z-axis. Step4: CWG is created from the circular faces of the transitions. The total length of the single section CWG is 85.4 mm (approximately 17 times the free space wavelength at 60 GHz).

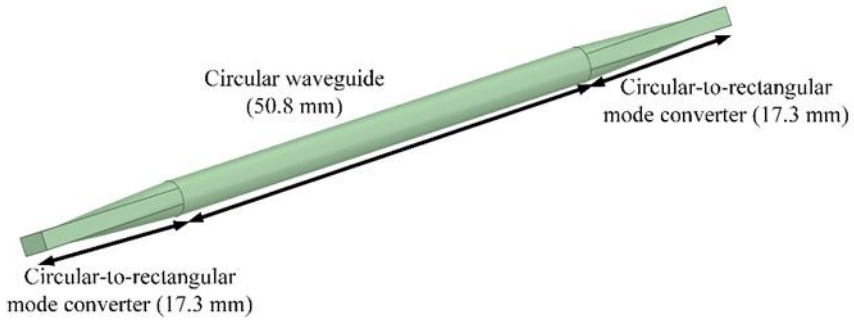

Figure 52 CAD model of single section CWG with R2C-WG mode converters connected at both ends.

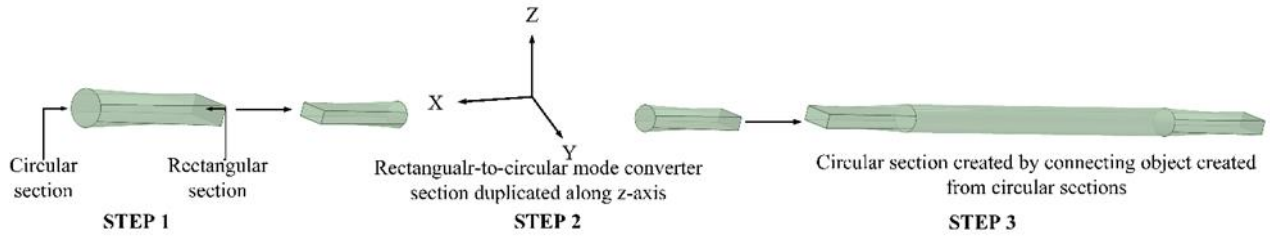

Figure 53 Step-by-step modelling of single section CWG connected to R2C-WG mode converters on both ends.

Multi-section Contorted Circular Waveguide

Figure 54 shows the CAD model of the contorted multi-section CWG. This CWG waveguide consists of 10 smaller circular sections with horizontal and vertical bends, connected to the R2C-WG transitions at both ends. These waveguide bends are created by circular 3D expansion of lines curved with the designated angles. The vertical dimension of the contorted CWG is 51.5 mm (approximately 10 times the wavelength at 60 GHz) and horizontal dimension is 69.8 mm (approximately 14 times the wavelength at 60 GHz). The contorted waveguide images from different cut planes are shown in Figure 54. The bends in the curves are optimized to provide an overall reflection co-efficient below -15 dB in ideal scenario with frequency of operation over 57-64 GHz.

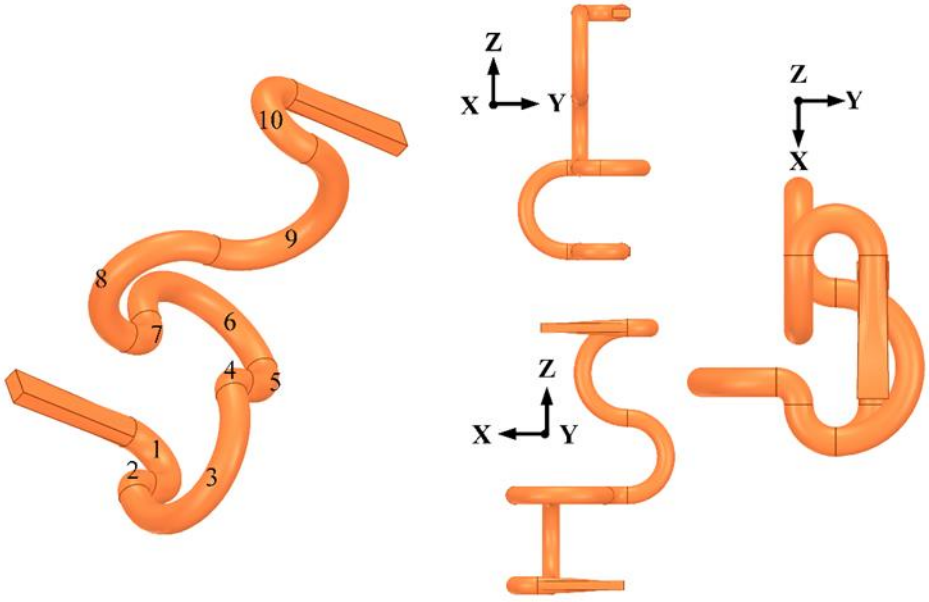

Figure 54 CAD modelling of contorted CWG with R2C-WG mode converters connected at both ends.

Contorted Butler Matrix

The CAD model of 4X4 contorted Butler matrix is shown in Figure 55. The hybrid couplers discussed in the previous chapter are stacked vertically with a uniform spacing of approximately 25 mm between them. The required phase modification of the Butler matrix as discussed in the background section is achieved by tuning the phase in coarse and fine manner. The coarse tuning of phase is achieved by varying the horizontal spacing and vertical spacing of the hybrids and phase bends respectively while fine tuning is achieved by modifying the dimension (width and depth) of the rectangular capacitive rings on one of the phase bends. The coarse-tuning aids in rapid change of phase between the waveguide bends while the fine-tuning mechanism is employed for closer approximation of phase reducing the margin of error. The inputs and outputs aligned on the same vertical plane for ease of connection with external connectors. The two different phase bends connecting the hybrids internally are shown in Figure 55 along with the complete 4X4 Butler matrix. The input ports and shown in red and the outputs in blue. The input ports are positioned closer together for ease of connection with antenna elements.

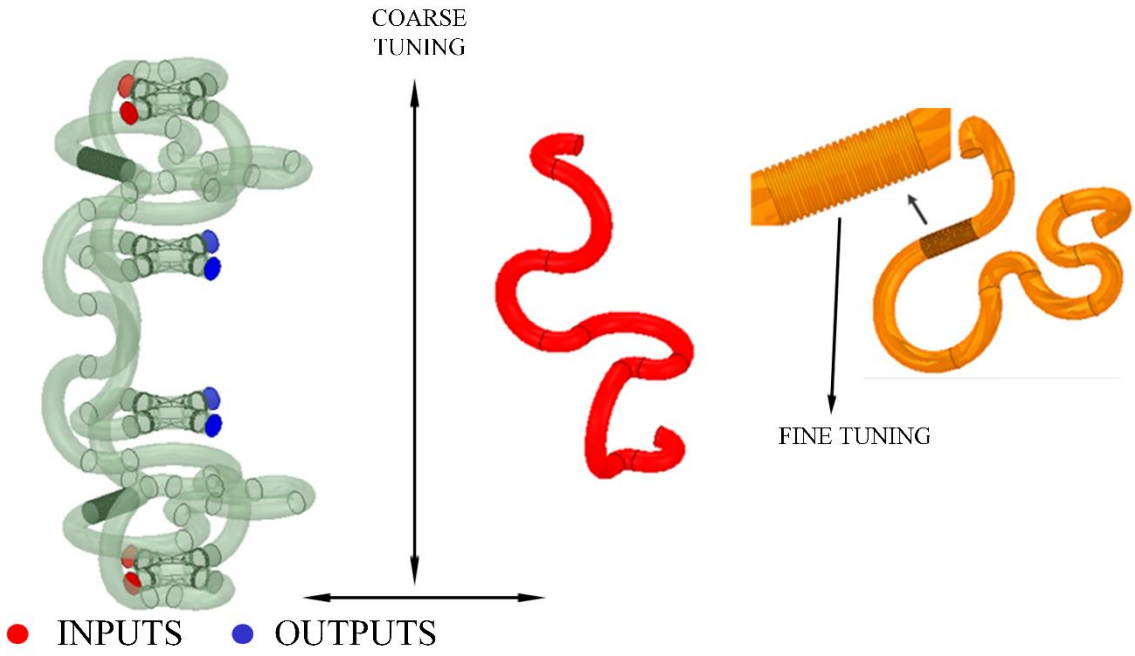

Figure 55 CAD model of 4X4 Butler matrix comprising of hybrid couplers and phase bends.

Fabrication and Metallization

This section describes the process of 3D printing and metallization of the three structures- single section CWG, contorted waveguide CWG and 4X4 Butler matrix. Commercial stereolithographic printer with printing resolution along z-axis of 25 microns and x, y-axis in the range of 100-150 microns is used for 3D printing both the structures described above. Three different resins namely black, clear, and model have been used interchangeably for the whole experimental expedition and similar results have been obtained across all three resins. The CAD models of printable files shown in the next section has been used to print the structures. The CAD models are converted to .STL file which discretizes the complete geometry into smaller sections. This .STL file is

reconstructed as a whole by the print software and interpreted for fabrication based on orientation and tolerance limits of the printer.

Single-section and Multi-section Contorted Circular Waveguide

The thickness of outer casing in single section CWG is approximately 3 mm in thickness. While the thickness of the outer casing in reduced to 1 mm for most parts of the contorted CWG except near the flanges where the thickness is maintained at 3mm. The thinner casing could potentially lead to failure in prints, compromising with the mechanical stability of the structure especially around the curves. Cylindrical pillars distributed along the length of contorted CWG supports the delicate curves in the structure and enhances the mechanical endurance of the overall structure. These modifications in the contorted CWG offers faster print and less resin usage compared to a volumetric casing which could potentially offer similar mechanical stability to the structure.

The single-section CWG is printed at an arbitrary orientation (horizontal, vertical or angled with respect to base plate) with the build plate as significant increment in time is not seen across different orientations. After successful print the structure is washed in commercial wash tank filled with isopropyl alcohol of concentration 95 % followed by 1.5-2 hours of air drying and curing at 60^0 C for 60 min. The single section CWG is metallized using the procedure detailed in chapter III which uses a single pump circulatory closed-loop system. 20 ml of Tollens reagent is mixed with 4 ml of dextrose (reducing agent) for each run and five such runs are required for metallizing the structure to obtain

satisfactory results. Total amount of silver required for metallizing the single section CWG is 1gram by weight.

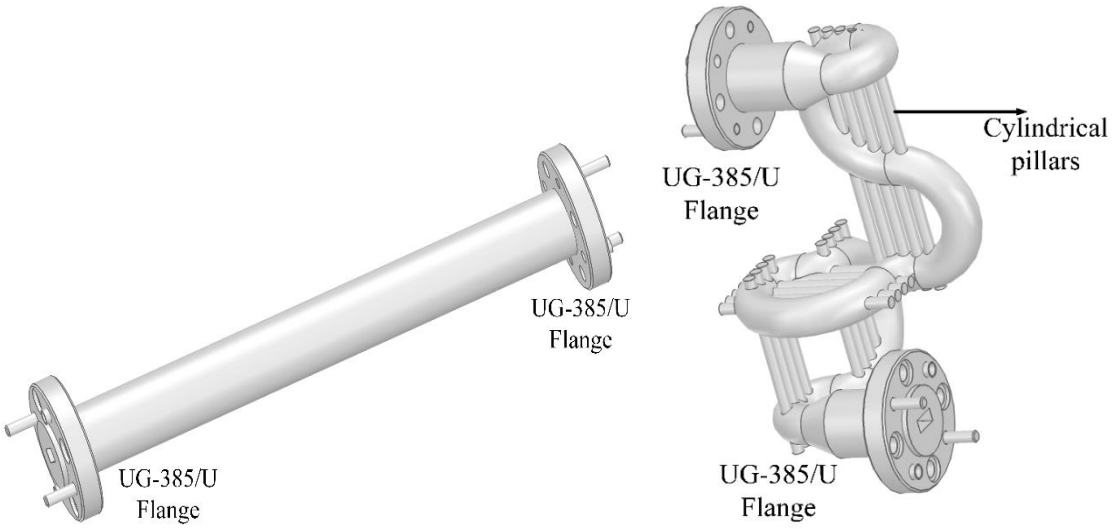

(a) (b)

Figure 56 CAD model of CWG terminated on both ends by R2C-WG mode converters and flanges connected at either ends for ease of connection with commercial measurement system (a) Printable single section CWG (b) Printable contorted CWG.

The contorted CWG is printed horizontally as it reduces time to print approximately by 5-7 hours over vertical or angled with base plate and offers closest to ideal results. This structure is washed with isopropyl alcohol (95% concentration) for 5 mins in commercial tank to remove resin from the outer surface of the structure and 10 mins using the modified dual-pump circulatory closed loop system shown in Figure 57. It is dried with heavy flow of air to remove excess alcohol followed by air drying for 6-8 hours and curing at 60^0 C

for 60 min. The dual-pump circulatory system is used for thorough cleaning of resin from the inside geometry to obtain uniform metal deposition.

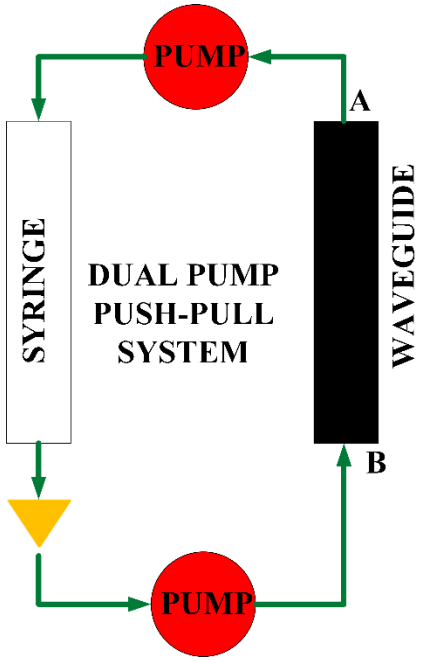

Figure 57 Dual pump push-pull system for metallizing geometrically complex structures like contorted CWG.

The dual-pump closed loop circulatory system consists of two pumps which rotates in the same direction to enhance the speed of fluid flow through the longer contorted waveguide structure. Slower fluid speed through the system reduces the uniformity of deposited metal at extreme ends eventually affecting the overall performance. 20 ml Tollens reagent mixed with 4 ml dextrose reducing solution is transported through the structure for each run. Desired results are obtained after 15 such runs (3 grams of silver by wt. is deposited) and the contorted waveguide is rotated between points A and B after each run to achieve uniform metal deposition. The number of runs required for

metallizing waveguide is decided by the best results obtained. Metallizing a structure beyond certain number of runs do not offer significant improvement in measured results and leads to gradual degradation of results at higher frequencies due to increasing surface roughness.

4X4 Contorted Butler Matrix

The CAD model of 3D printed Butler matrix is shown in Figure 58. The outer casing is 2.5 mm is width for most of the structure except at the sharper curves where it is maintained at a thickness of 1 mm as increasing the casing thickness around sharp curves leads to design errors. The mechanical stability of the structure is maintained by the cylindrical supports shown and the flanges have also been modified to withstand the effects of multiple connection and disconnection during the whole metallization and measurement expedition. The circular waveguide Butler matrix is terminated with R2C-WG at all input and output ports enabling connection to rectangular flanges. The 3D printed 4X4 Butler matrix is washed in isopropyl alcohol selectively connecting only 2 sets of ports at a time using the modified dual pump push-pull system shown in Figure 57. The chosen set of port combinations are: IN 1&2, IN 3&4, OUT 1&3 and OUT 2&4. If one set is chosen as inlet the outlet is swapped between the other 3 combinations with alcohol wash performed for 1.5 minutes with each combination. All the combinations are chosen as inlets while the outlet swapped across the other three combinations. When the set of inlet and outlet are connected the other ports are terminated with a flat piece of

elastic resin blocking the outlet to minimize fluid flow in that particular direction. The entire structure is air-dried for around 24 hours and then cured in commercial machine.

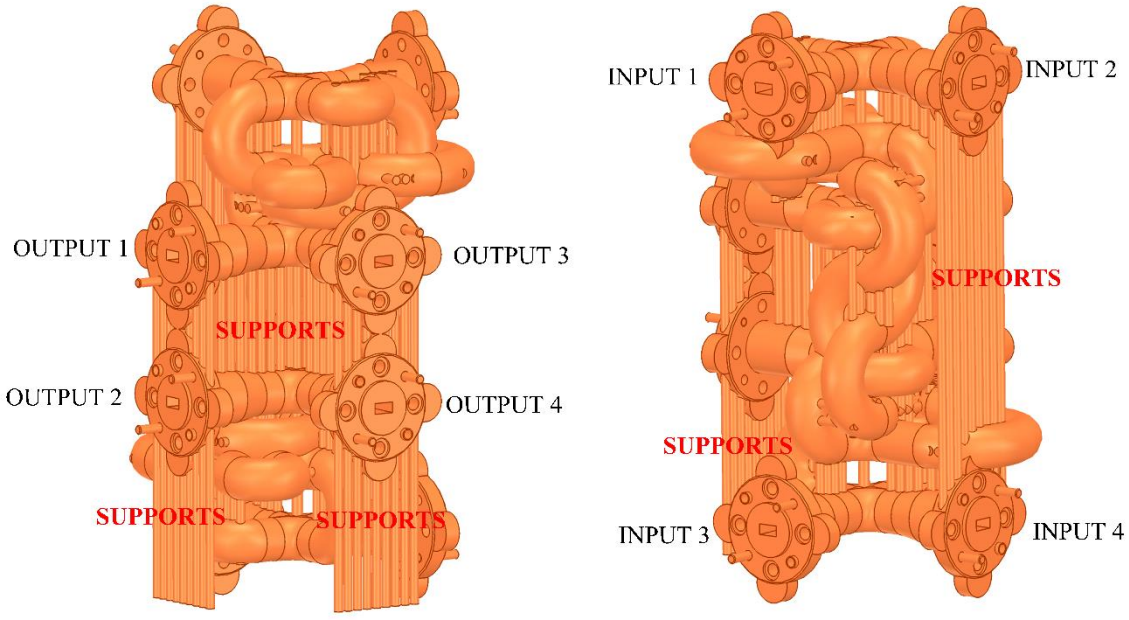

Figure 58 CAD model of fabricable 4X4 Butler matrix with modified flanges and supports to ensure mechanical stability of the structure during 3D print.

Measurement and Analysis

This section presents the detailed analysis of measured and simulated results of single section CWG, contorted CWG and 4X4 Butler matrix. The electromagnetic simulation software approximates the surface geometry of single section CWG by multiple smaller geometries based on chosen meshing and solves the electromagnetic fields on the entire structure by computing boundary conditions on smaller geometries. Similarly, the circular cross section is approximated by N-sided polygon and the entire geometry of CWG by smaller geometries which is converted to. STL format followed by reconstruction of the printable file (. STL format) in 3D printer software. The effects of these geometrical

approximations on the overall electromagnetic performance of the waveguide structures are explored here in details through measurement and simulation.

Single-section and Multi-section Contorted Circular Waveguide

The diameter of the circular cross-section of CWG is chosen as 3.5814 mm to excite fundamental mode TE11 over the frequency range of interest (57-64 GHz). The simulation results for a single section CWG with no transitions connected offer insertion coefficient close to 0 dB and reflection coefficient below -60 dB over the frequency range without any reflections. But the simulation results with default surface meshing for single section CWG connected to R2C-WG transition on either end show insertion co-efficient of 0 dB and reflection co-efficient below -40 dB with periodic reflections throughout the frequency range of interest for a 2-inch long circular waveguide. Figure 59 shows the simulation results of the single section circular waveguide with the R2C-WG transition connected in case 1 and without any mode converters connected in case 2. In both the structures only, the cylindrical waveguide section is measured. In case 1 this is achieved by de-embedding to remove the effects of R2C-WG transitions. These simulations are carried out with the default surface meshing in the software and is kept unchanged across the two cases. However, increasing the meshing to enable finer approximation of the surface of CWG connected to R2C-WG transitions removes the periodic reflections from the results offering the desired results across the frequency range without significant reflections.

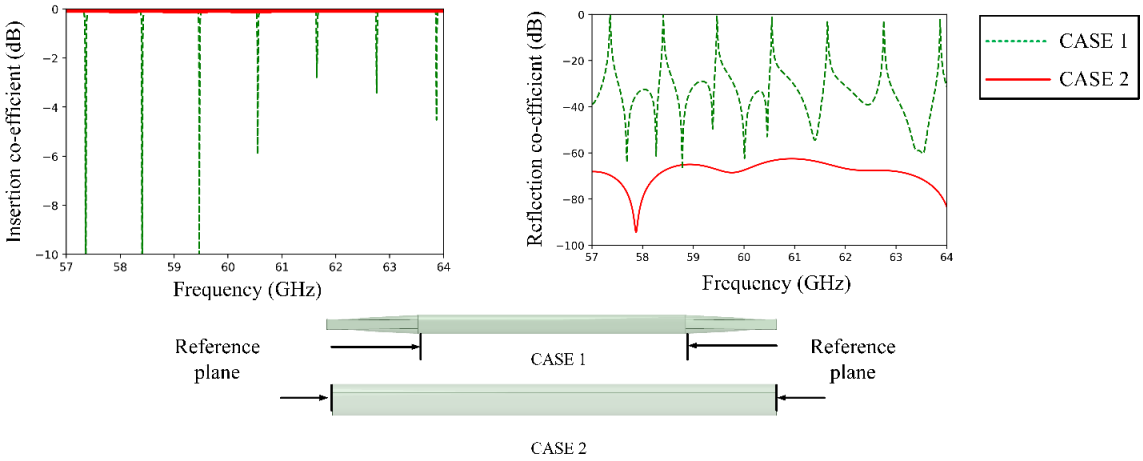

Figure 59 Simulated results in single section circular waveguide with R2C-WG mode converter connected (case 1) and circular waveguide with no R2C-WG mode converter connected (case 2).

Figure 60 compares the results from meshing differences and the observed results in the same single section CWG connected to R2C-WG transitions on either ends. This analysis obtained from simulation results indicate that a coarse meshing of the circular cross-section leads to periodic reflections contributed by undesired modes propagating in the waveguide at the frequency range of interest. Exact conversion of TE10 to TE11 mode occurs in the R2C-WG transition when the surfaces are finely approximated by dense meshing. The periodic reflection across the frequency range is not observed in a circular waveguide without R2C-WG transition even with coarse meshing (Figure 59) as the conversion of from TE10 to TE11 is not encountered in this scenario.

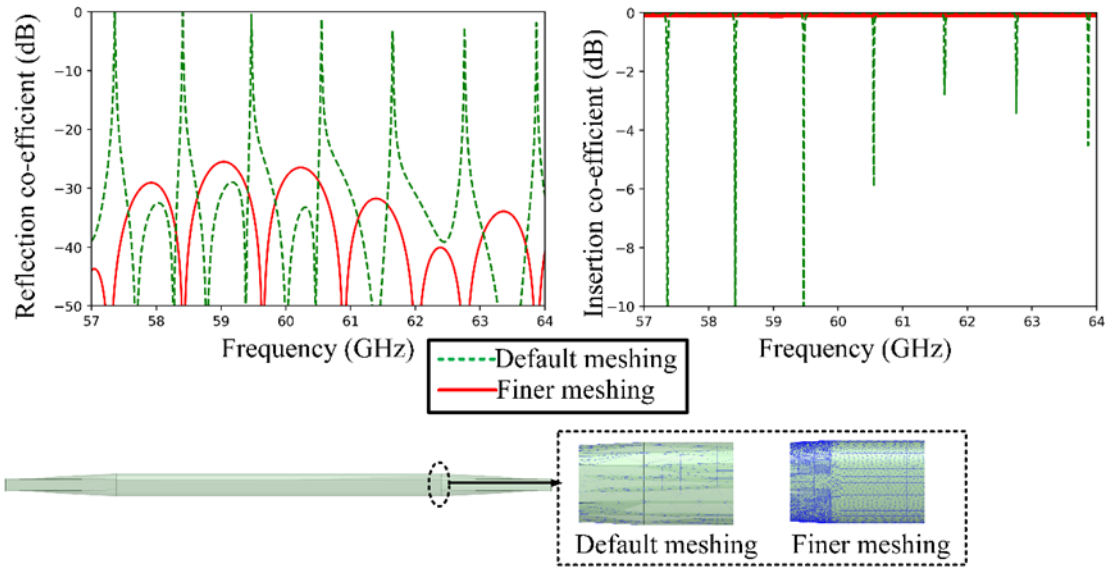

Figure 60 Comparison of simulated results in a single section CWG connected to R2C-WG transition with default and finer meshing.

The Figure 61 (a) shows the close relationship between the measured and simulated results of the structure with periodic repetition of reflections occurring at precise frequency locations. The measurement results are obtained by calibrating the network analyzer using Transmission Reflection and Load (TRL) calibration kit shown in Figure 62 (b) ensuring that the effects of R2C-WG and external connectors are ignored, shifting the plane of reference beyond R2C-WG. The close relationship between measured and simulated results are obtained for the CWG with the simulated structure designed using the procedure described in Figure 53.

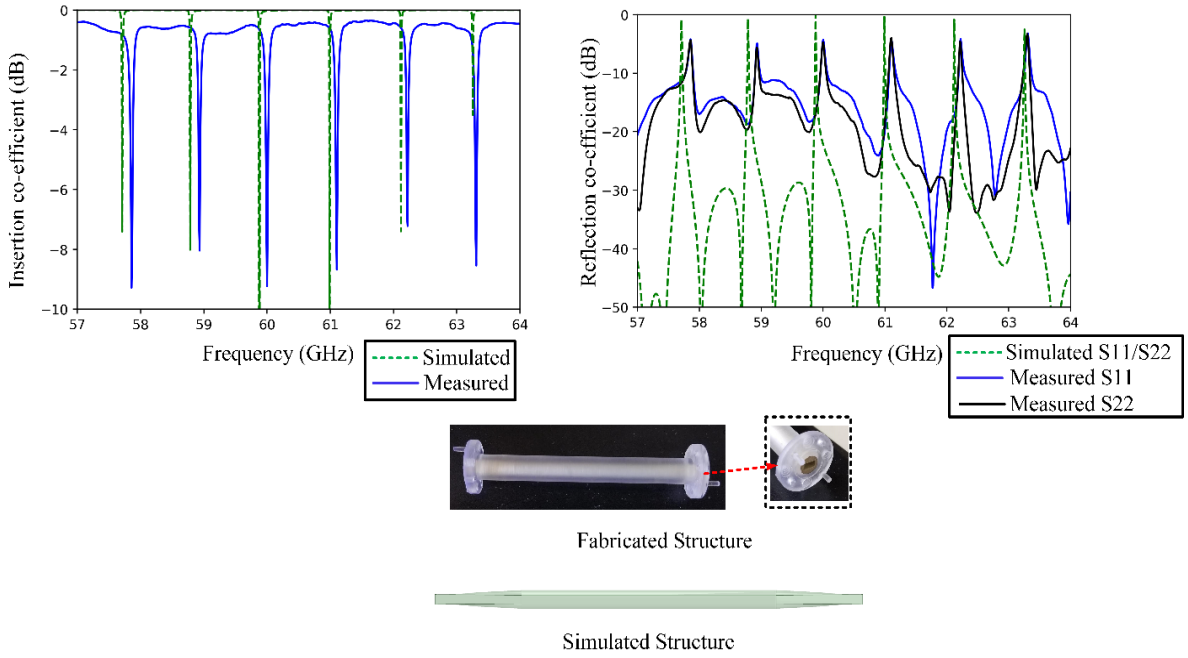

(a)

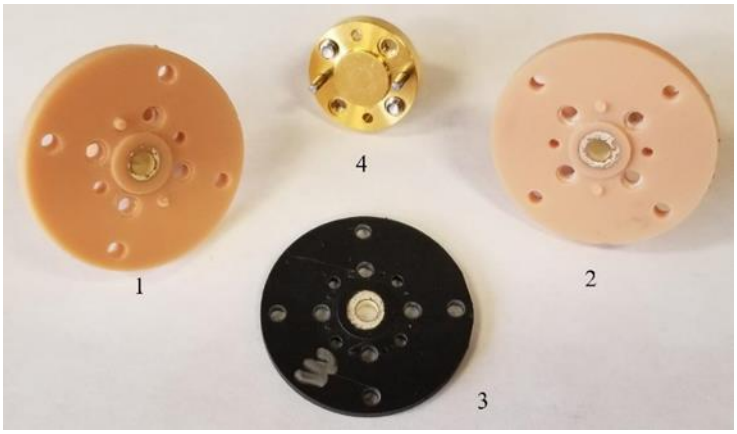

(b)

Figure 61 Measurement of single section circular waveguide connected to R2C-WG mode converter on either ends (a) Comparison of measured and simulated results (b) TRL calibration kit used for measuring the waveguide.

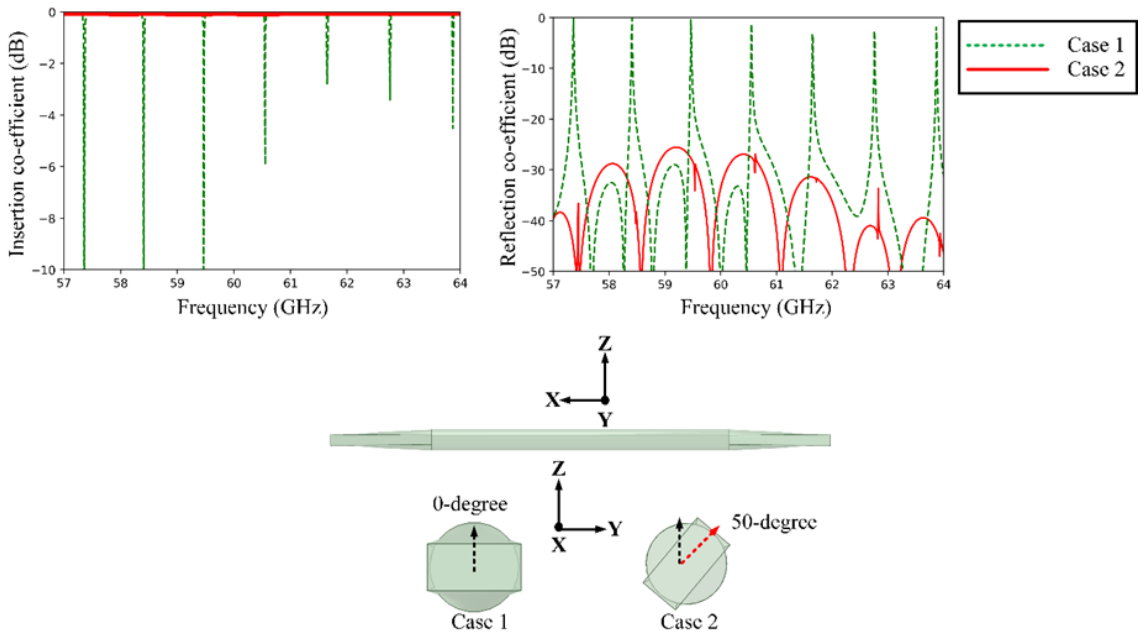

Figure 62 Measured single section circular waveguide with no tilt between the three sections and R2C-WG mode converters arbitrarily tilted from 0-degrees to remove the reflections seen in the structure.

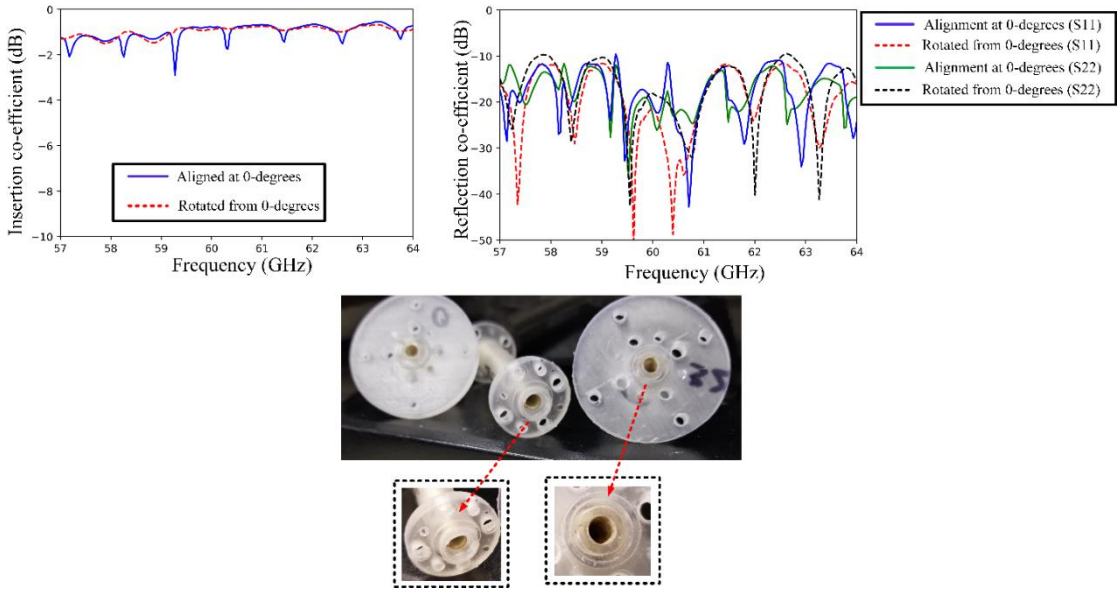

Figure 63 Measured results of contorted circular waveguide. (a) Waveguide printed at an arbitrary angle (b) waveguide printed horizontally to the base plate.

Figure 62 and Figure 63 investigates the effects of geometrical defects on the electromagnetic performance of the structure and projects the effects of geometrical defects on field alignment. In Figure 62 it is shown that the geometrical approximations in simulation leads to misalignment of electric field at the intersection of mode converter and CWG. The reflections reduce in intensity when the structure is tilted at an angle of 50 degrees with respect to the principal axis (z-axis). This observation has also been encountered in measured results shown in Figure 63. Though the tilt of principle axis is different between the measured and simulated scenario but the effect of geometrical approximations on the alignment of launched mode in CWG can be clearly seen. The tilt in measured scenario is obtained by modifying the cross-section of the flange which behaves like a lock and key system allowing free rotation between CWG and R2C-WG mode converter. The R2C-WG mode transition is rotated on either ends to obtain S21 and S11/S22 results with minimum or no reflection.

Figure 64 shows the fabricated contorted CWG connected to R2C-WG on either ends and its measurement set-up where the contorted waveguide is connected to commercial coax to rectangular waveguide connector. The contorted CWG consists of 10 different sections of CWG oriented vertically as well as horizontally. Each section is segmented separately based on printer resolution and orientation. The contorted waveguide is printed at horizontal and arbitrary (vertical and 45 degrees with x-axis) orientations as shown in Figure 65. Figure 66 shows the measured results of the contorted waveguide section 3D printed at these different angles. The horizontal orientation offers optimum results with

the magnitude of S21 around 0 dB and S11/S22 below -5 dB for the entire frequency range. While the arbitrary orientation reflects back almost the entire launched power from the waveguide. The S11/S22 values are closer to 0 dB and S21 below -5 dB. This indicates the sensitivity of electric field orientation at each cross-section which is dominated by the angle at which the structure is printed. The periodic reflections in the measurement are attributed to the excitation of undesired modes in circular waveguide due to geometrical defects introduced during the process of CAD modelling to 3D printing.

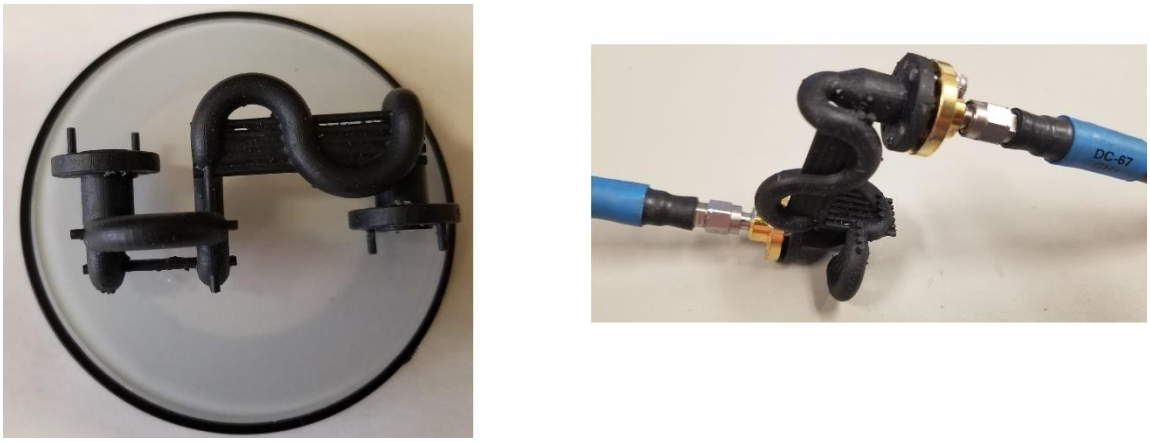

(a) (b)

Figure 64 Contorted circular waveguide (a) fabricated and metallized structure (b) measurement set-up with the contorted waveguide connected to commercial flange for measurement.

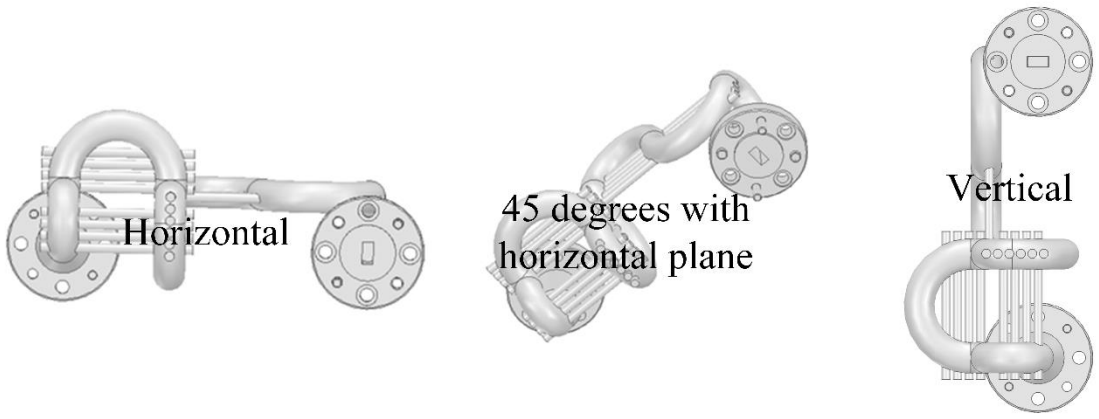

Figure 65 Different orientation of print for the contorted CWG: horizontal, angled and vertical with respect to base plane.

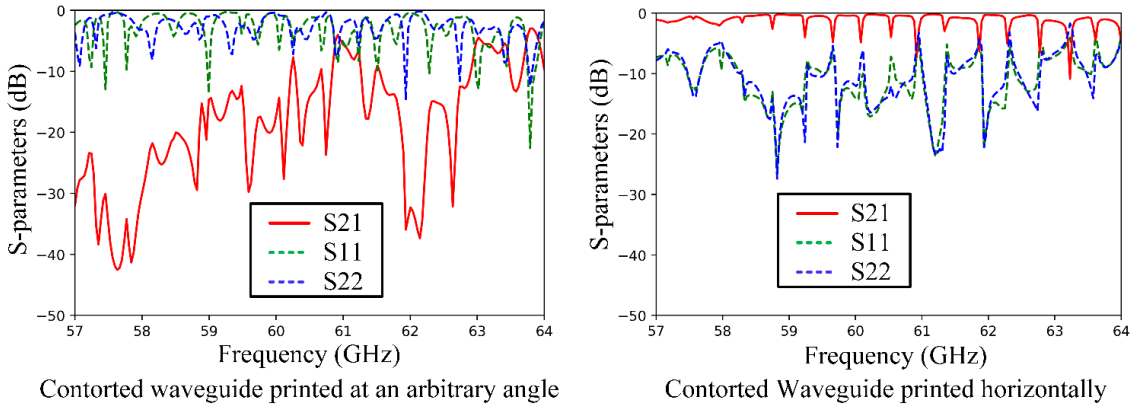

Figure 66 Measured results of contorted circular waveguide. (a) Waveguide printed at an arbitrary (vertical and 45 degrees with base plane) angle (b) waveguide printed horizontally to the base plate.

4X4 Contorted Butler Matrix

Figure 67 shows the fabricated model of 4X4 contorted Butler matrix in black resin with supports for mechanical stability of the structure. The whole structure is printed vertically for ease and accuracy of printing of hybrid couplers. Horizontal fabrication of Butler matrix would yield accurate print of phase bends but would lead to torn prints of inductive

curvilinear posts inside the hybrid coupler. The vertical print though increases geometrical defects and inaccuracies but leads to successful fabrication of the whole structure. Figure 68 shows the simulated magnitude and phase differences when each input port is excited. These results are obtained without connecting R2C-WG mode converter in the simulation. This 4X4 Butler matrix could be used for scanning beam in the XY-plane. The beam scanning ability of the Butler matrix is demonstrated by connecting the Butler matrix to waveguide antennas. The separation between the waveguides are maintained at 3.7 mm, more than the recommended spacing of 2.5 mm (half wavelength at 60 GHz) as the diameter of antenna 3.5 mm so, maintaining a spacing of half wavelength is impossible. The beam scanning of the waveguide antenna using Butler matrix is shown in Figure 69.

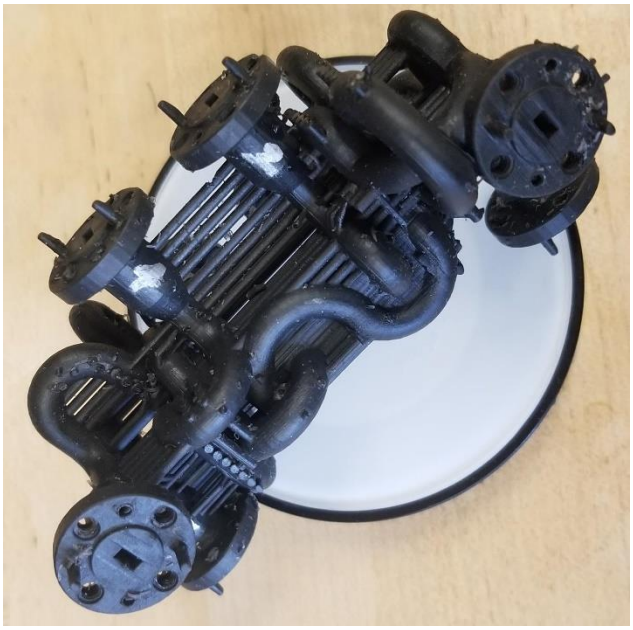

Figure 67 4X4 Butler matrix fabricated with black resin.

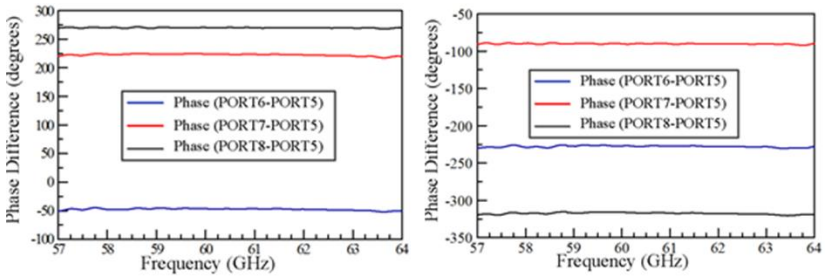

PORT 1 Excited PORT 2 Excited

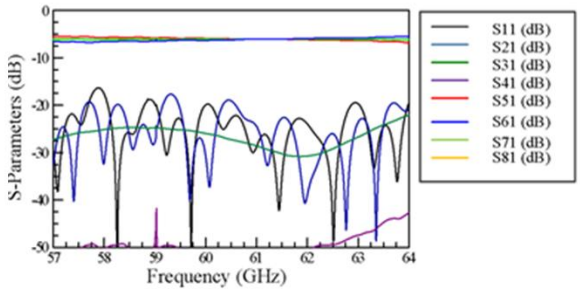

Magnitude Response

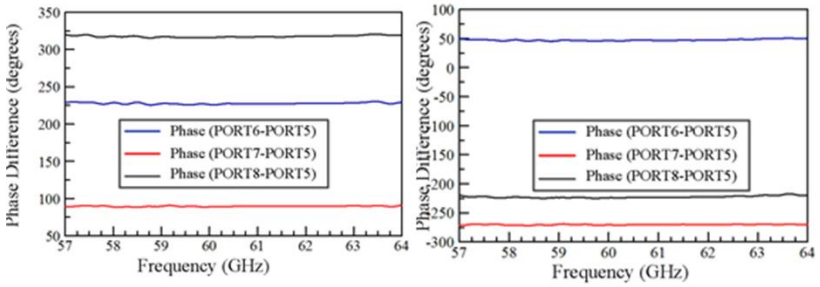

PORT 3 Excited PORT 4 Excited

Figure 68 Simulated results of 4X4 Butler matrix showing both phase difference and magnitude.

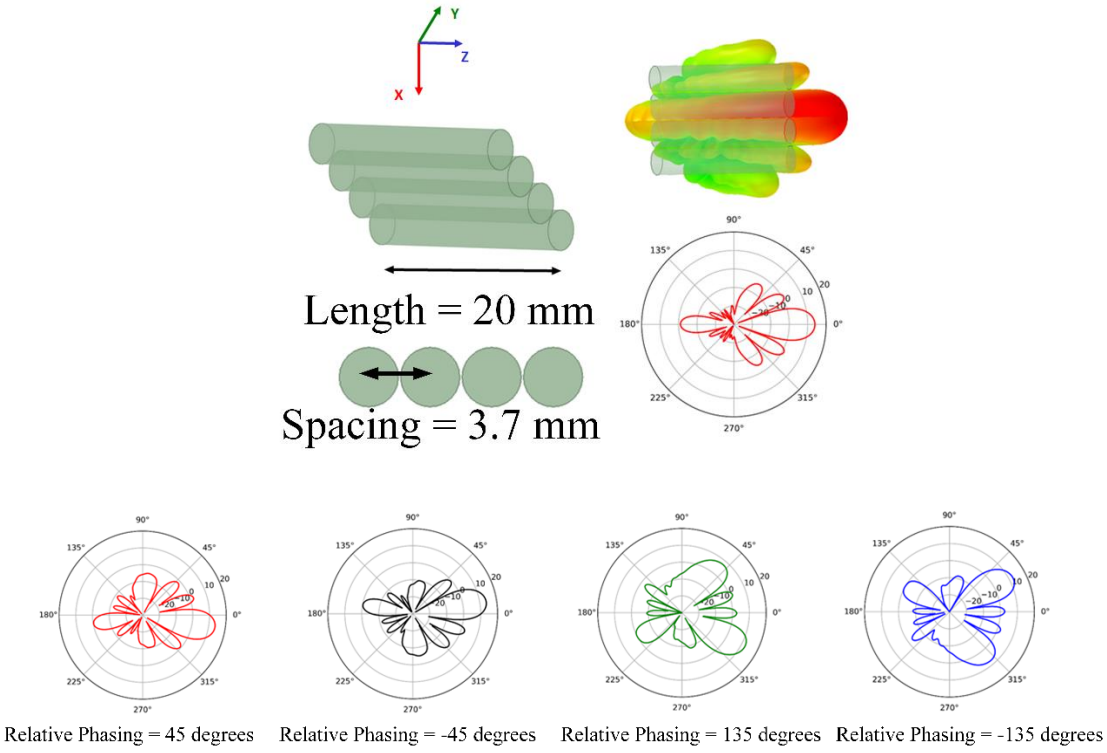

Figure 69 Beam scanning using 4X4 Butler matrix connected to waveguide antenna.

Discussion

Some of the geometrical defects introduced by additive manufacturing techniques could possibly affect the electromagnetic performance of a structure especially operating at higher frequencies when the dimension of the structure grazes closer to the resolution of the printer while other defects might not. It is important to identify the sources of defects introduced during printing that affect the performance of the structure and propose possible solutions keeping in mind the available resources. The fabrication defects introduced in this chapter could be alleviated by either using a printer with higher resolution or operating the entire system at the lower frequency for closer approximation of entire geometry. The aberrations in the measured results arise due to the introduction

of R2C-WG mode converters which introduces undesired modes in the system. These reflections could possibly be reduced or removed by application of different mode converters or launch techniques.

Key Contributions

- The contorted complex waveguide and Butler matrix structures introduced in this chapter shows that complex bends and curves could be designed to maintain rotational symmetry preserving the polarization of the structure.
- Identified the source of anomalous reflections observed in measurements by analyzing mode converters and other locations susceptible to fabrication workflow.
- Successfully established the relation between fabrication limitations on performance of complex waveguide structures with multiple twists and bends.
- Demonstrated the successful operation of contorted three-dimensional 4X4 Butler matrix over the frequency range of 57-64 GHz

CHAPTER V

CONCLUSION

This work provides systematic overview along with measured and simulated results of complex-geometry additively manufactured structures electromagnetically functionalized by selective pressure drive flow of fluids. These structures offer advances in the design space created by the amalgamation of distinct research areas that is electromagnetics, fluidics and additive manufacturing. Two different electromagnetic structures have been investigated for the study- structurally embedded vascular antenna array and contorted waveguide beamforming network. These structures are additively printed by depositing layer-upon-layer of material and electromagnetically functionalized by controlled flow of liquid metal or metal bath through the system.

The first work investigated in this dissertation consists of a structurally embedded antenna in multilayer and an antenna array shaped in the form of a leading edge of UAV, reconfigurable over a wide frequency range. These structures consist of geometrically distinct microvascular capillaries embedded in-between layers of epoxy and capable of transporting conductive fluid. The multilayer structure consists of two distinct geometrical patterns of microvascular cavities embedded in distict layers and operated as an antenna over a decade frequency range by controlled transport of liquid metal through these channels. The complex-curved antenna array assumes the shape of a predetermined mandrel with microvascular capillaries embedded in the curve. This antenna array is

capable of frequency reconfiguration and beam scanning. The structurally embedded vascular antennas offer advances in the current fabrication techniques through multilayer and complex-curved structures over planar and non-conformal EM devices which restrict the current design scope. The scope of amalgamation occurring from this field is clearly showcased through these structures and the limitations associated with the operation is also highlighted. Future work involves design of effective pump system for easy and measured flow of liquid metal in the capillaries both in forward and reverse direction without leaving behind traces of liquid metal in the microvascular channels. Improvement or advancement in the characteristics of conductive fluid are important steps in this direction to avoid traces of liquid metal left behind by retraction. Embedded feed in the epoxy substrate and precise measurement of liquid metal volume in embedded capillaries could also possibly reduce some of the deviations seen between measured and simulated results. These shape conformal structures open new avenues for designing antennas and microwave circuits on various other geometries with complex curves.

The second work investigated is the design, analysis, fabrication and metallization of contorted and complexly curved waveguides and beamforming networks. This work shows the design of geometrically complex waveguide structures with bends and twists preserving the polarization and rotational symmetry. Selective closed-loop circulatory electroless metallization technique has been developed to effectively deposit metal on inner surface of waveguides and antennas at low-cost generating low waste. This metallization technique could be extended to metallize any closed waveguiding or antenna

structures with silver or any other metal of interest, operating over any frequency band. Different other acrylate materials and even metal printed components could also be considered for metallization using similar techniques. The closed-loop pump system could be operated with pre-defined flow levels and pressure to regulate the area and degree of deposition. This would require careful and extensible studies of fluidics through complex curved systems. The sources of error highlighted in this work helps in developing understanding of the defects in fabrication flow process that affects the electromagnetic performance. This analysis could be used as a reference in the future to develop feedback system, advanced fabrication techniques or designs to alleviate these issues. The 4X4 Butler matrix developed in this work could also be potentially used to develop higher order beamforming networks as well as array system for beam scanning.

This work shows significant progress made in creating geometrically-complex antennas and contorted waveguide beam forming networks fabricated using additive techniques and electromagnetically functionalized by fluidic or microfluidic process. Through this work scope of current techniques are emphasized and their limitations are also highlighted. Future works involve working on some of the issues seen in this field and advancing the field with the available techniques highlighted.

REFERENCES

[1] A. Uriondo, M. Esperon-Miguez, and S. Perinpanayagam, “The present and future of additive manufacturing in the aerospace sector: A review of important aspects,” *Proc. Inst. Mech. Eng. Part G J. Aerosp. Eng.*, vol. 229, no. 11, pp. 2132–2147, 2015, doi: 10.1177/0954410014568797.

[2] R. Liu, Z. Wang, T. Sparks, F. Liou, J. Newkirk, and U. States, “13 13.1,” 2017.

[3] S. M. Yusuf, S. Cutler, and N. Gao, “Review: The impact of metal additive manufacturing on the aerospace industry,” *Metals (Basel).*, vol. 9, no. 12, 2019, doi: 10.3390/met9121286.

[4] O. Borgue, M. Panarotto, and O. Isaksson, “Impact on design when introducing additive manufacturing in space applications,” *Proc. Int. Des. Conf. Des.*, vol. 3, pp. 997–1008, 2018, doi: 10.21278/idc.2018.0412.

[5] A. Paolini, S. Kollmannsberger, and E. Rank, “Additive manufacturing in construction: A review on processes, applications, and digital planning methods,” *Addit. Manuf.*, vol. 30, no. July, 2019, doi: 10.1016/j.addma.2019.100894.

[6] D. Delgado Camacho *et al.*, “Applications of additive manufacturing in the construction industry – A forward-looking review,” *Autom. Constr.*, vol. 89, no. December 2017, pp. 110–119, 2018, doi: 10.1016/j.autcon.2017.12.031.

[7] C. Dordlofva, O. Borgue, M. Panarotto, and O. Isaksson, “Drivers and guidelines in design for qualification using additive manufacturing in space applications,” *Proc. Int. Conf. Eng. Des. ICED*, vol. 2019-Augus, no. August, pp. 729–738, 2019, doi: 10.1017/dsi.2019.77.

[8] K. V. Hoel, M. Ignatenko, S. Kristoffersen, E. Lier, and D. S. Filipovic, “3-D Printed Monolithic GRIN Dielectric-Loaded Double-Ridged Horn Antennas,” *IEEE Trans. Antennas Propag.*, vol. 68, no. 1, pp. 533–539, 2020, doi: 10.1109/TAP.2019.2938563.

[9] M. Li, Y. Yang, F. Iacopi, J. Nulman, and S. Chappel-Ram, “3D-Printed Low-Profile Single-Substrate Multi-Metal Layer Antennas and Array with Bandwidth Enhancement,” *IEEE Access*, vol. 8, pp. 217370–217379, 2020, doi:

10.1109/ACCESS.2020.3041232.

[10] K. Johnson *et al.*, “Digital Manufacturing of Pathologically-Complex 3D Printed Antennas,” *IEEE Access*, vol. 7, pp. 39378–39389, 2019, doi: 10.1109/ACCESS.2019.2906868.

[11] C. Gu *et al.*, “A D-Band 3D-Printed Antenna,” vol. 10, no. 5, pp. 433–442, 2020.

[12] S. Y. Jun, B. Sanz-Izquierdo, E. A. Parker, D. Bird, and A. McClelland, “Manufacturing Considerations in the 3-D Printing of Fractal Antennas,” *IEEE Trans. Components, Packag. Manuf. Technol.*, vol. 7, no. 11, pp. 1891–1898, 2017, doi: 10.1109/TCPMT.2017.2730366.

[13] Y. X. Zhang, Y. C. Jiao, and S. Bin Liu, “3-D-Printed comb mushroom-like dielectric lens for stable gain enhancement of printed log-periodic dipole array,” *IEEE Antennas Wirel. Propag. Lett.*, vol. 17, no. 11, pp. 2099–2103, 2018, doi: 10.1109/LAWP.2018.2851298.

[14] A. S. Kaddour, S. Bories, A. Bellion, and C. Delaveaud, “3-D-printed compact wideband magnetoelectric dipoles with circular polarization,” *IEEE Antennas Wirel. Propag. Lett.*, vol. 17, no. 11, pp. 2026–2030, 2018, doi: 10.1109/LAWP.2018.2849092.

[15] J. Shen and D. S. Ricketts, “Compact W-Band ‘Swan Neck’ turnstile junction orthomode transducer implemented by 3-D printing,” *IEEE Trans. Microw. Theory Tech.*, vol. 68, no. 8, pp. 3408–3417, 2020, doi: 10.1109/TMTT.2020.2992065.

[16] A. Vallecchi, D. Cadman, W. G. Whittow, J. Vardaxoglou, E. Shamonina, and C. J. Stevens, “3-D Printed Bandpass Filters with Coupled Vertically Extruded Split Ring Resonators,” *IEEE Trans. Microw. Theory Tech.*, vol. 67, no. 11, pp. 4341–4352, 2019, doi: 10.1109/TMTT.2019.2934456.

[17] K. Lomakin *et al.*, “3D Printed E-Band Hybrid Coupler,” *IEEE Microw. Wirel. Components Lett.*, vol. 29, no. 9, pp. 580–582, 2019, doi: 10.1109/LMWC.2019.2931458.

[18] G. L. Huang, C. Z. Han, W. Xu, T. Yuan, and X. Zhang, “A compact 16-way high-power combiner implemented via 3-d metal printing technique for advanced radio-

frequency electronics system applications," *IEEE Trans. Ind. Electron.*, vol. 66, no. 6, pp. 4767–4776, 2019, doi: 10.1109/TIE.2018.2863219.

[19] Q. Zhang and R. H. Austin, "Applications of Microfluidics in Stem Cell Biology," *Bionanoscience*, vol. 2, no. 4, pp. 277–286, 2012, doi: 10.1007/s12668-012-0051-8.

[20] S. Mashaghi, A. Abbaspourrad, D. A. Weitz, and A. M. van Oijen, "Droplet microfluidics: A tool for biology, chemistry and nanotechnology," *TrAC - Trends Anal. Chem.*, vol. 82, pp. 118–125, 2016, doi: 10.1016/j.trac.2016.05.019.

[21] Y. He, Y. Wu, J. Z. Fu, Q. Gao, and J. J. Qiu, "Developments of 3D Printing Microfluidics and Applications in Chemistry and Biology: a Review," *Electroanalysis*, vol. 28, no. 8, pp. 1658–1678, 2016, doi: 10.1002/elan.201600043.

[22] R. van Erp, R. Soleimanzadeh, L. Nela, G. Kampitsis, and E. Matioli, "Co-designing electronics with microfluidics for more sustainable cooling," *Nature*, vol. 585, no. 7824, pp. 211–216, 2020, doi: 10.1038/s41586-020-2666-1.

[23] S. Cheng and Z. Wu, "Microfluidic electronics," *Lab Chip*, vol. 12, no. 16, pp. 2782–2791, 2012, doi: 10.1039/c2lc21176a.

[24] P. Mostafalu, M. Akbari, K. A. Alberti, Q. Xu, A. Khademhosseini, and S. R. Sonkusale, "A toolkit of thread-based microfluidics, sensors, and electronics for 3D tissue embedding for medical diagnostics," *Microsystems Nanoeng.*, vol. 2, no. April, 2016, doi: 10.1038/micronano.2016.39.

[25] A. H. Naqvi, S. Member, and S. Lim, "Microfluidically Polarization-Switchable," vol. 17, no. 12, pp. 2255–2259, 2018.

[26] H. Tang and J. X. Chen, "Microfluidically Frequency-Reconfigurable Microstrip Patch Antenna and Array," *IEEE Access*, vol. 5, pp. 20470–20476, 2017, doi: 10.1109/ACCESS.2017.2756638.

[27] L. Song, W. Gao, C. O. Chui, and Y. Rahmat-Samii, "Liquid metal 3D printed microfluidic channel reconfigurable patch antenna with switchable slots," *2018 United States Natl. Comm. URSI Natl. Radio Sci. Meet. Usn. NRSM 2018*, vol. 2018-Janua, pp. 1–2, 2018.

[28] A. S. Griffin, H. Pan, J. D. Barrera, G. H. Huff, S. R. White, and N. R. Sottos, "A polarization reconfigurable microstrip patch antenna using liquid metal microfluidics," *Smart Mater. Struct.*, vol. 29, no. 4, 2020, doi: 10.1088/1361-665X/ab78b3.

[29] S. J. Kim, G. J. Lim, J. Cho, and M. J. Côté, "Drone-Aided Healthcare Services for Patients with Chronic Diseases in Rural Areas," *J. Intell. Robot. Syst. Theory Appl.*, vol. 88, no. 1, pp. 163–180, 2017, doi: 10.1007/s10846-017-0548-z.

[30] M. G. Fernandez, Y. A. Lopez, and F. L. H. Andres, "On the use of unmanned aerial vehicles for antenna and coverage diagnostics in mobile networks," *IEEE Commun. Mag.*, vol. 56, no. 7, pp. 72–78, 2018, doi: 10.1109/MCOM.2018.1700991.

[31] H. Inata, S. Say, T. Ando, J. Liu, and S. Shimamoto, "Unmanned aerial vehicle based missing people detection system employing phased array antenna," *IEEE Wirel. Commun. Netw. Conf. WCNC*, vol. 2016-Septe, no. ComExCon, pp. 7–12, 2016, doi: 10.1109/WCNC.2016.7564674.

[32] S. Yoon, J. Tak, J. Choi, and Y. M. Park, "Conformal monopolar antenna for UAV applications," *2017 IEEE Antennas Propag. Soc. Int. Symp. Proc.*, vol. 2017-Janua, pp. 517–518, 2017, doi: 10.1109/APUSNCURSINRSM.2017.8072301.

[33] M. Nosrati, A. Jafargholi, R. Pazoki, and N. Tavassolian, "Broadband slotted blade dipole antenna for airborne UAV applications," *IEEE Trans. Antennas Propag.*, vol. 66, no. 8, pp. 3857–3864, 2018, doi: 10.1109/TAP.2018.2835524.

[34] D. Wu, X. Chen, L. Yang, G. Fu, and X. Shi, "Compact and Low-Profile Omnidirectional Circularly Polarized Antenna with Four Coupling Arcs for UAV Applications," *IEEE Antennas Wirel. Propag. Lett.*, vol. 16, pp. 2919–2922, 2017, doi: 10.1109/LAWP.2017.2752358.

[35] J. Hu, G. Q. Luo, and Z. C. Hao, "A Wideband Quad-Polarization Reconfigurable Metasurface Antenna," *IEEE Access*, vol. 6, pp. 6130–6137, 2017, doi: 10.1109/ACCESS.2017.2766231.

[36] L. I. Balderas, A. Reyna, M. A. Panduro, C. Del Rio, and A. R. Gutierrez, "Low-Profile Conformal UWB Antenna for UAV Applications," *IEEE Access*, vol. 7, pp.

127486–127494, 2019, doi: 10.1109/ACCESS.2019.2939511.

[37] H. H. Tran, N. Nguyen-Trong, T. T. Le, and H. C. Park, “Wideband and Multipolarization Reconfigurable Crossed Bowtie Dipole Antenna,” *IEEE Trans. Antennas Propag.*, vol. 65, no. 12, pp. 6968–6975, 2017, doi: 10.1109/TAP.2017.2766439.

[38] A. Costa, R. Gonçalves, P. Pinho, and N. B. Carvalho, “Design of UAV and ground station antennas for communications link budget improvement,” *2017 IEEE Antennas Propag. Soc. Int. Symp. Proc.*, vol. 2017-Janua, pp. 2627–2628, 2017, doi: 10.1109/APUSNCURSINRSM.2017.8073356.

[39] C. U. Lee, G. Noh, B. K. Ahn, J. W. Yu, and H. L. Lee, “Tilted-beam switched array antenna for UAV mounted radar applications with 360° coverage,” *Electron.*, vol. 8, no. 11, pp. 1–11, 2019, doi: 10.3390/electronics8111240.

[40] D. G. Seo, C. H. Jeong, Y. S. Choi, J. S. Park, Y. Y. Jeong, and W. S. Lee, “Wide beam coverage dipole antenna array with parasitic elements for UAV communication,” *2019 IEEE Int. Symp. Antennas Propag. Usn. Radio Sci. Meet. APSURSI 2019 - Proc.*, pp. 1147–1148, 2019, doi: 10.1109/APUSNCURSINRSM.2019.8888747.

[41] Y. Zhou, Y. Bayram, F. Du, L. Dai, and J. L. Volakis, “Polymer-carbon nanotube sheets for conformal load bearing antennas,” *IEEE Trans. Antennas Propag.*, vol. 58, no. 7, pp. 2169–2175, 2010, doi: 10.1109/TAP.2010.2048852.

[42] A. Mehdipour, C. W. Trueman, A. R. Sebak, I. D. Rosca, and S. V. Hoa, “Reinforced continuous carbon-fiber composites using multi-wall carbon nanotubes for wideband antenna applications,” *IEEE Trans. Antennas Propag.*, vol. 58, no. 7, pp. 2451–2456, 2010, doi: 10.1109/TAP.2010.2048862.

[43] F. Xu, B. Wei, W. Li, J. Liu, W. Liu, and Y. Qiu, “Cylindrical conformal single-patch microstrip antennas based on three dimensional woven glass fiber/epoxy resin composites,” *Compos. Part B Eng.*, vol. 78, pp. 331–337, 2015, doi: 10.1016/j.compositesb.2015.03.091.

[44] Y. Liu, H. Du, L. Liu, and J. Leng, “Shape memory polymers and their composites

in aerospace applications: A review," *Smart Mater. Struct.*, vol. 23, no. 2, 2014, doi: 10.1088/0964-1726/23/2/023001.

[45] J. Kim, J. Y. Jang, G. H. Ryu, J. H. Choi, and M. S. Kim, "Structural design and development of multiband aero-vehicle smart skin antenna," *J. Intell. Mater. Syst. Struct.*, vol. 25, no. 5, pp. 631–639, 2014, doi: 10.1177/1045389X13493358.

[46] S. Biswas, "Fabrication of Conformal Load Bearing Antenna using 3D Printing," *2018 IEEE Antennas Propag. Soc. Int. Symp. Usn. Natl. Radio Sci. Meet. APSURSI 2018 - Proc.*, no. July 2018, pp. 235–236, 2018, doi: 10.1109/APUSNCURSINRSM.2018.8608257.

[47] N. Bishop, M. Ali, W. Baron, J. Miller, J. Tuss, and D. Zeppettella, "Aperture coupled MEMS reconfigurable pixel patch antenna for conformal load bearing antenna structures (CLAS)," *IEEE Antennas Propag. Soc. AP-S Int. Symp.*, pp. 1091–1092, 2014, doi: 10.1109/APS.2014.6904872.

[48] N. A. Bishop, J. Miller, D. Zeppettella, W. Baron, J. Tuss, and M. Ali, "A Broadband High-Gain Bi-Layer LPDA for UHF Conformal Load-Bearing Antenna Structures (CLASs) Applications," *IEEE Trans. Antennas Propag.*, vol. 63, no. 5, pp. 2359–2364, 2015, doi: 10.1109/TAP.2015.2409866.

[49] L. Yao *et al.*, "Fabrication and characterization of microstrip array antennas integrated in the three dimensional orthogonal woven composite," *Compos. Part B Eng.*, vol. 42, no. 4, pp. 885–890, 2011, doi: 10.1016/j.compositesb.2011.01.006.

[50] J. Zhong, A. Kiourti, T. Sebastian, Y. Bayram, and J. L. Volakis, "Conformal Load-Bearing Spiral Antenna on Conductive Textile Threads," *IEEE Antennas Wirel. Propag. Lett.*, vol. 16, pp. 230–233, 2017, doi: 10.1109/LAWP.2016.2570807.

[51] A. Kiourti and J. L. Volakis, "Stretchable and flexible E-fiber wire antennas embedded in polymer," *IEEE Antennas Wirel. Propag. Lett.*, vol. 13, pp. 1381–1384, 2014, doi: 10.1109/LAWP.2014.2339636.

[52] C. Z. Du, S. S. Zhong, L. Yao, and Y. P. Qiu, "Textile microstrip two-element array antenna on 3D orthogonal woven composite," *Conf. Proc. Int. Symp. Signals, Syst. Electron.*, vol. 2, pp. 662–663, 2010, doi: 10.1109/ISSSE.2010.5606954.

[53] K. Ghorbani, “Conformal load bearing antenna structure using Carbon Fibre Reinforced Polymer (CFRP),” *2014 Int. Work. Antenna Technol. Small Antennas, Nov. EM Struct. Mater. Appl. iWAT 2014*, no. 11, p. 118, 2014, doi: 10.1109/IWAT.2014.6958612.

[54] M. S. Kim, C. Y. Park, C. M. Cho, and S. M. Jun, “A multi-band smart skin antenna design for flight demonstration,” *8th Eur. Conf. Antennas Propagation, EuCAP 2014*, no. EuCAP, pp. 2855–2859, 2014, doi: 10.1109/EuCAP.2014.6902422.

[55] Z. Wang, L. Zhang, Y. Bayram, and J. L. Volakis, “Embroidered conductive fibers on polymer composite for conformal antennas,” *IEEE Trans. Antennas Propag.*, vol. 60, no. 9, pp. 4141–4147, 2012, doi: 10.1109/TAP.2012.2207055.

[56] A. M. Morishita, C. K. Y. Kitamura, A. T. Ohta, and W. A. Shiroma, “Two-octave tunable liquid-metal monopole antenna,” *Electron. Lett.*, vol. 50, no. 1, pp. 19–20, 2014, doi: 10.1049/el.2013.2971.

[57] G. H. Huff *et al.*, “Embedded Vascular Antenna,” vol. 65, no. 5, pp. 2282–2288, 2017.

[58] D. Morales, N. A. Stoute, Z. Yu, D. E. Aspnes, and M. D. Dickey, “Liquid gallium and the eutectic gallium indium (EGaIn) alloy: Dielectric functions from 1.24 to 3.1 eV by electrochemical reduction of surface oxides,” *Appl. Phys. Lett.*, vol. 109, no. 9, 2016, doi: 10.1063/1.4961910.

[59] D. J. Hartl, G. J. Frank, R. J. Malak, and J. W. Baur, “A liquid metal-based structurally embedded vascular antenna: II. Multiobjective and parameterized design exploration,” *Smart Mater. Struct.*, vol. 26, no. 2, 2017, doi: 10.1088/1361-665X/aa513d.

[60] D. J. Hartl *et al.*, “Analysis and characterization of structurally embedded vascular antennas using liquid metals,” *Sensors Smart Struct. Technol. Civil, Mech. Aerosp. Syst. 2016*, vol. 9803, no. April 2016, p. 980333, 2016, doi: 10.1117/12.2219258.

[61] D. J. Hartl, G. J. Frank, G. H. Huff, and J. W. Baur, “A liquid metal-based structurally embedded vascular antenna: I. Concept and multiphysical modeling,” *Smart Mater. Struct.*, vol. 26, no. 2, 2017, doi: 10.1088/1361-665X/aa5142.

[62] D. J. Hartl, G. J. Frank, and J. W. Baur, “Effects of microchannels on the mechanical performance of multifunctional composite laminates with unidirectional laminae,” *Compos. Struct.*, vol. 143, pp. 242–254, 2016, doi: 10.1016/j.compstruct.2016.01.106.

[63] “No Title,” *36. Ansys HFSS: High Frequency Structural Simulator*. https://www.ansys.com/products/electronics/ansys-hfss.

[64] “The Curve Parallel to a Parabola Is Not a Parabola : Parallel Curves Author (s): F . Max Stein Published by : Taylor & Francis , Ltd . on behalf of the Mathematical Association of America Stable URL : https://www.jstor.org/stable/3027202 The Curve Paral,” vol. 11, no. 4, pp. 239–246, 1980.

[65] “No Title,” *38. 3MTM FluorinertTM Electronic Liquid FC-70 – 3M Science Applied to Life.*, *September 2019*. https://multimedia.3m.com/mws/media/64891O/fluorinert-electronic-liquid-fc-70.pdf.

[66] A. Vosoogh and P. S. Kildal, “Simple Formula for Aperture Efficiency Reduction Due to Grating Lobes in Planar Phased Arrays,” *IEEE Trans. Antennas Propag.*, vol. 64, no. 6, pp. 2263–2269, 2016, doi: 10.1109/TAP.2016.2551259.

[67] Y. Liu, Q. Wang, Y. Jia, and P. Zhu, “A Frequency- and Polarization-Reconfigurable Slot Antenna Using Liquid Metal,” *IEEE Trans. Antennas Propag.*, vol. 68, no. 11, pp. 7630–7635, 2020, doi: 10.1109/tap.2020.2993110.

[68] A. Singh, I. Goode, and C. E. Saavedra, “A Multistate Frequency Reconfigurable Monopole Antenna Using Fluidic Channels,” *IEEE Antennas Wirel. Propag. Lett.*, vol. 18, no. 5, pp. 856–860, 2019, doi: 10.1109/LAWP.2019.2903781.

[69] V. T. Bharambe and J. J. Adams, “Planar 2-D Beam Steering Antenna Using Liquid Metal Parasitics,” *IEEE Trans. Antennas Propag.*, vol. 68, no. 11, pp. 7320–7327, 2020, doi: 10.1109/tap.2020.2998219.

[70] J. Shen and D. S. Ricketts, “Additive manufacturing of complex millimeter-wave waveguides structures using digital light processing,” *IEEE Trans. Microw. Theory Tech.*, vol. 67, no. 3, pp. 893–895, 2019, doi: 10.1109/TMTT.2018.2889452.

[71] R. Zhu, G. Lipworth, T. Zvolensky, D. R. Smith, and D. L. Marks, “Versatile Manufacturing of Split-Block Microwave Devices Using Rapid Prototyping and Electroplating,” *IEEE Antennas Wirel. Propag. Lett.*, vol. 16, pp. 157–160, 2017, doi: 10.1109/LAWP.2016.2563398.

[72] P. Hfurvvdv *et al.*, “(ydoxdwlrq ri ’ 3ulqwlqj 7hfkqrorj\ iru &ruuxjdwhg +ruq $qwhqqd 0dqxidfwxulqj,” pp. 251–255.

[73] J. Shen *et al.*, “Rapid prototyping of low loss 3D printed waveguides for millimeter-wave applications,” *IEEE MTT-S Int. Microw. Symp. Dig.*, pp. 41–44, 2017, doi: 10.1109/MWSYM.2017.8058593.

[74] E. G. Geterud, P. Bergmark, and J. Yang, “Lightweight waveguide and antenna components using plating on plastics,” *2013 7th Eur. Conf. Antennas Propagation, EuCAP 2013*, pp. 1812–1815, 2013.

[75] J. Shen, M. Aiken, C. Ladd, M. D. Dickey, and D. S. Ricketts, “A simple electroless plating solution for 3D printed microwave components,” *Asia-Pacific Microw. Conf. Proceedings, APMC*, vol. 0, pp. 18–21, 2017, doi: 10.1109/APMC.2016.7931434.

[76] B. Zheng, L. P. Wong, L. Y. L. Wu, and Z. Chen, “Identifying Key Factors towards Highly Reflective Silver Coatings,” *Adv. Mater. Sci. Eng.*, vol. 2017, 2017, doi: 10.1155/2017/7686983.

[77] J. Y. Kim, J. Yu, J. H. Lee, and T. Y. Lee, “The effects of electroplating parameters on the composition and morphology of Sn-Ag solder,” *J. Electron. Mater.*, vol. 33, no. 12, pp. 1459–1464, 2004, doi: 10.1007/s11664-004-0087-9.

[78] B. stucker Ian Gibson, David Rosen, *No Title*. 2015.

[79] J. J. Adams *et al.*, “Conformal printing of electrically small antennas on three-dimensional surfaces,” *Adv. Mater.*, vol. 23, no. 11, pp. 1335–1340, 2011, doi: 10.1002/adma.201003734.

[80] D. Filonov, S. Kolen, A. Shmidt, Y. Shacham-Diamand, A. Boag, and P. Ginzburg, “Volumetric 3D-Printed Antennas, Manufactured via Selective Polymer Metallization,” *Phys. Status Solidi - Rapid Res. Lett.*, vol. 13, no. 6, pp. 0–4, 2019,

doi: 10.1002/pssr.201800668.

[81] S. Choi, W. Su, M. M. Tentzeris, and S. Lim, “A novel fluid-reconfigurable advanced and delayed phase line using inkjet-printed microfluidic composite right/left-handed transmission line,” *IEEE Microw. Wirel. Components Lett.*, vol. 25, no. 2, pp. 142–144, 2015, doi: 10.1109/LMWC.2014.2382685.

[82] D. Sessions, A. Cook, K. Fuchi, A. Gillman, G. Huff, and P. Buskohl, “Origami-inspired frequency selective surface with fixed frequency response under folding,” *Sensors (Switzerland)*, vol. 19, no. 21, pp. 1–20, 2019, doi: 10.3390/s19214808.

[83] E. Brachmann *et al.*, “Electroless-deposited platinum antennas for wireless surface acousticwave sensors,” *Materials (Basel).*, vol. 12, no. 7, pp. 1–13, 2019, doi: 10.3390/ma12071002.

[84] I. O. Saracho-Pantoja, J. R. Montejo-Garai, J. A. Ruiz-Cruz, and J. M. Rebollar, “Additive Manufacturing of 3D Printed Microwave Passive Components,” *Emerg. Microw. Technol. Ind. Agric. Med. Food Process.*, 2018, doi: 10.5772/intechopen.74275.

[85] S. Kim, “Inkjet-printed electronics on paper for rf identification (RFID) and sensing,” *Electron.*, vol. 9, no. 10, pp. 1–22, 2020, doi: 10.3390/electronics9101636.

[86] Z. Ali *et al.*, “Authentication Using Metallic Inkjet-Printed Chipless RFID Tags,” *IEEE Trans. Antennas Propag.*, vol. 68, no. 5, pp. 4137–4142, 2020, doi: 10.1109/TAP.2019.2948740.

[87] B. S. Cook, S. Member, J. R. Cooper, S. Member, and M. M. Tentzeris, “An Inkjet-Printed Micro fl uidic RFID-Enabled Platform for Wireless Lab-on-Chip Applications,” vol. 61, no. 12, pp. 4714–4723, 2013.

[88] N. Jastram, M. A. Altarifi, L. Boskovic, and D. S. Filipovic, “On the Split-Block Realization of Millimeter-Wave Ridge Waveguide Components,” *IEEE Microw. Wirel. Components Lett.*, vol. 28, no. 4, pp. 296–298, 2018, doi: 10.1109/LMWC.2018.2808420.

[89] K. Zhao, J. A. Ramsey, and N. Ghalichechian, “Fully 3-D-Printed Frequency-

Scanning Slotted Waveguide Array with Wideband Power-Divider," *IEEE Antennas Wirel. Propag. Lett.*, vol. 18, no. 12, pp. 2756–2760, 2019, doi: 10.1109/LAWP.2019.2951324.

[90] R. Colella, F. P. Chietera, F. Montagna, A. Greco, and L. Catarinucci, "Customizing 3D-Printing for Electromagnetics to Design Enhanced RFID Antennas," *IEEE J. Radio Freq. Identif.*, vol. 4, no. 4, pp. 452–460, 2020, doi: 10.1109/jrfid.2020.3001043.

[91] E. L. Chuma, Y. Iano, L. L. B. Roger, M. Scroccaro, F. Frazatto, and L. T. Manera, "Performance analysis of X band horn antennas using additive manufacturing method coated with different techniques," *J. Microwaves, Optoelectron. Electromagn. Appl.*, vol. 18, no. 2, pp. 263–269, 2019, doi: 10.1590/2179-10742019v18i21337.

[92] K. Lomakin *et al.*, "SLA-Printed 3-D Waveguide Paths for E-Band Using Electroless Silver Plating," *IEEE Trans. Components, Packag. Manuf. Technol.*, vol. 9, no. 12, pp. 2476–2481, 2019, doi: 10.1109/TCPMT.2019.2927671.

[93] S. Verploegh and Z. Popović, "V- and W-band Two-Way Waveguide Splitters Fabricated by Metal Additive Manufacturing," *2018 IEEE MTT-S Lat. Am. Microw. Conf. LAMC 2018 - Proc.*, pp. 8–11, 2018, doi: 10.1109/LAMC.2018.8699010.

[94] M. Kacar, T. M. Weller, and G. Mumcu, "3D Printed Wideband Multilayered Dual-Polarized Stacked Patch Antenna With Integrated MMIC Switch," *IEEE Open J. Antennas Propag.*, vol. 2, no. January, pp. 38–48, 2020, doi: 10.1109/ojap.2020.3041959.

[95] G. Navangul, R. Paul, and S. Anand, "Error minimization in layered manufacturing parts by stereolithography file modification using a vertex translation algorithm," *J. Manuf. Sci. Eng. Trans. ASME*, vol. 135, no. 3, pp. 1–13, 2013, doi: 10.1115/1.4024035.

[96] P. Stief, J. Y. Dantan, A. Etienne, and A. Siadat, "A new methodology to analyze the functional and physical architecture of existing products for an assembly

oriented product family identification," *Procedia CIRP*, vol. 70, pp. 47–52, 2018, doi: 10.1016/j.procir.2018.02.026.

[97] P. Cirp, C. D. Conference, P. Stief, J. Dantan, A. Etienne, and A. Siadat, "ScienceDirect Geometric modeling Geometric deviation deviation modeling with with Statistical Statistical Shape Shape Analysis Analysis in in Design Design for for Additive Additive Manufacturing Manufacturing a , ∗ the functional to analyze physical arch," 2019.

[98] Q. Huang, H. Nouri, K. Xu, Y. Chen, S. Sosina, and T. Dasgupta, "Statistical predictive modeling and compensation of geometric deviations of three-dimensional printed products," *J. Manuf. Sci. Eng. Trans. ASME*, vol. 136, no. 6, pp. 1–10, 2014, doi: 10.1115/1.4028510.

[99] Q. Huang, "An Analytical Foundation for Optimal Compensation of Three-Dimensional Shape Deformation in Additive Manufacturing," *J. Manuf. Sci. Eng. Trans. ASME*, vol. 138, no. 6, pp. 1–8, 2016, doi: 10.1115/1.4032220.

[100] A. Wang, S. Song, Q. Huang, and F. Tsung, "In-Plane Shape-Deviation Modeling and Compensation for Fused Deposition Modeling Processes," *IEEE Trans. Autom. Sci. Eng.*, vol. 14, no. 2, pp. 968–976, 2017, doi: 10.1109/TASE.2016.2544941.

[101] Q. Huang, J. Zhang, A. Sabbaghi, and T. Dasgupta, "Optimal offline compensation of shape shrinkage for three-dimensional printing processes," *IIE Trans. (Institute Ind. Eng.*, vol. 47, no. 5, pp. 431–441, 2015, doi: 10.1080/0740817X.2014.955599.

[102] W. Cheng, J. Y. H. Fuh, A. Y. C. Nee, Y. S. Wong, H. T. Loh, and T. Miyazawa, "Optimization of Part- Building Orientation in Stereolithography," *Rapid Prototyp. J.*, vol. 1, no. 4, pp. 12–23, 1995.

[103] P. Delfs, M. T̈ows, and H. J. Schmid, "Optimized build orientation of additive manufactured parts for improved surface quality and build time," *Addit. Manuf.*, vol. 12, pp. 314–320, 2016, doi: 10.1016/j.addma.2016.06.003.